

University of Windsor

## Scholarship at UWindor

---

Electronic Theses and Dissertations

Theses, Dissertations, and Major Papers

---

2014

### CFD Simulation of Oil Jets with Application to Piston Cooling

GHASSAN (GUS) NASIF

*University of Windsor*

Follow this and additional works at: <https://scholar.uwindsor.ca/etd>

---

#### Recommended Citation

NASIF, GHASSAN (GUS), "CFD Simulation of Oil Jets with Application to Piston Cooling" (2014). *Electronic Theses and Dissertations*. 5214.

<https://scholar.uwindsor.ca/etd/5214>

This online database contains the full-text of PhD dissertations and Masters' theses of University of Windsor students from 1954 forward. These documents are made available for personal study and research purposes only, in accordance with the Canadian Copyright Act and the Creative Commons license—CC BY-NC-ND (Attribution, Non-Commercial, No Derivative Works). Under this license, works must always be attributed to the copyright holder (original author), cannot be used for any commercial purposes, and may not be altered. Any other use would require the permission of the copyright holder. Students may inquire about withdrawing their dissertation and/or thesis from this database. For additional inquiries, please contact the repository administrator via email ([scholarship@uwindsor.ca](mailto:scholarship@uwindsor.ca)) or by telephone at 519-253-3000ext. 3208.

# **CFD Simulation of Oil Jets with Application to Piston Cooling**

By

**Ghassan Nasif**

A Dissertation

Submitted to the Faculty of Graduate Studies

Through the Department of Mechanical, Automotive and Materials Engineering

in Partial Fulfillment of the Requirements for

the Degree of Doctor of Philosophy

at the University of Windsor

Windsor, Ontario, Canada

2014

Copyright© 2014 Ghassan Nasif

# CFD Simulation of Oil Jets with Application to Piston Cooling

By

**Ghassan Nasif**

APPROVED BY:

---

H. Ge, External Examiner  
Chrysler Group LLC, USA

---

F. Ghrib  
Department of Civil & Environmental Engineering

---

G. Rankin  
Department of Mechanical, Automotive and Materials Engineering

---

B. Zhou  
Department of Mechanical, Automotive and Materials Engineering

---

R. Barron, Co-Advisor  
Department of Mechanical, Automotive and Materials Engineering

---

R. Balachandar, Co-Advisor  
Department of Mechanical, Automotive and Materials Engineering

17 September 2014

## **DECLARATION OF CO-AUTHORSHIP/ PREVIOUS PUBLICATIONS**

### **I. Co-Authorship Declaration**

I hereby declare that this dissertation incorporates the outcome of research undertaken under the co-supervision of Dr. Ronald M. Barron and Dr. Ram Balachandar from University of Windsor. In all cases, I certify that I am the principal author and have had a major role in the preparation and writing of the manuscripts.

I am aware of the University of Windsor Senate Policy on Authorship and I certify that I have properly acknowledged the contributions of other researchers to my dissertation.

I certify that, with the above qualifications, this dissertation, and the research to which it refers, is the product of my own work.

## II. Declaration of Previous Publications

This dissertation includes three original journal papers and five conference papers. The nature and extent of the co-authors' contributions in these publications was to provide supervision and advice in completing the research and preparing the manuscripts.

List of my publications are:

Dissertation Chapter	Publication title/full citation	Publication status
Chapter 5	Nasif, G., Barron, R.M. and Balachandar, R., 2014, "Simulation of Jet Impingement Heat Transfer onto a Moving Disc", Int. Journal of Heat and Mass Transfer.	Accepted for publication
Chapter 4	*Nasif, G., Barron, R.M. and Balachandar, R., 2014, "Heat Transfer Due to an Impinging Jet in a Confined Space", ASME, J. Heat Transfer, 136(11), doi: 10.1115/1.4028242	Published
Chapter 4	Nasif, G., Barron, R.M. and Balachandar, R., 2014, "Jet Impingement Heat Transfer: Stationary Disc", International Journal of Surface Engineering and Materials Technology (IJSEMT), 4(1), pp. 34-38.	Published
Chapter 5	Nasif, G., Barron, R.M. and Balachandar, R., 2014, "Heat Transfer Characteristics of Jet Impingement onto a Heated Disc Bounded by a Cylindrical Wall", Proceedings of the 10th International Conference on Heat Transfer, Fluid Mechanics and Thermodynamics (HEFAT), pp. 441-447, Orlando, FL, USA.	Published (proceedings)
Chapter 4 & 5	Nasif, G., Barron, R.M. and Balachandar, R., 2014, "Thermal Characteristics of Jet Impingement onto a Stationary and Moving Circular Disc", 22nd Annual Conference of the CFD Society of Canada, CFD 2014, Toronto, ON, Canada.	Presented in conference

Chapter 4	*Nasif, G., Barron, R.M., Balachandar, R. and Iqbal, O., 2013, "Simulation of Jet Impingement Heat Transfer", Proceedings of ASME 2013 Internal Combustion Engine Division (ICED), Fall Technical Conference, Paper No. ICEF2013-19050, Dearborn, MI, USA.	Published (proceedings)
Chapter 5	Nasif, G., Barron, R.M. and Balachandar, R., 2013, "Jet Impingement Heat Transfer: Moving Disc", Proceedings of the 22nd National and 11th ISHMT-ASME Heat and Mass Transfer Conference, Paper No. HMTC1300891, Kharagpur, India.	Published (proceedings)
Chapter 4	Nasif, G., Barron, R.M., Balachandar, R. and Iqbal, O., 2013, "Simulation of Jet Impingement Heat Transfer Using VOF", 21st Annual Conference of the CFD Society of Canada, CFD 2013, Sherbrooke, QC, Canada.	Presented in conference

*\*I am grateful to the American Society of Mechanical Engineers (ASME) for granting the permission to use my publications towards my Ph.D. dissertation.*

I certify that I have obtained written permission from the copyright holders to include the above published materials in my dissertation. An image of these written permissions is included in the Appendix. I certify that the above material describes work completed during my registration as a graduate student at the University of Windsor.

I declare that to the best of my knowledge, my dissertation does not infringe upon anyone's copyright nor violate any proprietary rights and that any ideas, techniques, quotations, or any other material from the work of other people included in my dissertation, published or otherwise, are fully acknowledged in accordance with standard referencing practices.

I declare that this is a true copy of my dissertation, including any final revisions, as approved by my dissertation committee and the Graduate Studies office, and that this dissertation has not been submitted for a higher degree to any other University or Institution.

## ABSTRACT

This computational study is concerned with oil jet impingement heat transfer with the aim to investigate and improve the heat transfer efficiency process of piston cooling. Finite volume based computations using CD-adapco's STAR-CCM+ are performed in this study. One of the advantages of this commercial code is its ability to tackle problems involving multi-physics and complex geometries. Generic models with fixed and reciprocating moving discs are used in the first stage of this study to investigate the thermal characteristics of the jet impingement. Subsequently, the information that has been acquired from the first stage is used to successfully simulate a full-scale engine and estimate the temperature profile and heat dissipation from the pistons with and without a cooling oil jet.

The computational results show that the radial extent of the stagnation region beneath the jet is not uniform as stated in the literature, but is a function of the radial velocity gradient  $\partial u_r / \partial r$  in this region. Correlations describing the stagnation zone and local Nusselt numbers have been developed, applicable over a wide range of Reynolds numbers and Prandtl numbers. The effect of nozzle geometry is found to be insignificant on thermal characteristics for long jets. For jet impingement onto a moving boundary, an innovative methodology to accelerate the computational solution and reduce the cost in term of CPU time has been developed and implemented.

Finally, the piston cooling process due to oil jet impingement is evaluated for the Fiat-Chrysler full-scale 2.0 L Tigershark Inline 4-Cylinder gasoline engine. For this specific simulation, the cooling jet reduces the volume average temperature, the stagnation zone temperature, the maximum and minimum temperatures in the piston by 10%, 25%, 12% and 25%, respectively, in comparison with the no cooling jet case.



## **DEDICATION**

I dedicate my efforts to:

my family

## **ACKNOWLEDGEMENTS**

I would like to express my deep and sincere gratitude and appreciation to my advisors Dr. R. M. Barron and Dr R. Balachandar for their invaluable support, technical guidance, genuine interest, and generosity throughout the course of this study. Not only have they been for me a source of great inspiration as teachers and researchers, but also an object of admiration as a person as well.

I sincerely acknowledge the members of my doctoral committee, Dr. G. Rankin, Dr. B. Zhao, Dr. F. Ghrib and Dr. H. Ge, for their valuable time and for serving on my committee. I would like also to thank the Chrysler Canada/University of Windsor Automotive Research and Development Centre (ARDC) for graciously extending the use of their computing facilities. Special thanks go to Dr. M. O. Iqbal for his help during the early part of this work.

I gratefully acknowledge the entrance scholarship that I received from University of Windsor and the financial support from the Natural Sciences and Engineering Research Council of Canada and Chrysler Canada Inc. through the NSERC Industrial Postgraduate Scholarship program. Finally, I am grateful to all family members for their encouragement, support and patience during my graduate study.

# TABLE OF CONTENTS

DECLARATION OF CO-AUTHORSHIP/ PREVIOUS PUBLICATIONS .....	iii
ABSTRACT.....	vii
DEDICATION .....	viii
ACKNOWLEDGEMENTS.....	ix
LIST OF TABLES.....	xiii
LIST OF FIGURES .....	xiv
NOMENCLATURE .....	xvii
CHAPTER 1: INTRODUCTION.....	1
1.1 Overview.....	1
1.2 Research Objective .....	3
1.3 Scope of this Dissertation .....	5
CHAPTER 2: LITERATURE REVIEW .....	7
2.1 Introduction.....	7
2.2 Laminar and Turbulent Jets .....	8
2.3 Splattering of Turbulent Liquid Jets .....	13
2.4 Jet Impingement Flow Field .....	15
2.5 Radial Velocity Gradient at Stagnation Point .....	18
2.6 Liquid Jet Primary Breakup .....	20
2.6.1 Liquid Jet Breakup in Quiescent Medium .....	21
2.6.2 Liquid Jet Breakup in Crossflow Medium .....	23
2.7 Thermal Characteristics of Liquid Impinging Jets .....	26
2.7.1 Physical Mechanism of Convection .....	27
2.7.2 Stagnation Zone and Local Nusselt Number .....	29
2.7.3 Effect of Nozzle Configuration .....	35
2.8 Conclusions.....	37

CHAPTER 3: COMPUTATIONAL METHODOLOGY.....	39
3.1 Introduction.....	39
3.2 Governing Equation .....	40
3.2.1 Transient Term .....	41
3.2.2 Convective Term .....	41
3.2.2 Diffusion Term .....	43
3.3 Reconstruction Gradient .....	45
3.4 Reconstruction Gradient Limiting .....	46
3.5 Cell Gradients .....	47
3.6 Iterative Methodology .....	47
3.6.1 Basic Iterative Methods .....	49
3.6.2 Multigrid Methods .....	50
3.7 Segregated Models .....	51
3.7.1 Segregated Flow Model .....	51
3.7.2 Segregated Fluid Energy Model .....	57
3.7.3 Segregated Volume of Fraction Model .....	63
3.8 Turbulent Model .....	73
3.8.1 $k-\omega$ Turbulence Solver .....	79
3.9 Final Remarks .....	79
 CHAPTER 4: HEAT TRANSFER DUE TO AN IMPINGING JET IN A CONFINED SPACE: STATIONARY DISC .....	 82
4.1 Introduction.....	82
4.2 Conjugate Heat Transfer (CHT) .....	83
4.3 Model Setup and Boundary Conditions .....	84
4.4 Validation of Numerical Simulation .....	88
4.5 Results .....	92
4.5.1 Effect of Nozzle Configuration (Long Jet).....	92
4.5.2 Stagnation Zone Nusselt Number ( $Nu_o$ ) .....	95
4.5.3 Local Nusselt Number ( $Nu$ ) .....	103
4.5.4 Disc Temperature Profile.....	109
4.6 Conclusions.....	111

CHAPTER 5: HEAT TRANSFER DUE TO A CONFINED JET IMPINGING ON TO A MOVING DISC .....	113
5.1 Introduction.....	113
5.2 Model Setup and Boundary Conditions .....	114
5.3 Results and Discussion .....	118
5.3.1 Moving Boundary without Jet .....	119
5.3.2 Moving Boundary with Jet .....	122
5.3.2.1 Initial Estimate of the Temperature Profile .....	124
5.3.2.2 Nusselt Number Profile .....	128
5.3.2.3 Disc Temperature Profile .....	133
5.4 Conclusions.....	138
CHAPTER 6: SIMULATION OF PISTON COOLING USING OIL JETS.....	141
6.1 Introduction.....	141
6.2 Model Setup and Boundary Conditions .....	143
6.3 Results and Discussion .....	149
6.3.1 Domain Initialization .....	149
6.3.2 Nusselt Number Profiles .....	154
6.3.3 Piston Temperature Profile .....	157
6.4 Conclusions.....	162
CHAPTER 7: CONCLUSIONS AND RECOMMENDATIONS .....	164
7.1 Conclusions.....	164
7.2 Recommendations for Future Work .....	166
REFERENCES .....	168
APPENDIX.....	175
VITA AUCTORIS .....	181

## LIST OF TABLES

Table 4.1: Input parameters for jet impingement onto a stationary disc .....	86
Table 4.2: Summary of thermal characteristics for different nozzle geometries .....	94
Table 4.3: Stagnation zone characteristics, for $H = 60$ mm.....	101
Table 5.1: Input parameters for current numerical simulation.....	115
Table 5.2: Surface average Nusselt number (averaged over one cycle) at solid-fluid interface without jet cooling, (a) $\omega = 210$ rad/s, (b) $\omega = 630$ rad/s .....	120
Table 5.3: Surface average Nusselt number at solid-fluid interface, at two elevations from the nozzle exit; (a) $H/d = 20$ , (b) $H/d = 100$ .....	125
Table 5.4: Comparison of computed $Nu_o$ with the results from equations (4.2) and (2.40) .....	127
Table 5.5: Angle of occurrence of the maximum $Nu$ and corresponding velocity gradient $\partial u_r / \partial r$ near the wall for the first three regions defined in Figure 5.3 ( $\omega = 630$ rad/s) .....	132
Table 5.6: Surface average Nusselt number (phase-averaged over one cycle) at solid-fluid interface with the cooling jet: (a) $\omega = 210$ rad/s, (b) $\omega = 630$ rad/s.....	135
Table 5.7: Surface average of steady-state temperature for the regions defined in Figure 5.3 .....	136
Table 6.1: Heat dissipation through different parts of the piston with and without jet .....	161

## LIST OF FIGURES

Figure 1.1: Oil squirter assembly .....	3
Figure 2.1: Schematic illustration of free surface jet structure with increasing Weber number (or Reynolds number) .....	9
Figure 2.2: Surface profiles of a jet issuing from a smooth pipe (left), and a rough pipe (right), as a function of the Reynolds number .....	12
Figure 2.3: (a) Splattering turbulent jet issuing from fully-developed nozzle showing radially travelling wave, $Re_d = 28,000$ , $\xi = 0.11$ , (b) Splattering turbulent jet issuing from fully-developed nozzle, $Re_d = 48,300$ , $\xi = 0.31$ , (c) Laminar impinging jet issuing from contoured orifice, $Re_d = 51,000$ , $d = 5.0$ mm .....	15
Figure 2.4: Jet and film flow showing hydrodynamic evolution .....	18
Figure 3.1: (a) Convective boundedness criterion (CBC) on the three control volumes; upwind (U), central (C) and downwind (D), (b) Normalized variable diagram (NVD); upwind differencing (UD), downwind differencing (DD), central differencing (CD) and linear upwind differencing (LUD) .....	67
Figure 3.2: NVD shows the universal limiter boundaries. The dashed red boundary has a Courant number dependent slope $1/C$ . The case shown is for $C \approx 0.2$ .....	70
Figure 4.1: Computational domain and relevant boundary conditions .....	84
Figure 4.2: Effect of domain confinement on local Nusselt number obtained for nozzle size $d = 4.0$ mm at $H/d = 15$ and $Re_d = 12000$ .....	89
Figure 4.3: Comparison of computed stagnation zone Nusselt number with correlation given by equation (2.39), for $H = 60$ mm .....	90
Figure 4.4: Comparison of computed local Nusselt number with correlation given by equation (2.40); $H = 60$ mm, $d = 2$ mm .....	91
Figure 4.5: Exit velocity profiles for three nozzles sizes .....	93
Figure 4.6: Suppression of the velocity gradient in radial direction (velocity relaxation) .....	93
Figure 4.7: Contours of radial velocity gradient $\partial u_r / \partial r$ and radial extent of the stagnation zone for $d = 1.0$ mm at $H/d = 60$ ; (a) $Re_d = 2000$ , (b) $Re_d = 4000$ , (c) $Re_d = 6000$ and (d) $Re_d = 8000$ .....	98
Figure 4.8: Contours of radial velocity gradient $\partial u_r / \partial r$ and radial extent of the stagnation zone for $d = 2.0$ mm at $H/d = 30$ ; (a) $Re_d = 4000$ , (b) $Re_d = 8000$ , (c) $Re_d = 12000$ and (d) $Re_d = 16000$ .....	99

Figure 4.9: Contours of radial velocity gradient $\partial u_r/\partial r$ and radial extent of the stagnation zone for $d = 4.0$ mm at $H/d = 15$ ; (a) $Re_d = 4000$ , (b) $Re_d = 8000$ , (c) $Re_d = 12000$ and (d) $Re_d = 16000$ .....	100
Figure 4.10: Dependence of: (a) stagnation point radial velocity gradient and (b) dimensionless radial velocity gradient, on the parameter $v_f/d$ .....	102
Figure 4.11: Variation of stagnation zone Nusselt number with Reynolds number ....	102
Figure 4.12: Local Nusselt number $Nu$ normalized by $Nu_o$ , $H = 60$ mm: (a) $H/d = 60$ , (b) $H/d = 30$ , (c) $H/d = 15$ .....	106
Figure 4.13: Temperature distribution across the fluid film at three different locations downstream of the stagnation point, $H = 60$ mm, $Re_d = 12000$ : (a) $H/d = 30$ , (b) $H/d = 15$ .....	107
Figure 4.14: Temperature distribution at the interface between the oil sheet and impinging surface, $H = 60$ mm, $Re_d = 12000$ : (a) $H/d = 30$ , (b) $H/d = 15$ .....	108
Figure 4.15: Distribution of radial velocity beneath the stagnation region (A): (a) $d = 1.0$ mm, $Re_d = 8000$ , (b) $d = 2.0$ mm, $Re_d = 16000$ , (c) $d = 4.0$ mm, $Re_d = 16000$ ....	108
Figure 5.1: Computational domain and relevant thermal boundary conditions .....	114
Figure 5.2: Motion profile over one cycle for two angular velocities of the disc; (a) 210 rad/s, (b) 630 rad/s .....	116
Figure 5.3: Delineation of the nine regions at the fluid-solid interface .....	118
Figure 5.4: Temperature profile in the disc without cooling jet; (a) $\omega = 210$ rad/s, (b) $\omega = 630$ rad/s .....	120
Figure 5.5: Contours of mean radial velocity averaged over one cycle; (a) $\omega = 210$ rad/s, (b) $\omega = 630$ rad/s .....	121
Figure 5.6: Evolution of liquid jet as disc moves towards its top position (TP), $\omega = 630$ rad/s .....	123
Figure 5.7: Steady-state temperature profile for stationary disc with cooling jet, at two elevations from the nozzle exit: (a) $H/d = 20$ , (b) $H/d = 100$ .....	124
Figure 5.8: (a) Horizontal section through liquid jet, at 2.0 mm before impinging point (velocity magnitude), (b) Solid-fluid interface (VOF) .....	126
Figure 5.9: Surface (solid-fluid interface) average transient Nusselt number with cooling jet; (a) $\omega = 210$ rad/s, (b) $\omega = 630$ rad/s .....	129
Figure 5.10: Nusselt number profile (one cycle) obtained from average of recurring cycles in Figure 5.9; (a) $\omega = 210$ rad/s, (b) $\omega = 630$ rad/s .....	130



Figure 5.11: Contours of radial velocity and volume fraction of oil adjacent to the solid-fluid interface for two inner regions defined in Figure 5.3 ( $\omega = 630$ rad/s) .....	131
Figure 5.12: Evolution of surface average temperatures at fluid-solid interface with physical time; (a) $\omega = 210$ rad/s, (b) $\omega = 630$ rad/s .....	133
Figure 5.13: Final temperature distribution in the moving disc with the cooling jet; (a) $\omega = 210$ rad/s, (b) $\omega = 630$ rad/s .....	134
Figure 5.14: Evolution of temperature profile at stagnation zone region (Region-1) for angular velocities 210 rad/s and 630 rad/s .....	138
Figure 6.1: Computational domain and relevant boundary conditions .....	144
Figure 6.2: Interfaces (yellow) between different parts inside the computational domain .....	145
Figure 6.3: (a) Meshed domain; (b) Cross-sectional view through meshed domain ...	145
Figure 6.4: (a) VOF contours for the entire computational domain after initialization; (b) Cross-sectional VOF contours passing through squirter and cooling jets .....	147
Figure 6.5: (a) Velocity profile at nozzle exit; (b) Motion profile over one cycle for engine speed $N = 2000$ rpm .....	148
Figure 6.6: Computational domain without oil sump, used for domain initialization .....	150
Figure 6.7: Steady-state contours from transient simulation for the computational domain shown in Figure 6.6; (a) Velocity magnitude; (b) Pressure; (c) Temperature; (d) Turbulent kinetic energy .....	151
Figure 6.8: Computational domain used to find the temperature profile in the solid piston with and without cooling jet .....	152
Figure 6.9: Temperature and pressure profile as function of crank angle, extracted at cylinder/ crankcase interface (interface 3 shown in Figure 6.2) .....	153
Figure 6.10: Solid piston configuration; (a) Entire piston; (b) External shell; (c) Internal shell .....	154
Figure 6.11: Average Nusselt number at piston-fluid interface; (a) without cooling jet; (b) with cooling jet .....	156
Figure 6.12: Computational domain (piston and two compression rings) with the relevant thermal boundary conditions .....	157
Figure 6.13: Temperature profile in the piston without cooling jet, $N = 2000$ rpm .....	159
Figure 6.14: Temperature profile in the piston with cooling jet, $N = 2000$ rpm (jet flow rate $\dot{Q} = 0.025$ m <sup>3</sup> /s, $v_{bulk} = 10$ m/s) .....	160

## Nomenclature

$A$	Control volume face area
$A_w$	Control volume face area at fluid-wall interface
$a$	Coefficient arising from finite volume discretization
$\overline{a_0}, \overline{a_1}$	Average of momentum coefficients
$B$	Dimensionless velocity gradient defined by equation (2.11)
$B_b$	Coefficient in blended wall law defined by equation (3.89)
$b$	Explicit contribution to discretized equation
$C$	Courant number
$C_b$	Coefficient in blended wall law defined by equation (3.88)
$CD_{k\omega}$	Coefficient related to cross-diffusion term in $k-\omega$ SST model
$C_{2-3}$	Constant, defined by equation (2.34)
$C_g$	Constant, depends on geometry in equation (2.29)
$c_f$	Skin friction coefficient
$c_p$	Specific heat
$D_b$	Coefficient in blended wall law defined by equation (3.87)
$D_{droplet}$	Droplet diameter from capillary breakup
$D_\omega$	Cross-derivative term defined by equation (3.130), $k-\omega$ SST model
$d$	Jet diameter at the exit of smooth pipe nozzle
$E$	Total energy
$E_w, E'$	Wall function coefficients defined by equation (3.79)
$F_1, F_2$	Functions defined by equations (3.131) & (3.135), $k-\omega$ SST model

$f_c$	Curvature correction factor in $k-\omega$ SST model
$f_r$	Roughness function
$f_\beta, f_{\beta^*}$	Functions defined by equations (3.136) & (3.139), $k-\omega$ SST model
$G_k$	Turbulent production
$G(Pr)$	Boundary layer function of Prandtl number
$G_\omega$	Production of specific dissipation rate
$g_b$	Blending function defined by equation (3.146)
$H$	Nozzle-to-target spacing
$H_e$	Total enthalpy defined by equation (3.64)
$h$	Heat transfer coefficient, $q''_w/(T_{ref} - T_w)$
$h_{local}$	Local heat transfer coefficient defined by equation (3.93)
$i$	Internal energy
$k$	Thermal conductivity or Turbulent kinetic energy
$k_{eff.}$	Effective thermal conductivity defined by equation (3.68)
$L_c$	Liquid jet breakup length
$l$	Characteristic length, equal to $d$ in this study
$m, n$	Exponents in equation (2.29), range between 0 and 1
$\dot{m}_f$	Control volume face mass flow rate
$Nu$	Local Nusselt number, $(hl/k)$
$Nu_d$	Local Nusselt number, $(hd/k)$
$Nu_o$	Stagnation zone Nusselt number, $(hd/k)$
$Oh$	Ohnesorge number defined by equation (2.19)

$P$	Function of Prandtl number defined by equation (3.81)
$Pr$	Prandtl number
$Pr_t$	Turbulent Prandtl number
$p$	Pressure
$Q$	Volume flow rate of splattered liquid
$Q_f$	Function used in calculation of $Y_{RC}$ , defined by equation (3.52)
$Q_s$	Volume flow rate of liquid jet
$q$	Momentum flux ratio defined by equation (2.20)
$q^+$	Dimensionless viscous dissipation
$q''_w$	Wall heat flux
$Re_d$	Reynolds number based on nozzle diameter
$r, z$	Cylindrical coordinates
$r_f$	Coefficient defined by equation (3.28)
$r_1$	Stagnation zone (or region) radius
$S_u$	Additional source specified by the user
$St$	Stanton number defined by equation (2.36)
$S_\phi$	Source term in equation (3.1)
$T$	Temperature
$T^+$	Dimensionless temperature
$T_f$	Temperature of incoming fluid
$T_{p0}$	Wall-cell centroid temperature defined by equation (3.94)
$T_{ref}$	Reference temperature
$T_s$	Liquid sheet free surface temperature

$T_w$	Local wall temperature
$t$	Time
$t'$	Turbulent time scale defined by equation (3.134)
$t_s(r)$	Sheet thickness of wall jet
$U, V, W$	Mean components of velocity vector
$u, v, w$	Instantaneous components of velocity vector
$u', v', w'$	Fluctuating components of velocity vector
$u^+$	Normalized wall-parallel velocity defined by equation (3.73)
$u_c^+$	Fictitious non-dimensional velocity defined by equation (3.83)
$u_{parallel}$	Wall-parallel component of velocity
$u_r, v_z$	Velocity components in radial and axial direction in cylindrical coordinate
$u'_r, v'_z$	Fluctuating components of velocity vector in cylindrical coordinate
$u_s$	Free surface velocity of liquid sheet
$u_\tau$	Shear velocity defined by equation (3.47)
$V$	Cell volume
$v_f$	Bulk velocity of incoming jet
$v_{max}$	Centreline velocity of incoming jet
$We_d$ (or) $We_{liq}$	Liquid jet Weber number defined by equation (2.18)
$We_{cf}$	Gas crossflow Weber number defined by equation (2.17)
$x, y, z$	Cartesian coordinates
$x_b$	Axial distance of breakup onset defined by equation (2.23)
$y_b$	Height of breakup onset defined by equation (2.22)

$y_{p0}$	Normal distance from the wall to the wall-cell centroid
$y^+$	Non-dimensional wall coordinate

## **Tensors & Vectors**

<b>A</b>	Control volume face area vector
<b>a</b>	Solution vector in equation (3.35)
<b>b</b>	Residual vector
$\mathbf{f}_r$	Body force due to rotation
$\mathbf{f}_g$	Body force due to gravity
$\mathbf{f}_p$	Porous media body force
$\mathbf{f}_\omega$	Vorticity confinement force
$\mathbf{f}_a$	User-defined body force
<b>I</b>	Identity matrix
<b>n</b>	Normal vector to surface element $dA$
$\mathbf{q}''$	Heat flux vector
<b>S</b>	Strain rate tensor defined by equation (3.128)
$\mathbf{T}_l$	Laminar stress tensor
$\mathbf{T}_t$	Turbulent stress tensor, defined by equation (3.42)
<b>U</b>	Mean velocity vector
<b>u</b>	Instantaneous velocity vector
<b>W</b>	Rotation rate tensor defined by equation (3.138)
$\mathbf{x}$	Position vector
$\alpha$	Face metric quantity defined by equation (3.14)

## Greek Symbols

$\alpha, \alpha^*$	Coefficients in $k-\omega$ SST model
$\alpha_i$	Volume fraction of the $i^{th}$ phase in the control volume V
$\alpha_{lim.}$	Scale factor defined by equation (3.22)
$\beta, \beta^*$	Coefficients in $k-\omega$ SST model
$\beta_f$	Blending function defined by equation (3.120)
$\beta_g$	Geometric weighting factor in equation (3.10)
$\Gamma$	Blending function in Kader's wall law defined by equation (3.91)
$\Gamma_\phi$	Diffusion coefficient in governing equation (3.1)
$\gamma_{RC}$	Rhie & Chow dissipation defined by equation (3.52)
$\gamma_{ts}$	Coefficient used in $\tau_t$ calculation at near wall locations
$\Delta t$	Time step size
$\delta, \delta_t$	Momentum and thermal boundary layer thickness
$\delta_{stag.}$	Stagnation zone boundary layer thickness
$\kappa$	Von Karman constant
$\mu$	Dynamic viscosity
$\mu_t$	Turbulent viscosity
$\mu_{eff.}$	Effective viscosity, $\mu + \mu_t$
$\nu$	Kinematic viscosity
$\zeta$	VOF normalized value
$\zeta_s$	Fraction of impinging liquid splattered, $Q_s/Q$
$\rho$	Density

$\sigma$	Liquid-gas surface tension
$\sigma_k, \sigma_\omega$	Inverse turbulent Schmidt number, coefficients used in $k$ - $\omega$ SST model
$\tau_w$	Wall shear stress
$\phi$	Transported scalar property
$\omega$	Specific dissipation rate or Angular velocity
$\omega_{spl.}$	Splattering parameter defined by equation (2.1)
$\omega_{u.relax}$	Under-relaxation factor in equation (3.33)



# CHAPTER 1

## INTRODUCTION

### 1.1 Overview

Pistons in today's motor vehicle engines perform a wide range of functions, e.g., they transmit the force generated by combustion gases to the connecting rod, they support the normal force applied against the cylinder walls while the cylinder pressure is conveyed to the connecting rod and together with their sealing elements, they seal the combustion chamber from the crankcase. The combustion chamber is the hottest part of the engine. The piston is the bottom of the combustion chamber and it is the only part of the chamber that is not cooled by the standard cooling system. Most of the heat is dissipated from the piston through the piston rings into the cylinder walls, or through the wrist pins and down the connecting rods. In the automotive industry, there is demand for increasing engine performance in conjunction with decreasing free space in the engine compartment. One of the consequences of increasing the engine power density is that it threatens the structural integrity of the pistons at high engine loads, making them susceptible to disintegration due to the thermal stress.

Internal combustion engine pistons can be cooled by oil, water or air. Air-cooling is simpler from a design point of view, but lower specific heat per unit volume of air requires very large quantities of air to be directed towards the piston. This involves bulky ducting arrangements and an additional air compressor, which makes it less appealing from a practical viewpoint. Water-cooling was applied to heavy, low speed engines for some time, but later it was abandoned because of serious design and maintenance

difficulties with piping and sealing. Oil jet piston cooling is an alternative way to cool the piston. The oil jet splashes the oil on to the underside surface of the piston, thus removing the heat from the piston and effectively cooling it.

Impinging jets provide an effective manner to transfer energy or mass in many industrial applications. A directed liquid or gaseous flow released against a surface can efficiently transfer large amounts of thermal energy or mass between the surface and the fluid. Jet impingement is characterized by very low thermal resistance and is relatively simple to implement (Agarwal et al., 2011). In many applications, the conventional cooling requirements are limited by other restrictive factors such as available space, coolant selection, local environmental conditions and maximum allowable surface temperature.

Over the past few years, the oil jet cooling technology has been adopted by many automotive manufacturers to prevent overheating of the piston and to meet low emission and high power density requirements. Knock reduction is also one of the positive consequences of using oil squirters. A jet of pressurized engine oil is sprayed to the underside of each piston to help dissipate the extreme heat generated during sustained high rpm operation. An oil squirter or nozzle is mounted at an appropriate location in the block to clear the piston skirt as shown in Figure 1.1. Each squirter is equipped with a check valve to keep oil from draining back into the sump. The check valve has a spring that is only activated at a certain engine rpm, i.e., at high oil pressure.



Figure 1.1: Oil squirter assembly ([www.turbo-mopar.com](http://www.turbo-mopar.com))

## 1.2 Research Objective

Chrysler Canada/University of Windsor Automotive Research and Development Centre (ARDC) is presently interested in improving the performance of oil squirters that are currently used in engines manufactured by Fiat-Chrysler Automobiles. Given the enormous importance of oil squirters and the potential for future opportunities, new challenges have been identified that require a better understanding of the fundamental principles of the application. The setup complexity and high cost of conducting experiments for this particular problem provides strong motivation to pursue the

relatively less expensive Computational Fluid Dynamics (CFD) simulation methodology for investigation of the jet cooling technology.

This dissertation aims to obtain an effective approach to evaluate the cooling process of the piston by oil jet impingement without phase change. The oil jet is directed at a small region on the underside of the piston where the maximum temperature is expected.

The objectives of this research are to:

- Investigate the local convective heat transfer at the underside and exterior piston walls with and without an impinging oil jet. The heat transfer coefficient will assist to predict the temperature distribution in the piston and subsequently the heat transfer efficiency of the cooling process.
- Evaluate the effect of nozzle size, jet Reynolds number and moving boundary on the cooling process.
- Predict the maximum temperature that may occur in the piston to ensure that the temperature does not exceed the recommended limits.
- Estimate the heat dissipation throughout the different parts of the piston, i.e., piston rings, piston pin and inner shell of the piston with and without cooling jet.
- Provide a well-grounded computational methodology to simulate similar problems as part of Fiat-Chrysler Automobiles ongoing engine research program. This study gives a benchmark and path for similar future work.

### **1.3 The Scope of this Dissertation**

The flow field in the current study involves significant complexity in terms of multi-physics, tight geometry, moving parts, etc. Many thermal and fluid variables interact in this complicated process. Various meshing and mesh moving techniques are required, including arbitrary sliding interface (ASI) of counter weights and mesh morphing to replicate the linear motion of the target, i.e., disc or piston. Time dependent energy and momentum equations need to be solved with small time increments to prevent the smearing associated with numerical diffusion and preserve the sharpness of the oil-air interface. Flow characteristics and wall heat transfer of conventional impinging jets depend strongly on a number of aspects, such as confinement, nozzle geometry and flow conditions at the nozzle outlet. This explains the significant amount of effort devoted worldwide to this area of research.

Impinging jet is regarded as a method of achieving particularly high convective heat transfer coefficients and therefore enhances the heat transfer from the target (i.e., the disc or piston in this study). Using numerical simulation to predict the thermal characteristics with the presence of oil jet cooling will significantly help to select the proper design factors that will improve the performance of the engine. To achieve this goal, finite volume based computations using CD-adapco's STAR-CCM+ are performed in the current study for a variety of thermal and flow conditions with the aid of high performance computing (HPC). Correlations to predict the convective heat transfer coefficient are deduced and a methodology to accelerate the computational solution and reduce the cost in terms of CPU time is developed in the current study.

A general review for several aspects and some of the latest research reported in the literature on liquid jet impingement heat transfer is given in Chapter 2. To solve the

energy equation and to model turbulence and the dynamics of a set of immiscible fluids, solution to the transport equations of the relevant parameters needs to be coupled with the solver for the Navier-Stokes equations. In Chapter 3 we summarize the computational methodology and the segregated solvers required in the current study. Prior to launching a full-scale detailed investigation on the real engine, a generic model is used to enhance our understanding of the underlying physics of the problem. The thermal characteristics of jet impingement on to stationary and moving discs are investigated in Chapter 4 and 5, respectively. The simulation results of the entire engine with and without oil squirters are presented in Chapter 6. Transient simulation of Fiat-Chrysler's full-scale 2.0 L Tigershark Inline 4-Cylinder gasoline engine is used in our study. The convective heat transfer coefficient distribution on the piston wall and the temperature contours are computed to evaluate the performance of the cooling process by oil jet impingement. Lastly, the dissertation ends by summarizing the conclusions and recommending a possible path for future study.

## **CHAPTER 2**

### **LITERATURE REVIEW**

#### **2.1 Introduction**

This chapter reviews several aspects and some of the latest research on impinging liquid jets that has a consequence for the jet heat transfer problem investigated in this dissertation. The aim of this review is to provide a unified description of the fundamental and the technological aspects of this subject. Even though the impinging jet flow field constitutes a simple geometry, it poses extremely complex flow physics due to the different flow regions associated with the jet impingement process.

In industrial applications, jet flows can be classified based on the miscibility of the substances comprising the jet and surroundings, i.e., the ability of substances to mix and form a homogeneous solution. Thus, two common jets can be identified; miscible jets (referred to as submerged jets) or immiscible jets (referred to as unsubmerged or free surface jets). An example of miscible flow is a gas jet flowing into air, whereas a liquid jet issuing into the atmosphere is a case of immiscible flow. An immiscible jet has unstable boundaries and the stream is vulnerable to primary breakup or deflection some distance downstream from the nozzle. The range of such flow, that is, the distance over which the flow remains intact, depends on the physical properties of the substances and the amount of initial turbulence at the nozzle exit. The free surface type jet flow will be employed in the current study since they are involved in the localized cooling of the pistons in internal combustion engines.

Although single-phase jets have been most extensively employed in industry, two-phase jets are also important in some applications. Depending on the temperature difference between the wall and the saturation temperature of the jet liquid, impingement heat transfer may have two patterns; single-phase forced convection and forced convective boiling. In the current study, the saturated temperature of the engine oil is less than the temperature of the target (piston) and therefore convective transport without phase change is considered in our simulations.

According to the existing literature, the wall heat transfer for impinging jets is mainly determined by the specific flow and thermal condition of the issuing jet. The Nusselt number is often used as a measure of the heat transfer because it describes the physics in terms of fluid properties, making it independent of the target characteristics. The Nusselt number is commonly given as a function of Reynolds number,  $Re_d$ , and Prandtl number,  $Pr$ , in the form  $Re_d^m Pr^n$ .

## **2.2 Laminar and Turbulent Jets**

Elison & Webb (1994) investigated the transport of fully-developed liquid jets impinging normally on a surface for the flow regime  $300 \leq Re_d \leq 7000$  based on the nozzle exit conditions. The issuing jets were imaged for the full span of Weber and Reynolds numbers and the observations are summarized schematically in Figure 2.1. For very low Weber number (not shown in the figure), droplets begin to form at the nozzle tip and are torn off due to the gravity. As Weber number or Reynolds number increases, the droplets coalesce into a single stream attached to the nozzle exit. The stream exhibits surface instabilities immediately downstream of the exit as shown in Figure 2.1a. The



starting point of these instabilities moves downstream along the jet as the Weber number increases (the point of onset of the jet instabilities in Figures 2.1(b-d) are beyond the nozzle-to-plate spacing investigated by Elison & Webb, 1994). At low Weber number, the liquid jet boundary coincides with the outside diameter of the nozzle tube due to the surface tension effect. Therefore, the jet itself is larger than the internal diameter of the nozzle as shown in Figure 2.1(a-b). As Weber number increases, the free surface curvature at the nozzle exit increases and its diameter approaches the internal diameter of the nozzle as shown in Figure 2.1(c-d).

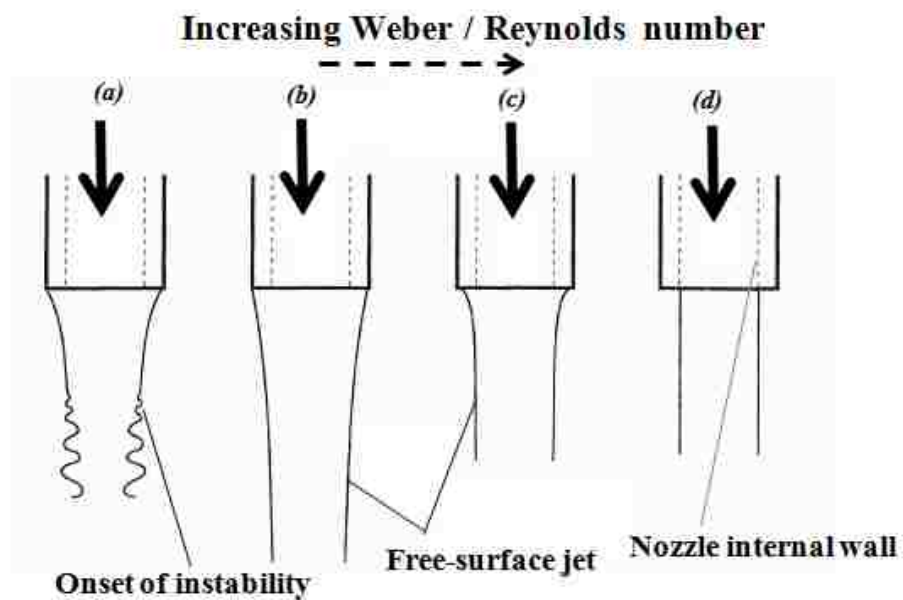


Figure 2.1: Schematic illustration of free-surface jet structure with increasing Weber number (or Reynolds number) (Elison & Webb, 1994)

Jets with a parabolic profile are normally produced by a laminar flow issuing from a long circular pipe nozzle at Reynolds numbers below 2000-4000. The parabolic

distribution of the velocity profile will persist if the target is within a few diameters downstream from the nozzle exit. If the jet is long enough for viscosity to act, this profile diffuses toward a uniform velocity profile as the jet moves to the target. For a longer jet column and at  $Re_d < 2000$ , the downward jet is likely to be contracted due to the gravitational acceleration and the surface tension effect, which becomes more significant at low Reynolds number.

Generally, the piping systems that provide liquid to nozzles are often turbulent. Turbulence is promoted by high flow velocities, low liquid viscosity, surface roughness and cavitation. The perturbations will be carried into the issuing jet unless the pipe nozzle has a very high contraction ratio. Turbulent jets have an elevated heat transfer coefficient owing to both the direct effect of free stream turbulence on the boundary layer and the more indirect effect of a nonuniform velocity profile on the stagnation point velocity gradient. The increase relative to laminar theory may range from 30-50% (Lienhard, 2006).

The stagnation zone boundary layer is likely to remain laminar over a wide range of jet Reynolds numbers, but turbulence in the impinging jet will tend to disrupt the thin viscous region, elevating the heat transfer coefficient. This effect is well documented for the stagnation zone in gas flow (Lowery & Vachon, 1975; Mehendale et al., 1991). For turbulent liquid impinging jets, a well defined turbulent nozzle is that of a fully-developed turbulent pipe flow. A liquid jet issuing from a tube of more than about 40 diameters in length without a terminating nozzle is a fully-developed turbulent pipe flow if the Reynolds number exceeds about 2000-4000. The roughness of the pipe wall controls the turbulence intensity at the nozzle exit. However, the turbulence intensities for

such flows do not exceed 4-5% in the core of the flow (Pope, 2000). Other types of nozzles may be less turbulent than pipe nozzles if they have a strong and well-contoured contraction at the outlet. It is worth mentioning that the jet free surface may remain laminar even with high Reynolds numbers as shown in Figure 2.2, whereas the wall roughness of the pipe nozzle specifies the disturbance level in the jet free surface.

Several researchers have adopted the pipe nozzle as a standard for turbulent liquid jets and the turbulence of such a jet is only defined by the jet Reynolds number and the nozzle diameter. The correlations have usually fit data to the form suggested by laminar theory, adjusting the lead constant and Reynolds number exponent. The Prandtl number exponent is normally chosen to be constant within a certain range (see section 2.7.1). Thus, the independent effects of free stream turbulence, Prandtl number and Reynolds number are lumped together in such results to produce a simple engineering equation. For this reason, the turbulence intensity parameter is missing in liquid jet impingement correlations that predict the heat transfer coefficient. The turbulence intensity effect on thermal characteristics will be further discussed in section 2.7.3.

In contrast to laminar profiles, which typically vary from uniform in long jets to parabolic in short jets (with  $v_{max} = 2v_f$ , where  $v_f$  is the bulk velocity of the jet flow), the velocity profile of turbulent pipe flow will likely vary between a uniform and mildly nonuniform distribution. However, the centreline velocity may be still significantly greater than the bulk velocity. For example, at  $Re_d = 4000$  in a circular tube,  $v_{max}/v_f = 1.27$ , while at  $Re_d = 10^5$ ,  $v_{max}/v_f = 1.18$  (Lienhard, 2006). The effect of velocity profile on the radial velocity gradient at the stagnation point is discussed in section 2.5.

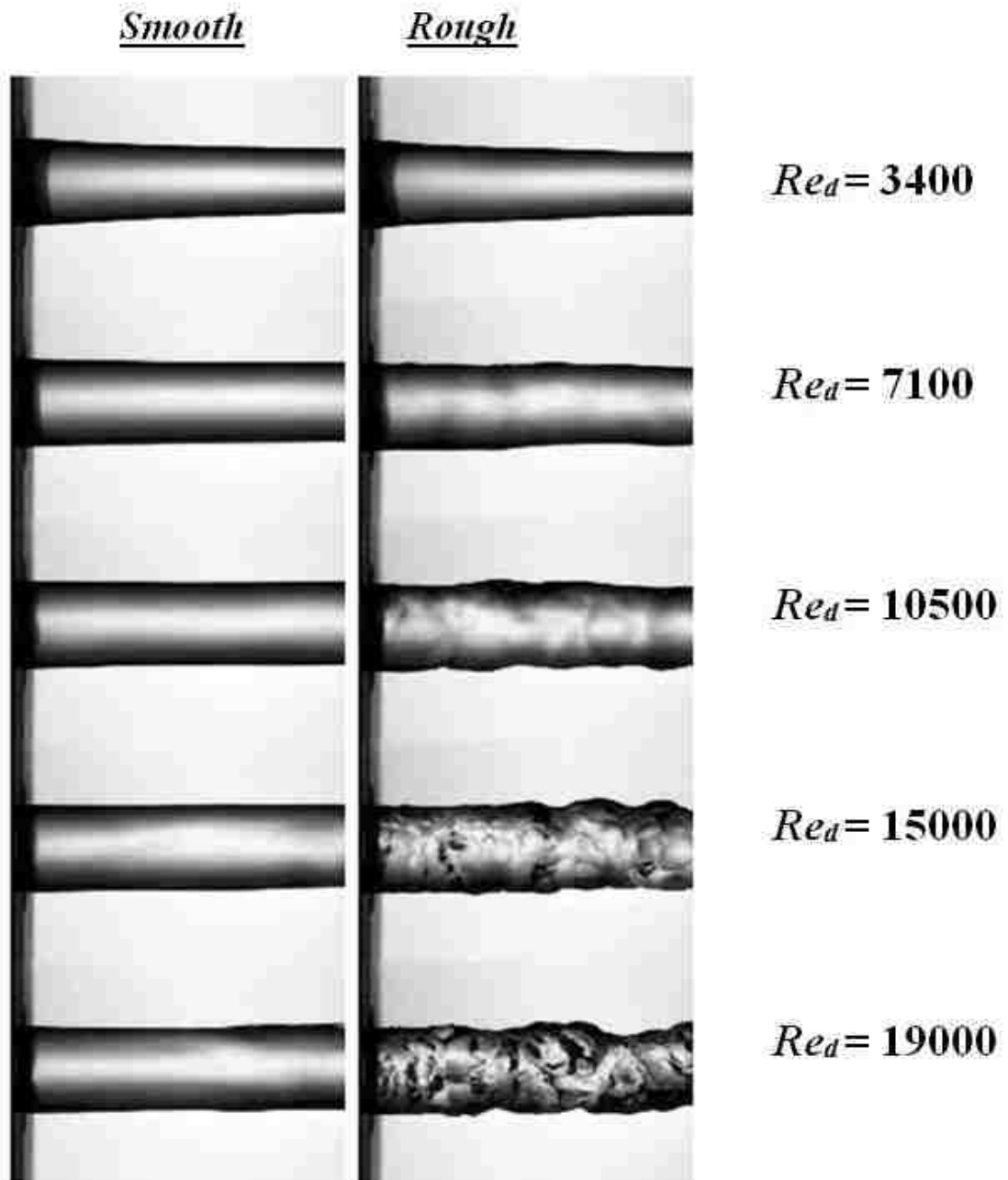


Figure 2.2: Surface profiles of a jet issuing from a smooth pipe (left), and a rough pipe (right), as a function of the Reynolds number (Eggers & Villermaux, 2008)

### 2.3 Splattering of Turbulent Liquid Jets

Turbulent liquid jets that impinge on solid surfaces often splatter violently, ejecting a shower of droplets from the liquid film formed on the target surface. The mechanism of the splattering was studied extensively by Bhunia & Lienhard (1994a,b), Lienhard et al. (1992) and Errico (1986). Strong splattering can result in atomization of 30-70% of the incoming liquid jet. The airborne droplets will no longer contribute to cooling the wall. The splattering has no influence on the heat transfer in the stagnation region because the droplets break away several diameters downstream of the stagnation point. Therefore, when the jet splatters, the cooling performance declines only downstream of the stagnation point. Lienhard et al. (1992) defined the fraction of impinging fluid splattered,  $\xi_s$ , as the ratio of the splattered flow rate,  $Q_s$ , to the incoming flow rate,  $Q$ .

The disturbance in a turbulent impinging jet is carried into the radially spreading liquid film. The turbulence has two contrary effects on the convective heat transfer in the locations close to the stagnation region; first, the fluctuation in the flow tends to enhance the mixing and elevates the convective heat transfer coefficient in the boundary layer downstream of the stagnation zone and promotes turbulent transition of the thin liquid film. The skin friction,  $c_f$ , will be greater with a turbulent liquid sheet in comparison with a laminar one. Stevens & Webb (1992) performed an experimental study to measure the free surface of the spreading liquid sheet. They found that the free-surface speed begins to drop at  $r/d \approx 2.5$  with the turbulent jet, sooner than predicted by laminar flow theory. This is attributed to the increase of the skin friction due to the turbulence. Second, the turbulence disturbs the surface of the incoming jet and this disturbance is carried into the liquid sheet. The radial spreading can produce a strong increase in the disturbance

amplitude. If the initial disturbances are large enough, the amplified disturbance in the spreading sheet can cause droplets to break away from the liquid sheet, resulting in splattering (Lienhard, 2006).

Investigations by Errico (1986) and Lienhard et al. (1992) suggest that splattering is only a consequence of the disturbances on the surface of the impinging jet, as shown in Figure 2.3(a-b). On the contrary, as shown in Figure 2.3c, undisturbed laminar jets do not splatter unless they are long enough to have developed significant disturbances from Rayleigh instability. Bhunia & Lienhard (1994a) investigated splattering for downwards turbulent water jets impacting solid targets. Their experiments cover Reynolds numbers between  $2700 < Re_d < 98,000$ , Weber numbers between  $130 < We_d < 31,000$ , and nozzle-to-target spacing between  $0.2 < H/d < 125$ . This study explicitly indicates that for a turbulent jet, the amount of splattering is governed by the level of surface disturbances present on the surface of the jet. At a given nozzle-target separation, the amount of splattering depends mainly on the jet Weber number. An empirical correlation is given in Bhunia & Lienhard (1994b) to predict the splattering ratio,  $\xi_s$ , as:

$$\xi_s = -0.258 + 7.85 \times 10^{-5} \omega_{spl} - 2.51 \times 10^{-9} \omega_{spl}^2 \quad (2.1)$$

where  $\omega_{spl}$  is the splattering parameter, which characterizes the rms amplitude of disturbance reaching the target. This parameter is defined as:

$$\omega_{spl} = We_d \exp\left(\frac{0.971 H}{\sqrt{We_d} d}\right) \quad (2.2)$$

The jet Weber number ( $We_d = \rho v_f^2 d / \sigma$ ) in equation (2.2) is based on the bulk jet velocity at the nozzle exit,  $v_f$ , the nozzle diameter,  $d$ , and the liquid surface tension,  $\sigma$ .

The expression given by equation (2.1) is valid for  $4400 < \omega_{spl} < 10000$ .

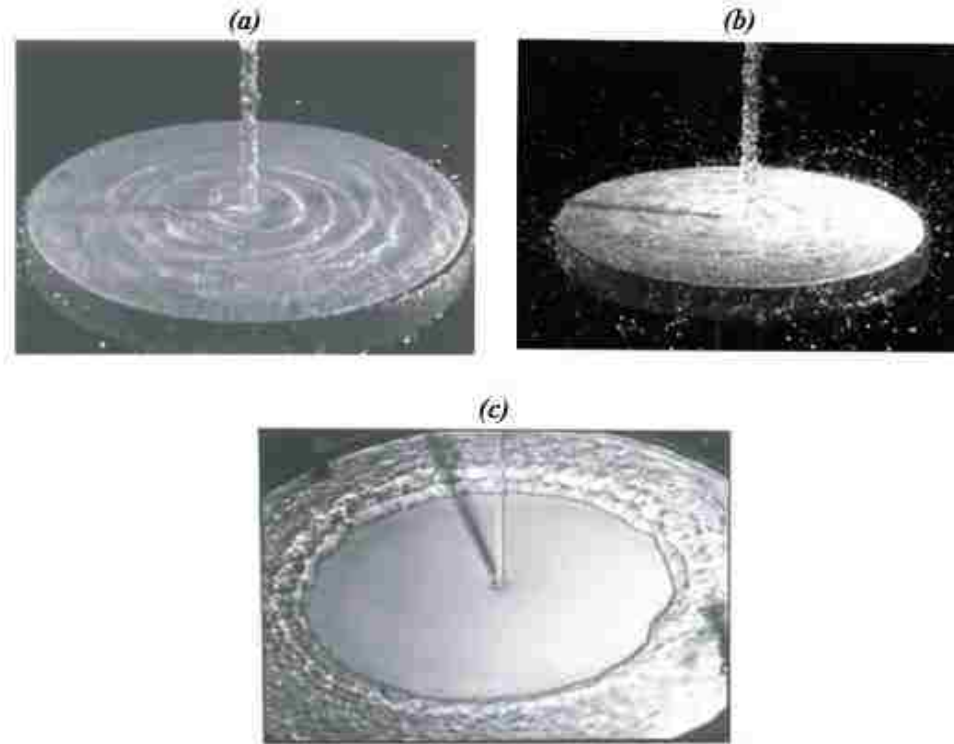


Figure 2.3: (a) Splattering turbulent jet issuing from fully-developed nozzle showing radially travelling wave,  $Re_d = 28,000$ ,  $\xi = 0.11$ , (b) Splattering turbulent jet issuing from fully-developed nozzle,  $Re_d = 48,300$ ,  $\xi = 0.31$ , (c) Laminar impinging jet issuing from contoured orifice,  $Re_d = 51,000$ ,  $d = 5.0$  mm (Lienhard, 2006)

## 2.4 Jet Impingement Flow Field

The initial region of the impinging jet, for large enough nozzle-to-target spacing, is characterized by free jet behaviour. A free jet can be defined as a jet entering a large container of quiescent fluid. When an axisymmetric free jet strikes a target, the flow field can be reasonably divided into an outer inviscid region and an inner viscous boundary layer. A very thin viscous layer initiates normal to the impingement axis and around the stagnation point, referred to as the stagnation zone. This layer exhibits little resistance

to heat flow, where the convective heat transfer coefficient reaches a large amount. Following impingement, the flow spreads thinner as it travels radially, the thickness of the liquid film adjacent to the wall decreases with radius. This decrease will bring the growing boundary layer into contact with the surface of the fluid film. The fluid film thickness begins to increase at larger radii due to the viscous drag, which slows down the flow and thickens the liquid layer. The hydrodynamics of this fluid film was theoretically studied by Watson (1964), who divided the flow field of the wall jet into five consecutive regions as shown in Figure 2.4; (1) the above mentioned stagnation zone region, (2) the laminar boundary layer region, in which the viscous layer thickness is less than the liquid film. In this region, the liquid film free surface is assumed to have the same velocity as the incoming jet, (3) the viscous similarity region, in which the viscous boundary layer extends through the liquid film, the surface velocity decreases as radius increases due to the viscous drag, (4) the transition region and (5) the fully turbulent flow region. Analytical analyses to predict a radial film flow were performed by Sharan & Hoshino (1984), Liu & Lienhard (1989), Liu et al. (1991), Azuma & Hoshino (1984a,b,c,d) and Lienhard (1995). These various studies are in relatively good agreement with one another. A brief discussion of the results from these studies is provided below.

Near the point of impact, a small viscous region is formed, referred to as the stagnation zone. The range of stagnation zone radius has been experimentally approximated by  $0.0 \leq r/d \leq 0.787$ . This region is often extremely thin; the 99% momentum boundary layer thickness for axisymmetric jet flow is given from theory as:

$$\delta_{Stag.} = \frac{2.76d}{\left[2 \left(\frac{d}{v_f}\right) \left(\frac{\partial u_r}{\partial r}\right)\right]^{0.5} Re_d^{0.5}} \quad (2.3)$$



where  $v_f$ , is the bulk velocity of the incoming jet and  $d$  is the nozzle diameter. The radial velocity gradient in equation (2.3) is evaluated just above the boundary layer region. Following the stagnation zone, a laminar transition region begins, where the flow transits to a laminar boundary layer. This region extends in the range  $0.787 \leq r/d \leq 2.23$ . The region of laminar boundary layer behaviour begins at  $r/d = 2.23$  and extends up to  $r/d < 0.1773Re_d^{1/3}$ , where the free-surface velocity  $u_s$  of the liquid sheet equals to the bulk velocity of the incoming jet. In this region, the boundary layer thickness is approximately

$$\delta = 2.679 \left( \frac{rd}{Re_d} \right)^{1/2}. \quad (2.4)$$

The velocity profile in this region is given by:

$$u_r(r, z) = u_s(r) \left[ \frac{3z}{2\delta} - \frac{1}{2} \left( \frac{z}{\delta} \right)^3 \right]. \quad (2.5)$$

The viscous boundary layer reaches the surface of the liquid sheet at a radius  $r_2$  given by:

$$\frac{r_2}{d} = 0.1773Re_d^{1/3}. \quad (2.6)$$

Beyond  $r_2$ , the free-surface speed decreases as:

$$u_s(r) = \frac{1}{5} \frac{v_f d^2}{t_s(r)r}. \quad (2.7)$$

The liquid sheet thickness,  $t_s(r)$ , in this region is given as:

$$t_s(r) = 0.1713 \left( \frac{d^2}{r} \right) + \frac{5.147}{Re_d} \left( \frac{r^2}{d} \right). \quad (2.8)$$

The velocity profile in this region is obtained by using equation (2.5) with surface velocity  $u_s$  from equation (2.7) and boundary layer thickness equal to film sheet thickness from equation (2.8).

The radii of onset of the turbulence and when the flow becomes fully turbulence have been correlated from experiments (Liu et al., 1991) as:

$$\frac{r_3}{d} = 1200Re_d^{-0.422}, \quad (2.9)$$

$$\frac{r_4}{d} = 28600Re_d^{-0.68}, \quad (2.10)$$

respectively. In light of the above equations and due to the existence of the confined boundary, the flow will not extend beyond the similarity region in our study.

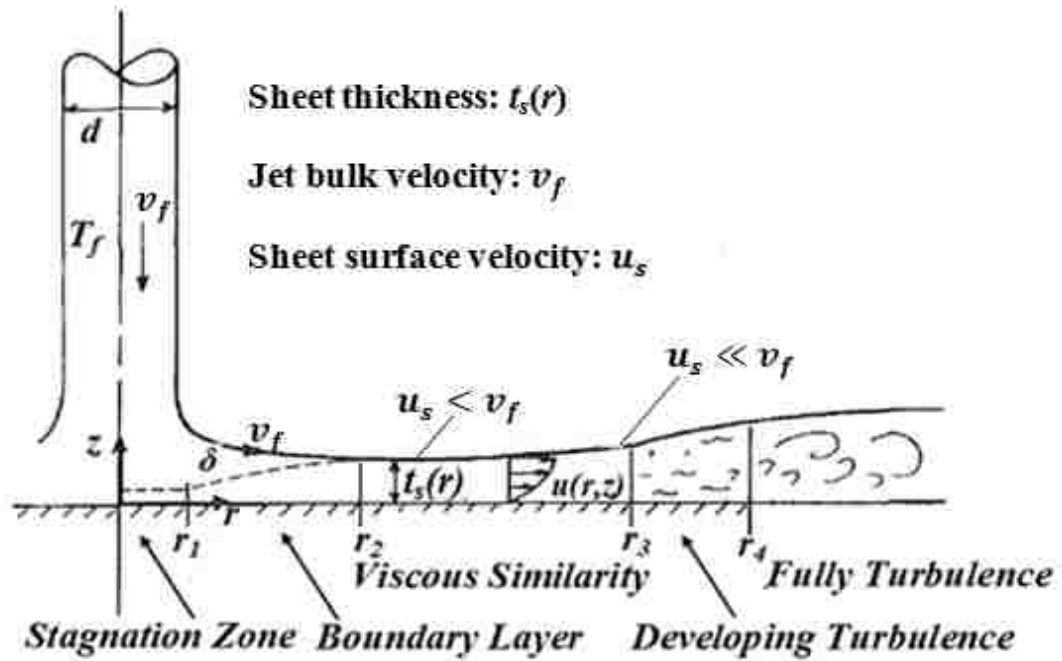


Figure 2.4: Jet and film flow showing hydrodynamic evolution

## 2.5 Radial Velocity Gradient at Stagnation Point

The radial velocity gradient at the stagnation point has a significant influence on the heat transfer coefficient (Vader et al., 1991; Burmeister, 1983; Donaldson et al., 1971). The analytical solution of the stagnation zone boundary layer is a classical problem,

whose results depend mainly on the radial velocity gradient of the inviscid flow near the stagnation point. Therefore, the analysis of the viscous stagnation region requires first the solution of the velocity field at the outer inviscid region from potential theory. It is worthwhile at this point to introduce a dimensionless velocity gradient,  $B$ , which will be used extensively in our study. This parameter is defined as (Lienhard, 2006):

$$B = 2 \left( \frac{d}{v_f} \right) \left( \frac{\partial u_r}{\partial r} \right)_{r \rightarrow 0}. \quad (2.11)$$

The gradient  $(\partial u_r / \partial r)_{r \rightarrow 0}$  is evaluated immediately just above the boundary layer.

An analytical solution for a uniform velocity profile of circular jets impinging normally onto a surface was found by Shen (1962) and by Strand (1964). They evaluated the dimensionless radial velocity gradient at the stagnation point as:

$$B = 1.831. \quad (2.12)$$

The radial velocity distribution at the stagnation region is evaluated from potential theory as:

$$\frac{u_r(r)}{v_f} = \frac{B r}{2 d}. \quad (2.13)$$

Wang et al. (1989) found for laminar jets that the radial velocity gradient at the stagnation point is a linear function of parameter  $v_f/d$ . Stevens & Webb (1991) concluded that the radial velocity gradient at the stagnation point also has an important effect on the heat transfer coefficient in turbulent jets. The parameter  $v_f/d$  may be used to functionally describe the stagnation velocity gradient in turbulent jets. Contrary to laminar jets, the turbulence may result in a slight non-linear dependence of the velocity gradient on the term  $v_f/d$ .

The velocity gradient at the stagnation point is strongly dependent on the velocity profile in the approaching jet. Stevens et al. (1992) carried out laser-doppler measurements of the radial velocity gradient for several turbulent flow nozzles located a distance of one nozzle diameter from the target. For a converging nozzle, the gradient was found to be  $B \approx 2.3$ . This type of nozzle would be expected to have the most nearly uniform velocity profile, and its stagnation point gradient is close to the uniform profile theoretical value, i.e.,  $B = 1.83$ . Corresponding measurements for a fully-developed pipe nozzle showed that  $B \approx 3.6$  (Stevens, 1991), well above the theoretical value. One may conclude that the variation in  $B$  among nozzles can have significant effects on turbulent jet heat transfer when the nozzle-to-target spacing is small. The effect of nozzle configuration on heat transfer coefficient will be further discussed in section 2.7.3.

All liquid jets will approach a uniform velocity profile when nozzle-to-target spacing increases, e.g., when  $H/d > 5.0$  (for water), because viscosity tends to eliminate the radial gradients within about five diameters downstream of the nozzle (Stevens & Webb, 1992). Therefore, for all long jets, the radial velocity gradient  $\partial u_r / \partial r$  at the stagnation point tends to be uniform, i.e.,  $B \rightarrow 1.83$  (theoretical value).

## **2.6 Liquid Jet Primary Breakup**

The next subsections discuss the deflection and primary breakup properties of round liquid jets in the absence and presence of a crossflow. Different regimes related to the primary breakup will be briefly presented. The discussion in this section is concerned with jets targeting downward.

### 2.6.1 Liquid Jet Breakup in Quiescent Medium

Rayleigh (1878) was among the first to study theoretically the breakup of round liquid jets. He postulated the growth of small disturbances that produce breakup when the fastest growing disturbance attains an optimum wavelength of  $4.51d$ . After breakup, the cylinder of length  $4.51d$  becomes a spherical drop, with  $D_{droplet} = 1.89d$ . Rayleigh's analysis took into account surface tension and inertial forces but neglected viscosity and the effect of the surrounding air. Weber (1931) later extended Rayleigh's work to include the effect of air resistance on the collapse of jets into drops. He found that air friction shortens the optimum wavelength for drop formation. For a relative velocity of 15 m/s, Weber concluded that the optimum wavelength becomes  $2.8d$  and the drop diameter becomes  $1.6d$ . Thus the effect of relative velocity between the liquid jet and the surrounding air is to reduce the optimum wavelength for jet breakup which results in a smaller drop size. At higher jet velocities, breakup is caused by waviness of the jet. This mode is associated with a reduction in the influence of surface tension and increased effectiveness of aerodynamic forces. At even higher velocities, this aerodynamic interaction causes irregularities in the previously smooth liquid surface. These irregularities or disturbances in the jet surface become amplified and eventually detach themselves from the liquid surface. Ligaments are formed which subsequently disintegrate into drops. As the jet velocity increases, the diameter of the ligaments decrease and the mean drop diameters become much smaller than the initial jet. At very high relative velocities atomization is complete within a short distance from the discharge orifice. A wide range of drop sizes is produced, with the mean drop diameter being considerably less than the initial jet diameter.

Laminar flow is promoted by low flow velocity, high liquid viscosity and the absence of any flow disturbances. With laminar flow, the velocity profile varies across the jet radius in a parabolic manner, rising from minimum value at the outer surface to a maximum at the jet axis. If a laminar jet is injected into quiescent or slow moving air, there is no appreciable velocity difference between the outer surface of the jet and the surrounding air. Therefore, the necessary conditions for jet breakup by air friction decreases. For long jets, surface irregularities develop that cause the jet to disintegrate into relatively large drops.

Many studies followed the Rayleigh (1878) and Weber (1931) investigations of liquid column breakup lengths and turbulent primary breakup properties at the surface of round liquid jets, e.g., Wu et al. (1992, 1995), Wu & Faeth (1993, 1995), Dai et al. (1998) and Sallam et al. (1999). An experimental study of turbulent liquid breakup lengths in still air at standard temperature and pressure was carried out by Sallam et al. (2002). In this study, the jet exit conditions were limited to non-cavitating water and ethanol flows, long length/diameter ratio (greater than 40:1), jet exit Reynolds numbers of 5000–200,000, jet exit Weber numbers of 235–270,000 and liquid/gas density ratios of 690 and 860, where direct effects of viscosity were small. Three liquid column breakup modes were observed in this investigation; first, a weak turbulent Rayleigh-like breakup mode due to the capillary instability for  $We_d < 300$ , where the liquid column breakup length,  $L_c$ , could be correlated as:

$$L_c/d = 0.5\sqrt{We_d}. \quad (2.14)$$

Second, a turbulent breakup mode for  $600 < We_d < 30000$ , when the drop diameter resulting from turbulent primary breakup becomes comparable to the diameter of the

liquid column itself. The underlying requirement for such breakup is that conditions at the jet exit must be turbulent, and the liquid column breakup lengths could be correlated as:

$$L_c/d = 2.1\sqrt{We_d}. \quad (2.15)$$

Third, an aerodynamic bag/shear breakup mode for  $We_d > 30,000$ , when small scale turbulence has disappeared and the liquid column is distorted in the cross stream direction by large-scale turbulence. The breakup mechanism that occurs in this mode is very similar to aerodynamic breakup of non-turbulent round liquid jets in gaseous crossflows. In this regime, the liquid column breakup lengths could be correlated as:

$$L_c/d = 8.51We_d^{0.32}. \quad (2.16)$$

The merging of turbulent primary breakup and secondary breakup occurs for liquid/gas density ratios smaller than 500 (Wu & Faeth, 1993). For such conditions, Sallam et al. (2002) stated that the aerodynamic effects on turbulent primary breakup are likely to differ from the behaviour observed in their investigations, where the liquid/gas density ratios is greater than 500.

### **2.6.2 Liquid Jet Breakup in Crossflow Medium**

The present study is concerned with heat transfer as a consequence of jet impingement in turbulent surroundings. This chaotic surrounding ensues because of the high reciprocating motion of the piston inside the cylinder. Therefore, the intact jet will be vulnerable to deflection or primary breakup before reaching the impingement surface due to the strong motion and turbulence of the gas in the contiguous ambient surroundings. It is worthwhile to define the dimensional variables of interest that play a

significant role in primary breakup of the liquid jet in crossflow. These are the thermodynamic densities of the liquid and gaseous phases, dynamic viscosities of the liquid and gaseous phases, diameter of the nozzle, velocity of the liquid jet at the nozzle exit, the normal velocity component of the gaseous phases to the liquid column and the interfacial surface tension. The following dimensionless groups are relevant to primary breakup of the liquid jet:

$$\text{Crossflow Weber number: } We_{cf} = \frac{\rho_g U_g^2 d}{\sigma} = \frac{\text{Inertia (gas)}}{\text{Surface tension}} \quad (2.17)$$

$$\text{Liquid Weber number: } We_{liq} = \frac{\rho_l V_l^2 d}{\sigma} = \frac{\text{Inertia (liq)}}{\text{Surface tension}} \quad (2.18)$$

$$\text{Ohnesorge number: } Oh = \frac{\mu_l}{\sqrt{\rho_l d \sigma}} = \frac{\text{Viscous (liq)}}{\text{Surface tension}} \quad (2.19)$$

$$\text{Momentum flux ratio: } q = \frac{\rho_l \left(\frac{V_l}{U_g}\right)^2}{\rho_g} = \frac{We_{liq}}{We_{cf}} \quad (2.20)$$

where the subscripts  $l$  and  $g$  refer to the liquid and gaseous phases, respectively.

The subject of a liquid jet in crossflow has been the focus of several experimental studies with the primary objective of understanding the phenomenon better and proposing physical models for liquid breakup. Various regimes of liquid breakup have been observed for round liquid jets in crossflow, and the effects of variation in physical variables that characterize both the liquid jet injection and crossflow have been investigated in these studies (Hsiang & Faeth, 1995; Mazallon et al., 1999; Sallam et al., 2004; Lee et al., 2007; Pai et al., 2008).

Wu et al. (1997, 1998) provided a phenomenological model for jet penetration based on their own experiments. Their work has become one of the key referenced works in this area. They modeled a liquid column as a circular column and applied a simple force



balance to obtain the jet trajectory using a regression analysis. Their measurements were done at normal temperatures and pressures with  $q$  ranging from 4 - 185 and crossflow subsonic Mach numbers of 0.2 to 0.4. They provided the following correlations:

$$\text{Liquid Column Trajectory: } \frac{y}{d} = 1.37 \sqrt{q \left( \frac{x}{d} \right)}. \quad (2.21)$$

$$\text{Height of Breakup Onset: } \frac{y_b}{d} = 3.44 \sqrt{q}. \quad (2.22)$$

$$\text{Axial Distance of Breakup Onset: } \frac{x_b}{d} = 8.06. \quad (2.23)$$

The formation of ligaments and drops along the liquid jet surface were studied experimentally by Sallam et al. (2004) using round non-turbulent liquid jets in air crossflow at normal temperature and pressure. Test conditions included water, ethyl alcohol, and glycerol jets injected normal to the crossflow for the following ranges of test variables; crossflow Weber numbers of 0 – 2000, liquid/gas momentum flux ratios of  $q = 3 – 8000$ , liquid/gas density ratios of  $\rho_l/\rho_g = 683 – 1033$ , and Ohnesorge numbers of  $Oh = 0.003 – 0.29$ . These investigations revealed that the effect of crossflow on primary jet breakup is weak for velocities corresponding to low Weber number,  $We_{cf} \leq 4$ . The liquid jet column is somewhat deformed, to yield an ellipsoidal cross section, and may be deflected in the direction of the crossflow velocity. This behaviour is caused by reduced gas pressures along the sides of the jet due to acceleration of the gas across the liquid jet associated with lateral motion of the liquid jet which is eventually stabilized by surface tension. The increased drag force due to the flattened shape of the liquid jet enhances its tendency to be deflected due to the gaseous crossflow.

Sallam et al. (2004) showed that the transitions between the various breakup regimes are not influenced significantly by liquid viscosities for  $Oh < 0.3$  and by liquid jet exit

velocities for  $q < 8000$ . Transitions to different breakup regimes, i.e., bag, multimode, and shear breakup, occurred at  $We_{cf} = 4, 30, \text{ and } 110$ , respectively. They also concluded that there were two regimes for both the onset of ligament formation along the liquid surface and for the variation of ligament diameter as a function of distance from the nozzle exit along the liquid surface. First, an initial transient regime associated with the growth of a shear layer thickness near the liquid surface that supplies liquid to the base of ligaments and, second, a quasi-steady regime where the shear layer thickness reaches its maximum possible growth within the confines of the round liquid jet and has a thickness that is a fixed fraction of the liquid jet diameter.

Pai et al. (2008) performed a computational study of a liquid jet in crossflow using the spectrally refined level-set method. This study revealed that for a constant crossflow Weber number, sizes of liquid surface disturbances on the windward side of the liquid jet decrease with increasing liquid Weber number, while the jet penetrates deeper into the domain with increase of the momentum flux ratio,  $q$ .

## **2.7 Thermal Characteristics of Liquid Impinging Jets**

In this section, we will introduce a general physical description of the convection mechanism and continue to describe the dimensionless parameters that characterize the convective heat transfer. A brief description of the empirical correlations found in the available literature that are used for prediction of the Nusselt number will be reviewed as well.

### 2.7.1 Physical Mechanism of Convection

Convection heat transfer is a complicated phenomenon that involves fluid motion as well as heat conduction. The fluid motion enhances heat transfer, since it brings hotter and cooler chunks of fluid into contact, initiating higher rates of conduction in a fluid. Therefore, the rate of heat transfer through a fluid is much higher by convection than it is by conduction. In fact, the higher the fluid velocity, the higher the rates of heat transfer. Convection heat transfer strongly depends on the fluid properties, i.e., dynamic viscosity,  $\mu$ , thermal conductivity,  $k$ , density,  $\rho$ , and specific heat,  $c_p$ , as well as the fluid velocity. It also depends on the geometry and the roughness of the solid surface, in addition to the type of fluid flow, whether laminar or turbulent (Cengel & Ghajar, 2011). Thus, we expect the convection heat transfer relations to be rather complex because of the dependence of convection on so many variables. This is not surprising, since convection is the most complex mechanism of heat transfer. Therefore, our final target is to predict the local or surface average heat transfer coefficient.

Due to the no-slip and no temperature jump conditions between the cooling or heating surface and the fluid layer adjacent to the surface, the heat transfer mechanism is purely conduction, since the fluid layer is motionless. The heat transfer at the solid-fluid interface can be expressed as (Cengel & Ghajar, 2011):

$$q''_w = q''_{cond.} = q''_{conv.} = -k_f \left( \frac{\partial T}{\partial y} \right)_{y=0} = h(T_{ref} - T_w) \quad (2.24)$$

where the subscripts  $w$ ,  $cond.$  and  $conv.$  represent the wall, conduction and convection respectively,  $(\partial T / \partial y)_{y=0}$ , is the temperature gradient at the solid-fluid interface,  $h$  is the heat transfer coefficient,  $k_f$  is the fluid thermal conductivity and  $T_{ref}$  is the reference temperature, which may be chosen as the bulk temperature of the fluid or any other

predefined temperature, depending on the nature of the problem. Equation (2.24) can be arranged in the form

$$\left[ \frac{\partial \left( \frac{T - T_w}{T_{ref} - T_w} \right)}{\partial (y/l)} \right]_{y/l=0} = \frac{hl}{k_f} = \frac{q''_{conv}}{q''_{cond}} = Nu \quad (2.25)$$

where,  $l$  is the characteristic length,  $y/l = 0.0$  represents the location at the fluid-solid interface and  $Nu$  is the local Nusselt number. The physical interpretation of Nusselt number is the enhancement of heat transfer through a fluid layer as a result of convection relative to conduction across the same fluid layer. The larger the Nusselt number, the more effective the convection. A Nusselt number of  $Nu = 1.0$  for a fluid layer represents heat transfer across the layer by pure conduction.

The local heat transfer coefficient,  $h$ , in a laminar boundary layer is a function of several physical parameters, represented as:

$$h = f(k_f, l, \rho, \mu, c_p, U_\infty, x) \quad (2.26)$$

where  $U_\infty$  is the free stream velocity just above the boundary layer and  $x$ , is the streamwise location. Using the dimensional analysis method for reducing the number of variables (White, 2009), the dimensionless groups from equation (2.26) are:

$$\text{Local Nusselt number: } Nu_x = f\left(\frac{x}{l}, \frac{U_\infty l \rho}{\mu}, \frac{\mu c_p}{k_f}\right) \quad (2.27)$$

$$\text{Average Nusselt number: } Nu = f\left(\frac{U_\infty l \rho}{\mu}, \frac{\mu c_p}{k_f}\right). \quad (2.28)$$

Normally, the experimental data for heat transfer is often represented with reasonable accuracy by a simple power-law relation of the form (Cengel & Ghajar, 2011):

$$Nu = C_g Re_l^m Pr^n \quad (2.29)$$

where  $m$  and  $n$  are constant exponents (usually between 0 and 1), the value of the constant  $C_g$  depends on the geometry and  $Pr$  is the Prandtl number. Prandtl number is a dimensionless parameter representing the ratio of diffusion of momentum to diffusion of heat in a fluid. The Prandtl numbers of gases are about 1.0, which indicates that both momentum and heat dissipate through the fluid at about the same rate. Heat diffuses very quickly in liquid metals ( $Pr < 1.0$ ) and very slowly in oils ( $Pr > 1.0$ ) relative to momentum. Consequently, the thermal boundary layer,  $\delta_t$ , is much thicker for liquid metals and much thinner for oils relative to the momentum boundary layer,  $\delta$ , (Hewitt et al., 1994).

In the jet impingement problem, the radial velocity gradient, which was discussed earlier, plays a crucial role in the specification of the heat transfer coefficient at the stagnation zone. Therefore, this parameter is expected to appear along with the Reynolds number and Prandtl number in equation (2.29). In jet impingement problems, the Reynolds number is normally calculated based on the nozzle exit properties. The Prandtl number dependence for liquid jet impingement has been characterized with exponent ranging from 0.33 to 0.487 (Jiji & Dagan, 1987; Ma & Bergles, 1983; Metzger et al., 1974).

### **2.7.2 Stagnation Zone and Local Nusselt Number**

The laminar boundary layer theory may be used to solve momentum and energy equations and evaluate the heat transfer coefficient in the stagnation region. The radial velocity distribution,  $u_r(r)$ , just above the boundary layer is required in the analytical solution. According to potential theory, this velocity is linear in  $r$  at the stagnation region,

where  $r$  is the radial coordinate (in cylindrical coordinates) from the stagnation point (see section 2.5). Solution of the laminar boundary layer for the stagnation region results in a heat transfer coefficient that is constant and independent of  $r$ , i.e., the thermal boundary layer has a uniform thickness within the stagnation region. The uniform value of heat transfer coefficient implies that uniform wall temperature and uniform heat flux produce an identical heat transfer coefficient.

From the laminar theory, the analytical solution for Nusselt number at the stagnation region shows the dependence of  $Nu_o$  on the stagnation point velocity gradient, i.e.,  $Nu_o \propto B^{0.5}$ . The expression is given as (Lienhard, 2006):

$$Nu_o = G(Pr)Re_d^{0.5}B^{0.5} \quad (2.30)$$

where the parameter  $G(Pr)$  is evaluated numerically within given ranges of Prandtl number. Equation (2.30) can be used to predict a theoretical value of stagnation zone Nusselt number for any jet whose stagnation point radial velocity gradient is known. It applies to either uniform wall temperature or uniform heat flux. However, one of the challenging issues is to obtain the radial velocity gradient at the stagnation point, which is highly dependent on the velocity profile of the incoming flow.

The laminar theory agrees well with experimental results when turbulence is eliminated in the impinging jet. The nozzle-to-target spacing has been shown to influence the laminar jets (Liu et al., 1991; Stevens & Webb, 1992) when (1) a sharp-edged nozzle is placed too close to the target to complete its contraction, so that the uniform profile is not attained, (2) the tube nozzle is placed far enough from the target that the viscosity diffuses the parabolic profile to a uniform profile, and (3) the jet velocity is low enough that gravitational acceleration causes significant variation in jet speed and size.

Liu et al. (1991) and Liu & Lienhard (1989) investigated analytically and experimentally the jet impingement process onto a uniform heated surface using free, uniform velocity laminar jets ( $2 \times 10^4 \leq Re \leq 1 \times 10^5$ ) in the absence of phase change. Analytical and numerical predictions were developed for a laminar radial film flow using the laminar theory (see also section 2.4). Integral solutions for the heat transfer in the viscous boundary layer and the similarity regions were obtained for Prandtl number greater than unity. Experiments using undisturbed laminar jets were performed to determine local Nusselt numbers from the stagnation point to radii of up to 40 diameters and to test the predictions of the theory. The agreement was generally good, and confirmed the predicted trends (Liu & Lienhard, 1989). Turbulent transition in the film flow was observed experimentally at a certain radius. Beyond this transition radius, a separate turbulent analysis was constructed. A brief review of Liu et al. (1991) and Liu & Lienhard (1989) findings are summarized below for  $Pr > 1.0$  (see also Figure 2.4).

At the region extending in the range  $0.787 < r/d < 2.23$  where the flow transits to a laminar boundary layer (this region is not shown in Figure 2.4), the local Nusselt number is given as:

$$Nu_d = \left\{ \frac{\frac{27}{80} Re_d Pr \frac{r}{\delta}}{\frac{1}{2} \left(\frac{r}{d}\right)^2 - 0.2535} \right\}^{1/3}. \quad (2.31)$$

For the boundary layer region,  $2.23 < r/d < 0.1773 Re_d^{1/3}$ , the local Nusselt number is given as:

$$Nu_d = 0.632 Re_d^{0.5} Pr^{1/3} \left(\frac{d}{r}\right)^{0.5}. \quad (2.32)$$

The similarity viscous region follows the laminar boundary layer region where the viscous effect extends through the entire liquid film,  $0.1773Re_d^{1/3} < r/d < 1200Re_d^{-0.422}$ , and the local Nusselt number is given as:

$$Nu_d = \frac{0.407Re_d^{1/3} Pr^{1/3} (d/r)^{2/3}}{\left[0.1713(d/r)^2 + \frac{5.147r}{Re_d d}\right]^{2/3} \left[\frac{1}{2}(r/d)^2 + C_{2-3}\right]^{1/3}} \quad (2.33)$$

where the constant,  $C_{2-3}$  is evaluated as:

$$C_{2-3} = \frac{0.267(d/r_2)^{1/2}}{\left[0.1713(d/r_2)^2 + \frac{5.147r_2}{Re_d d}\right]^2} + \frac{1}{2} \left(\frac{r_2}{d}\right)^2 \quad (2.34)$$

Liu et al. (1991) also predicted the turbulent heat transfer using the thermal law of the wall (thermal law of the wall is discussed in Chapter 3). Experiments showed that the turbulent region begins at  $r/d > 2.86 \times 10^4 Re_d^{-0.68}$ . The thermal law of the wall may be expressed as:

$$St = \frac{c_f/2}{1.07 + 12.7(Pr^{2/3} - 1)(c_f/2)^{0.5}} = f(c_f, Pr) \quad (2.35)$$

where  $St$  is the Stanton number, defined as:

$$St = \frac{q''_w}{\rho c_p u_s (T_w - T_s)} \quad (2.36)$$

The skin friction coefficient,  $c_f$ , used in equation (2.35) is calculated from Blasius' law using a 1/7 power turbulent velocity distribution. The skin friction in this region is given as:

$$c_f = 0.073Re_d^{-0.25} \left(\frac{r}{d}\right)^{0.25} \quad (2.37)$$

When  $Pr \gg 1.0$ , the Nusselt number in this region is given as:



$$Nu_d = 0.0052 Re_d^{3/4} \left( \frac{d}{t_s(r)} \right) \left( \frac{d}{r} \right)^{3/4} \left( \frac{Pr}{1.07 + 12.7(Pr^{2/3} - 1)(c_f/2)^{0.5}} \right). \quad (2.38)$$

The sheet thickness,  $t_s(r)$ , and the velocity distribution in the turbulent region is defined in Liu et al. (1991).

Liu & Lienhard (1989) also showed that if  $Pr > 4.859$ , the thermal boundary layer never reaches the surface of the liquid film because the growth of the thermal boundary layer is slower than the thickening of the liquid film caused by viscous retardation. The experimental results show that the local Nusselt number is not uniform at the stagnation region as concluded from the analytical studies, but it is a function of the radial distance from the stagnation point. The local Nusselt number reaches its maximum at some radial distance away from the point of impact and then decreases as the radius increases further. Both the magnitude and radial position of the maximum Nusselt number increase with Reynolds number. The wall temperature rises steadily away from the stagnation point.

An experimental study to characterize the heat transfer coefficient for round fully-developed turbulent liquid jets impinging normally onto a uniform heat flux surface was carried out by Stevens & Webb (1991) with varying nozzle diameters and flow conditions. Smooth glass tubes with inside diameters 2.2, 4.1, 5.8 and 8.9 mm were employed as pipe nozzles. The investigation revealed that the Nusselt number in the region near the stagnation point was distinctly dependent on Reynolds number,  $Re_d$ , Prandtl number,  $Pr$ , and radial velocity gradient,  $\partial u_r / \partial r$ , and less dependent on nozzle-to-target spacing,  $H$ . Inclusion of the velocity gradient as an important parameter suggests  $B = 2(d/v_f)(\partial u_r / \partial r)$  as the obvious non-dimensional velocity gradient. However, there is no available method for measuring  $\partial u_r / \partial r$  at the stagnation point, leaving only

the dimensional term  $d/v_f$  to estimate the gradient. The drawback of using  $d/v_f$  as a correlating parameter is its dimensional nature, and there is no obvious reference time scale for use in its normalization. Taking into account the effects of  $d/v_f$  and the dimensionless parameters  $Re_d$ ,  $Pr$  and  $H/d$ , an empirical relation for the stagnation point Nusselt number was reported in Stevens and Webb (1991) as:

$$Nu_o = 2.67Re^{0.567}Pr^{0.4}(H/d)^{-0.0336}(d/v_f)^{0.237}. \quad (2.39)$$

Equation (2.38) is valid for  $4000 < Re_d < 52000$  and predicts the experimental data with an average and maximum error of 5% and 14%, respectively, for all nozzles sizes used in the experiments. In this study, all fluid properties were evaluated at the nozzle exit. As reflected by the small exponent of  $H/d$  in equation (2.39), the effect of the nozzle-to-target spacing on Nusselt number is insignificant.

An equation to predict the local Nusselt number was also suggested for the region that extends radially to the onset of turbulence (Stevens & Webb, 1991):

$$\frac{Nu}{Nu_o} = \left[ 1 + (a_{sw}e^{b_{sw}(r/d)})^{-9} \right]^{-1/9} \quad (2.40)$$

where  $a_{sw}$  and  $b_{sw}$  are constants, but vary for each nozzle size. This correlation applies only to the region before transition occurs. Beyond that point, the correlation serves as a lower bound on the local heat transfer, but does not accurately predict local Nusselt number.

Other empirical correlations to predict stagnation zone Nusselt number are given in Lienhard (2006). However, all these correlations are limited to specific ranges of Reynolds number and Prandtl number.

### 2.7.3 Effect of Nozzle Configuration

The effect of nozzle configuration on transport and heat transfer coefficient in the stagnation zone was experimentally investigated by Stevens et al. (1992) and Pan et al. (1992) using small nozzle-to-target spacing. Four different nozzle exit conditions were studied, including fully-developed pipe flow, contoured nozzle, and turbulence-damped and turbulence sharp-edged orifice. A liquid jet Reynolds number in the range 30,000 - 55,000 and nozzle-to-target spacing  $H/d < 0.8$  were employed in the investigation. Stevens et al. (1992) revealed that the mean radial velocities vary nearly linearly with radial location from the impinging point. For short nozzle-to-target spacing, the dimensionless mean velocity gradients, of relevance to the heat transfer, were found to be a strong function of nozzle type. Turbulence levels were also found to be strongly influenced by the nozzle exit condition. The maximum turbulence intensities associated with fully-developed and contoured orifice nozzles used in the investigation were found to be less than 5% (Stevens et al., 1992). One of the major outcomes from this study was that the increase in turbulence intensity at the nozzle exit resulted in only minor changes in the radial velocity gradient but yielded substantial differences in the turbulent fluctuations of the radial velocity component. This radial fluctuation will enhance the splattering downstream from the impinging point.

Pan et al. (1992) also investigated the thermal characteristics of turbulent jet impingement for the previous four nozzles configurations. The results showed that for short nozzle-to-target spacing ( $H/d < 0.8$ ) and identical jet Reynolds numbers, significant differences of approximately 40% exist in the magnitudes of Nusselt number.

A correlation to predict stagnation zone Nusselt number was established by Pan et al. (1992) as  $Nu_0 = f(Re_d, u'_r/v_f, B)$ . This correlation is given as:

$$Nu_0 = 0.72Re_d^{0.53}B^{0.63}(u'_r/v_f)^{-0.022} \quad (2.41)$$

where  $u'_r$  is the fluctuation component in the radial direction. From equation (2.41), the dependence of stagnation zone Nusselt number on turbulence level is negligible since the exponent of the parameter  $(u'_r/v_f)$  is very small. Moreover, the effect of the radial velocity gradient is dominant in equation (2.41). Hence, the Reynolds number and velocity gradient appear to be of primary importance for heat transfer in turbulent, liquid free-surface jets (Pan et al., 1992). In light of this, the term  $(u'_r/v_f)$  may be dropped from the relation, yielding a revised correlation:

$$Nu_0 = 0.334Re_d^{0.53}B^{0.58}Pr^{0.4} \quad (2.42)$$

The empirical correlation given by equation (2.42) is used to predict stagnation zone Nusselt numbers for short nozzle-to-target spacing, i.e.,  $H/d < 0.8$ . This correlation represents all of the experimental data with a maximum error of 4% (Pan et al., 1992). Finally, for all Reynolds numbers in the range 30,000 - 55,000, the sharp-edged orifice without turbulence damping screens provided the highest heat transfer coefficients, followed by the sharp-edged orifice with turbulence damping screens, the fully-developed pipe nozzle, and finally the contoured orifice.

## 2.8 Conclusions

This chapter includes a general review of previous research concerned with flow and thermal characteristics of impinging liquid jets. A number of important conclusions from this chapter may be summarized as follows:

- A very thin viscous layer initiates normal to the impingement axis and around the stagnation point, referred to as the stagnation zone. This layer exhibits little resistance to heat flow, where the convective heat transfer coefficient reaches a considerable amount.
- The radial velocity gradient  $\partial u_r / \partial r$  has a significant effect on the heat transfer coefficient in the stagnation zone; this gradient depends primarily on the jet velocity profile. However, all liquid jets will approach a uniform velocity profile when nozzle-to-target spacing increases, because viscosity tends to eliminate the radial gradients within a certain distance downstream of the nozzle. Therefore, for all long jets, the radial velocity gradient in the stagnation region tends to be uniform.
- The radial velocity gradient at the stagnation point was found to be a linear function of  $v_f / d$  in laminar jets, where  $v_f$  is the bulk velocity at the nozzle exit. However, a turbulent jet may result in a non-linear dependence between  $\partial u_r / \partial r$  and  $v_f / d$ .
- The heat transfer coefficient at the stagnation region is mainly dependent on the dimensionless quantities  $Re_d$ ,  $Pr$  and  $H/d$  as well as the dimensional quantity  $\partial u_r / \partial r$ . The effect of nozzle-to-target parameter  $H/d$  is insignificant for long jets and can be neglected.
- The effect of nozzle configuration on heat transfer coefficient is significant for short jets, i.e.,  $H/d < 1.0$ . The turbulence level is strongly influenced by the nozzle exit

conditions and the wall roughness. The dependence of the stagnation zone Nusselt number on turbulence level is negligible since the effect of  $(u'_r/v_f)$  is very small and the radial velocity gradient is more dominant.

- Splattering can result in ejecting a shower of droplets from the liquid film formed on the target surface. The splattering is only a consequence of the disturbances on the surface of the impinging jet. Splattering has no influence on the heat transfer in the stagnation region because the droplets break away several diameters downstream of the stagnation point. Therefore, when the jet is splattering, the cooling performance declines only downstream of the stagnation point.
- The investigations reveal that the effect of crossflow on primary jet breakup is weak for velocities corresponding to Weber number  $We_{cf} \leq 4$ , liquid/gas momentum flux ratios of  $q = 3 - 8000$  and liquid/gas density ratios of  $\rho_l/\rho_g = 683 - 1033$ . The liquid jet column is somewhat deformed, to yield an ellipsoidal cross section, and may be deflected in the direction of the crossflow velocity. Therefore, the indirect effect of crossflow on stagnation zone heat transfer is insignificant when jet Weber number is less than four.
- All previous studies to predict heat transfer coefficient as a consequence of jet impingement were conducted for a stationary target. There does not appear to be any studies for jet impingement onto a target moving reciprocally against the liquid jet.

## CHAPTER 3

### COMPUTATIONAL METHODOLOGY

#### 3.1 Introduction

In the current study, a computational analysis using the finite volume approach is used to solve the heat transfer problem associated with jet cooling. The finite volume method (FVM) is a methodology for representing partial differential equations in the form of algebraic equations. It is one of the most versatile discretization techniques in CFD. The first step in FVM is to divide the solution domain into a number of control volumes where the variables of interest are located at the centroid of the control volume. The next step is to integrate the differential form of the governing equations over each control volume. The volume integrals resulting from a partial differential equation that contains divergence terms are converted to surface integrals, using the divergence theorem. These terms are then evaluated as fluxes at the surfaces of each control volume. The FVM approach guarantees local conservation of the fluid property for each control volume. Numerical schemes which possess the conservativeness property also ensure global conservation of the fluid property for the entire domain. Also, all flow processes contain effects due to convection and diffusion. In diffusive phenomena, a change of fluid property at one location affects the property in more or less equal measure in all directions around it. On the other hand, convective phenomena involve influencing exclusively in the flow direction. FVM with the transportiveness property must account for all directionality of influencing in term of the relative strength of diffusion to convection. The other advantage of the FVM is that it is easily formulated to allow for either a structured or unstructured mesh.

### 3.2 Governing Equation

This section describes the basics of the finite volume discretization methods used in STAR-CCM+ (from CD-adapco). The general conservative differential form of the equations governing the time dependent three-dimensional flow and heat transfer of a Newtonian fluid is given as (Versteeg & Malalasekera, 2007; Anderson, 1995):

$$\frac{\partial \rho \phi}{\partial t} + \nabla \cdot (\rho \phi \mathbf{u}) = \nabla \cdot (\Gamma_\phi \nabla \phi) + S_\phi. \quad (3.1)$$

Equation (3.1) is also referred to as the transport equation for the property  $\phi$ . The terms in this equation represent, from left to right, the local acceleration, the convective flux, the diffusive flux and the volumetric source (including pressure gradients and gravitational force). The set of Navier-Stokes equations is obtained by setting the variable  $\phi$  in equation (3.1) to  $1, u, v, w$  and  $T$  and selecting appropriate expressions for the diffusion coefficient  $\Gamma_\phi$  and source term. Equation (3.1) is used as the starting point for computational procedures in the finite volume method. The key first step of the finite volume method is the integration of equation (3.1) over a three-dimensional control volume (CV). The integral form of the general transport equation (assuming a fixed control volume) can be written as (Versteeg & Malalasekera, 2007):

$$\frac{\partial}{\partial t} \int_{CV} \rho \phi dV + \int_{CV} \nabla \cdot (\rho \phi \mathbf{u}) dV = \int_{CV} \nabla \cdot (\Gamma_\phi \nabla \phi) dV + \int_{CV} S_\phi dV. \quad (3.2)$$

Using Gauss' divergence theorem, equation (3.2) can be written as:

$$\frac{\partial}{\partial t} \int_{CV} \rho \phi dV + \oint_A \mathbf{n} \cdot (\rho \phi \mathbf{u}) dA = \oint_A \mathbf{n} \cdot (\Gamma_\phi \nabla \phi) dA + \int_{CV} S_\phi dV \quad (3.3)$$

where  $\mathbf{n}$  is the unit normal vector to the surface element  $dA$ . The discrete form can be obtained by applying equation (3.3) to a cell-centred control volume for a representative cell 0. The source term in the right side of equation (3.3) is approximated by the product



of the value of the integrand,  $S_\phi$ , evaluated at the cell centroid, and the cell volume,  $V$ .

The discrete form of equation (3.3) can be written as (STAR-CCM+ Manual, 2012):

$$\frac{d}{dt}(\rho\phi V)_0 + \sum_f [\rho\phi(\mathbf{u} \cdot \mathbf{A})]_f = \sum_f [\Gamma_\phi \nabla\phi \cdot \mathbf{A}]_f + (S_\phi V)_0 \quad (3.4)$$

where  $\mathbf{A}$  is the area vector ( $\mathbf{A} = \mathbf{n}A$ ), the subscripts 0 and  $f$  in equation (3.4) refer to a cell 0 quantity and a face quantity, respectively.

The following subsections describe the approximations employed when writing each term in equation (3.4) as functions of the cell variables.

### 3.2.1 Transient Term

In STAR-CCM+, the transient term is only included in actual transient calculations and it is not generally used as a device to obtain a steady-state solution. The implicit unsteady solver offers two temporal discretization options; first-order and second-order. In our study, a first-order temporal discretization will be used with the implicit unsteady solver.

The first-order temporal scheme, also referred to as Euler implicit, discretizes the unsteady term using the solution at the current time level,  $n+1$ , as well as the one from the previous time level,  $n$ , as follows (STAR-CCM+ Manual, 2012):

$$\frac{d}{dt}(\rho\phi V)_0 = \frac{(\rho_0\phi_0)^{n+1} - (\rho_0\phi_0)^n}{\Delta t} V_0 \quad (3.5)$$

### 3.2.2 Convective Term

The convective term at a face is discretized as:

$$[\rho\phi(\mathbf{u} \cdot \mathbf{A})]_f = (\dot{m} \phi)_f = \dot{m}_f \phi_f \quad (3.6)$$

where  $\phi_f$  and  $\dot{m}_f = [\rho(\mathbf{u} \cdot \mathbf{A})]_f$  are the scalar value and mass flow rate at the face, respectively. The manner in which the face value  $\phi_f$  is computed from the cell values has a significant effect on the stability and accuracy of the numerical scheme. Several schemes are commonly available to evaluate  $\phi_f$ , such as first-order upwind, second-order upwind, central differencing, hybrid second-order upwind/central, etc.

Generally, first-order schemes introduce a dissipative error that is stabilizing and helps the solver achieve robust convergence. However, the numerical dissipation has the effect of smearing discontinuities, especially if those discontinuities are not aligned with the grid lines. A description of the relevant schemes for the convective fluxes is provided below.

For a second-order upwind scheme, the convective flux is computed as:

$$\dot{m}_f \phi_f = \begin{cases} \dot{m}_f \phi_{f,0} & \dot{m}_f \geq 0 \\ \dot{m}_f \phi_{f,1} & \dot{m}_f < 0 \end{cases} \quad (3.7)$$

where the face values  $\phi_{f,0}$  and  $\phi_{f,1}$ , are linearly interpolated from the cell values on either side of the face as follows:

$$\phi_{f,0} = \phi_0 + (\mathbf{x}_f - \mathbf{x}_0) \cdot (\nabla \phi)_{r,0} \quad (3.8)$$

$$\phi_{f,1} = \phi_1 + (\mathbf{x}_f - \mathbf{x}_1) \cdot (\nabla \phi)_{r,1} \quad (3.9)$$

where  $\mathbf{x}_f$  is the position vector to a point on the cell face,  $\mathbf{x}_0$  and  $\mathbf{x}_1$  are the position vectors of the cell centroids,  $(\nabla \phi)_{r,0}$  and  $(\nabla \phi)_{r,1}$  are the limited reconstruction gradients in cells 0 and 1 respectively, and the subscript  $r$  denotes the reconstructed value. The fact that the reconstructed gradients are limited helps to reduce the numerical dissipation and improve the accuracy (STAR-CCM+ Manual, 2012). The disadvantage is that, in some situations, the reduced numerical dissipation might result in lower convergence properties

than the first-order accurate schemes. Generally, this is an acceptable trade-off. Limited reconstruction gradients are discussed in section 3.4.

For a central differencing scheme, the convective flux is computed as:

$$\dot{m}_f \phi_f = \dot{m}_f [(\beta_g \phi_0 + (1 - \beta_g) \phi_1)] \quad (3.10)$$

where  $\beta_g$  is the geometric weighting factor, related to the mesh stretching. The value of this factor is 0.5 for a uniform mesh. The central differencing scheme is formally second-order accurate, however, it is prone to dispersive error.

Finally, for both the second-order upwind or central differencing schemes, the flux at a boundary face is evaluated as:

$$\dot{m}_f \phi_f = \begin{cases} \dot{m}_f \phi_{f,0} & \dot{m}_f \geq 0 \\ \dot{m}_f \phi_f & \dot{m}_f < 0 \end{cases} \quad (3.11)$$

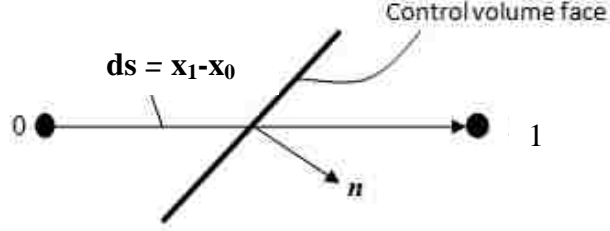
where  $\phi_{f,0}$  is interpolated from the cell value using the limited reconstruction gradients in cell 0 (from equation (3.8)) and  $\phi_f$  is the face value that is imposed by the boundary conditions.

### 3.2.3 Diffusion Term

The discrete form of the diffusion term in equation (3.4) is given as:

$$D_f = [\Gamma_\phi \nabla \phi \cdot \mathbf{A}]_f \quad (3.12)$$

where  $\Gamma_\phi$ ,  $\nabla \phi$  and  $\mathbf{A}$  represent the face diffusivity, gradient and area vector ( $\mathbf{n}A$ ), respectively. To obtain an accurate second-order expression for an interior face gradient that implicitly involves the cell values  $\phi_0$  and  $\phi_1$ , the following decomposition is used (STAR-CCM+ Manual, 2012):



$$\nabla\phi_f = (\phi_1 - \phi_0)\alpha_m + \overline{\nabla\phi} - (\overline{\nabla\phi} \cdot \mathbf{ds})\alpha_m \quad (3.13)$$

where  $\alpha_m$  is a face metric quantity, defined as:

$$\alpha_m = \frac{\mathbf{n}}{\mathbf{n} \cdot \mathbf{ds}} \quad (3.14)$$

and

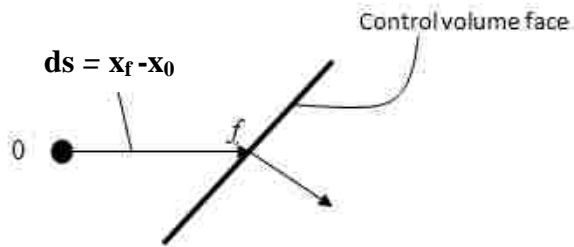
$$\overline{\nabla\phi} = \frac{(\nabla\phi_0 + \nabla\phi_1)}{2}. \quad (3.15)$$

The second and third terms in equation (3.13) represent the secondary gradient contribution. They are essential for maintaining accuracy on non-orthogonal meshes (STAR-CCM+ Manual, 2012).  $\nabla\phi_0$  and  $\nabla\phi_1$  are the cells 0 and 1 gradients. Then the diffusion flux in equation (3.12) at an interior face may be written as:

$$D_f = [\Gamma_\phi \nabla\phi \cdot \mathbf{A}]_f = \Gamma_{\phi_f} [(\phi_1 - \phi_0)\alpha_m \cdot \mathbf{A} + \overline{\nabla\phi} \cdot \mathbf{A} - (\overline{\nabla\phi} \cdot \mathbf{ds})\alpha_m \cdot \mathbf{A}]. \quad (3.16)$$

The diffusion coefficient  $\Gamma_{\phi_f}$  is obtained by averaging the cell values on either side of the face.

At a boundary face, a similar decomposition is used:



$$[\Gamma_\phi \nabla\phi \cdot \mathbf{A}]_f = \Gamma_{\phi_0} [(\phi_f - \phi_0)\alpha_m \cdot \mathbf{A} + \nabla\phi_0 \cdot \mathbf{A} - (\nabla\phi_0 \cdot \mathbf{ds})\alpha_m \cdot \mathbf{A}]. \quad (3.17)$$

### 3.3 Reconstruction Gradient

In our study, the Green-Gauss gradient method is used to compute reconstruction gradients, i.e.,  $(\nabla\phi)_r$ . For the Green-Gauss gradient method, the weighted least squares method is used for pressure, while the simple Gauss method is used for all variables other than pressure.

In the weighted least square method, the ultimate reconstruction gradients in cell 0 are computed using the following formula (STAR-CCM+ Manual, 2012):

$$(\nabla\phi)_r^u = \left[ \sum_f \frac{(\phi_0 - \phi_m)\mathbf{ds}}{\mathbf{ds} \cdot \mathbf{ds}} \right] / \left[ \sum_f \frac{\mathbf{ds} \otimes \mathbf{ds}}{\mathbf{ds} \cdot \mathbf{ds}} \right] \quad (3.18)$$

where the superscript  $u$  refers to ‘ultimate’ reconstruction gradient and the symbol " $\otimes$ " denotes the outer product of two vectors. The outer product of two vectors is a tensor, i.e.,  $\mathbf{ds} \otimes \mathbf{ds}$  is equivalent to the matrix multiplication  $\mathbf{dsds}^T$ .

In the Gauss method, the ultimate reconstruction gradients in cell 0 are computed using the Gauss' divergence theorem (STAR-CCM+ Manual, 2012):

$$\int_V \nabla\phi \, dV = \oint_A \phi \, d\mathbf{A} . \quad (3.19)$$

The discrete form of equation (3.19) can be written as

$$(\nabla\phi)_r^u = \frac{1}{V_0} \sum_f \phi_f \mathbf{A}_f \quad (3.20)$$

and the face value is approximated by the arithmetic average of the adjacent cell values:

$$\phi_f = \frac{\phi_0 + \phi_1}{2}. \quad (3.21)$$

### 3.4 Reconstruction Gradient Limiting

The problem with simply reconstructing face values from the unlimited reconstruction gradients is that the reconstructed values may exceed the cell values bounding the face. For this reason, it is necessary to limit the reconstruction gradients by scaling them appropriately in each cell. For each cell 0, a limited reconstruction gradient is required. The reconstructed face value used in equation (3.8) should not exceed the maximum and minimum of the neighbouring cell centroid values, including the value in cell 0. Thus, for each cell 0, the limited reconstructed gradient is approximated as:

$$(\nabla\phi)_{r,0} = \alpha_{lim.}(\nabla\phi)_{r,0}^u \quad (3.22)$$

where  $\alpha_{lim.}$  is a scalar factor that expresses the ratio of the limited and unlimited values.

Also, for each cell 0 the following quantities are defined:

$$\phi_0^{max} = \max(\phi_0, \phi_{neighbours}) \quad (3.23)$$

$$\phi_0^{min} = \min(\phi_0, \phi_{neighbours}) \quad (3.24)$$

$$\Delta_{max} = \phi_0^{max} - \phi_0 \quad (3.25)$$

$$\Delta_{min} = \phi_0^{min} - \phi_0 \quad (3.26)$$

where  $\phi_{neighbours}$  represents the cell value in each neighbour that has a common face with cell 0. Equation (3.8) may be written as:

$$\Delta_f = \phi_{f,0} - \phi_0 = (\mathbf{x}_f - \mathbf{x}_0) \cdot (\nabla\phi)_{r,0} \quad (3.27)$$

A new scalar factor is introduced for each face, defined as:

$$r_f = \begin{cases} \frac{\Delta_f}{\Delta_{max}} & \Delta_f > 0 \\ \frac{\Delta_f}{\Delta_{min}} & \Delta_f \leq 0 \end{cases} \quad (3.28)$$

In the current study, the Venkatakrishnan limiter (Venkatakrishnan, 1994) is used in the simulation. The Venkatakrishnan limiter is given for each face as:

$$\alpha_{f-lim.} = \frac{2r_f + 1}{r_f(2r_f + 1) + 1}. \quad (3.29)$$

Finally, only one value is used as the cell value, which is given by

$$\alpha_{lim.} = \min(\alpha_{f-lim.}). \quad (3.30)$$

### 3.5 Cell Gradients

Cell gradients are computed using the reconstruction gradients. For the Green-Gauss gradient method, the improved estimates of the face values, obtained from the reconstruction gradients, can in turn be used to obtain better estimates of the cell gradients using Gauss' divergence theorem:

$$\nabla\phi = \frac{1}{V_0} \sum_f \phi_f \mathbf{A}_f \quad (3.31)$$

where the face value is approximated by the arithmetic average of the face values reconstructed from the adjacent cell values:

$$\phi_f = \frac{\phi_{f,0} + \phi_{f,m}}{2}. \quad (3.32)$$

Finally, the scalars  $\phi_{f,0}$  and  $\phi_{f,m}$  are calculated from equations (3.8) and (3.9).

### 3.6 Iterative Methodology

The discretization approach will result in a large system of linear algebraic equations, which needs to be solved implicitly in an iterative fashion. The algebraic system for the transported variable  $\phi$  at iteration  $k+1$  is written implicitly as:

$$a_p \phi_p^{k+1} + \sum_n a_n \phi_n^{k+1} = b \quad (3.33)$$

where the summation is carried out over all the neighbours  $n$  of cell  $p$ . The explicit parameter  $b$  in the right hand side of equation (3.33) is evaluated from the previous iteration level  $k$ . The coefficients  $a_p$  and  $a_n$  are obtained directly from the discretized terms. An under-relaxation factor may be introduced implicitly in equation (3.33) as follows:

$$\frac{a_p}{\omega_{u.relax}} \phi_p^{k+1} + \sum_n a_n \phi_n^{k+1} = b + \frac{a_p}{\omega_{u.relax}} (1 - \omega_{u.relax}) \phi_p^k \quad (3.33)$$

where  $\omega_{u.relax}$  is the under-relaxation factor, the superscript  $k+1$  implies the value after the solution is produced, and the source term on the right hand side is evaluated at the previous iteration. Defining  $\Delta\phi = \phi^{k+1} - \phi^k$ , equation (3.33) can be written in delta form as:

$$\frac{a_p}{\omega_{u.relax}} \Delta\phi_p + \sum_n a_n \Delta\phi_n = b - a_p \phi_p^k - \sum_n a_n \phi_n^k. \quad (3.34)$$

The right hand side in equation (3.34) is termed the residual, and it represents the discretized form of the original equation (3.4) at iteration  $k$ . Therefore, the residual will be zero when the discretized equation is satisfied exactly.

For linear phenomena such as constant-property solid conduction, the linear system needs to be constructed and solved only once. In most situations, however, the system is non-linear. For example, the source term  $S_\phi$  or diffusion coefficient  $\Gamma_\phi$  could themselves be functions of  $\phi$ . In this case, an iterative solution is required, and there are two levels of iteration; an outer iteration loop controlling the solution update and an inner loop governing the iterative solution of the linearized system. Since the outer iterations are



repeated multiple times, the linear system only needs to be solved approximately at each iteration. The iterative solution of linear equations is covered below.

The discretization approach described above leads to a linear system which can be expressed as:

$$\mathbf{Aa} = \mathbf{b}. \quad (3.35)$$

Equation (3.35) represents the algebraic equations assembled for each computational cell. The matrix  $\mathbf{A}$  contains the coefficients of the linear system, i.e., coefficients  $a_p$  and  $a_n$  on the left hand side of equation (3.34), the vector  $\mathbf{a}$  represents the unknowns  $\Delta\phi$  in equation (3.34), and the vector  $\mathbf{b}$  represents the residuals on the right hand side of equation (3.34). Typically, the matrix  $\mathbf{A}$  is very sparse; therefore, direct methods such as Gauss elimination or LU decomposition on such systems are very costly. In STAR-CCM+, an efficient iterative method, i.e., the algebraic multigrid method (AMG), is used to solve the discrete linear system iteratively.

### 3.6.1 Basic Iterative Methods

The general principle behind iterative methods is that, given an approximate solution,  $\mathbf{a}^k$ , to find a better approximation  $\mathbf{a}^{k+1}$ , the process is repeated until convergence. If the exact solution vector in equation (3.35) is  $\mathbf{a}_{ex.}$ , the error vector ( $\mathbf{er}$ ) and residual vector ( $\mathbf{r}$ ) at iteration  $k$  are given as:

$$\mathbf{er}^k = \mathbf{a}_{ex.} - \mathbf{a}^k \quad (3.36)$$

$$\mathbf{r}^k = \mathbf{b} - \mathbf{Aa}^k, \quad (3.37)$$

from which it follows that

$$\mathbf{Aer}^k = \mathbf{r}^k. \quad (3.38)$$

Therefore, continuing the iteration until the residual is driven to a small value will also cause the error to be driven to a small value.

The most basic iterative methods are Jacobi and Gauss-Seidel iterations. These methods involve visiting each cell in sequence, and updating the value of  $a_i$  in each cell  $i$  using the coefficients of its  $n$  neighbour cells. The difference between Jacobi and Gauss-Seidel iteration appears to be slight: Jacobi uses the “old” values of  $a_n$ , while Gauss-Seidel uses the available values that have been updated, but nevertheless results in convergence that is about twice as fast as the Jacobi method (Hoffmann & Chiang, 2000).

### **3.6.2 Multigrid Methods**

The primitive iteration methods described above, while relatively simple to implement, exhibit relatively slow convergence characteristics. This suggests that some of the work could be done on a coarse grid, since computations on coarse grids are much less costly and, for example, the Gauss-Seidel method converges four times faster on a grid half as fine (STAR-CCM+ Manual, 2012). The main idea of multigrid is to accelerate the convergence of a basic iterative method by global correction from time to time, accomplished by solving a coarse problem. This principle is similar to interpolation between coarser and finer grids. Multigrid algorithms perform the following steps:

- Agglomerate cells to form coarse grid levels.
- Transfer the residual from a fine level to a coarser level (known as restriction).
- Transfer the correction from a coarse level back to a finer level (known as prolongation).

More information regarding multigrid algorithms can be found in Astrachancev (1971), Press et al. (2007), Bakhvalov (1966) and Fedorenko (1964).

### **3.7 Segregated Models**

In the segregated approach, the governing equations are solved sequentially, i.e., segregated from one another. Because the governing equations are generally non-linear and coupled, the solution loop must be carried out iteratively in order to obtain a converged numerical solution. The individual governing equations for the solution variables, e.g.,  $u, v, w, p, T$ , are solved one after another. Each governing equation, while being solved, is decoupled or segregated from all other equations. The segregated algorithm is memory efficient, since the discretized equations need only be stored in the memory one at a time. However, the solution convergence is relatively slow since the equations are solved in a decoupled manner. In our study, three segregated models are used in the simulations, i.e., segregated flow model, segregated fluid energy model, and segregated volume of fluid model.

#### **3.7.1 Segregated Flow Model**

The term “segregated” refers to the fact that the solution algorithm uses a SIMPLE-type approach, which has separate pressure and velocity solvers. The segregated flow model solves the flow equations, i.e., one for each component of velocity, and one for pressure, in a segregated, or uncoupled manner. The linkage between the momentum and continuity equations is achieved with a predictor-corrector approach. The complete formulation can be described as using a collocated variable arrangement and Rhie

&Chow-type pressure-velocity coupling (Rhie & Chow, 1983; Ferziger & Peric, 2002) combined with a SIMPLE-type algorithm.

The continuity and Navier-Stokes equations can be represented by the following integral equations, obtained by choosing the appropriate physical variable for  $\phi$  in equation (3.3) (STAR-CCM+ Manual, 2012):

$$\frac{d}{dt} \int_{CV} \rho dV + \oint_A \mathbf{n} \cdot (\rho \mathbf{u}) dA = \int_{CV} S_u dV \quad (3.39)$$

$$\begin{aligned} \frac{d}{dt} \int_{CV} \rho \mathbf{u} dV + \oint_A (\rho \mathbf{u} \otimes \mathbf{u}) \cdot \mathbf{n} dA \\ = - \oint_A p \mathbf{I} \cdot \mathbf{n} dA + \oint_A \mathbf{T} \cdot \mathbf{n} dA + \int_{CV} (\mathbf{f}_r + \mathbf{f}_g + \mathbf{f}_p + \mathbf{f}_\omega + \mathbf{f}_u) dV \end{aligned} \quad (3.40)$$

where  $S_u$  in equation (3.39) contributes additional mass source terms, which may be specified by the user. The terms on the left hand side of equation (3.40) are the transient term and the convective flux. On the right hand side are the pressure gradient term, the viscous flux and the body force terms.  $\mathbf{I}$  is the identity matrix and  $\mathbf{T}$  is the viscous stress tensor. The body force terms represent the effects of system rotation, gravity, porous media, vorticity confinement and user-defined body forces, respectively. From this point on, all turbulence quantities in equations (3.39) and (3.40) will be expressed in terms of mean flow quantities. The time-averaged Navier-Stokes equations (see also section 3.8) are used for this purpose (Versteeg & Malalasekera, 2007; Hoffmann & Chiang, 2000).

In turbulent flow, the complete stress tensor is given by:

$$\mathbf{T} = \mathbf{T}_l + \mathbf{T}_t \quad (3.41)$$

where  $\mathbf{T}_l$  and  $\mathbf{T}_t$  are the laminar and turbulent stress tensors. The turbulent stress tensor is also known as the Reynolds stress tensor. The Boussinesq approximation is used to evaluate the Reynolds stress tensor as follow:

$$\mathbf{T} = \mu_{eff} \left[ \nabla \mathbf{U} + \nabla \mathbf{U}^T - \frac{2}{3} (\nabla \cdot \mathbf{U}) \mathbf{I} \right] \quad (3.42)$$

where  $\mathbf{U}$  is the mean velocity vector and  $\mu_{eff} = \mu + \mu_t$  is the effective viscosity (the sum of the laminar and turbulent viscosities).

Applying equation (3.40) to a cell-centred control volume for cell 0 and ignoring the body forces, one obtains the following discrete equation for the transport of velocity:

$$\frac{d}{dt} (\rho \mathbf{U} V)_0 + \sum_f (\mathbf{U} \rho \mathbf{U} \cdot \mathbf{n} A)_f = - \sum_f (p \mathbf{I} \cdot \mathbf{n} A)_f + \sum_f (\mathbf{T} \cdot \mathbf{n} A)_f \quad (3.43)$$

The discrete equation for each velocity component is expressed implicitly as a linear system as described in section (3.2) through section (3.5). The transient terms, body forces and convective flux for each velocity component is discretized in the same manner as the scalar quantity described therein. To evaluate the stress tensor  $\mathbf{T}$ , the velocity gradient tensor  $\nabla \mathbf{U}_f$  at the face must be written in terms of the cell velocities for purposes of linearization. Using equation (3.13) through (3.15), the velocity gradient tensor at a face may be written:

$$\nabla \mathbf{U}_f = (\mathbf{U}_1 - \mathbf{U}_0) \otimes \boldsymbol{\alpha}_m + \overline{\nabla \mathbf{U}_f} - (\overline{\nabla \mathbf{U}_f}) \otimes \boldsymbol{\alpha}_m \quad (3.44)$$

For no-slip walls in turbulent flow, it is assumed that only the component of velocity parallel to the wall,  $u_{parallel}$ , is of interest. A linear relationship between the wall shear force and the wall-parallel component velocity is hypothesized as:

$$(\mathbf{T} \cdot \mathbf{n} A)_f = -\gamma_{ts} \mathbf{U}^t \quad (3.45)$$

where  $\gamma_{ts}$  is a coefficient used in the turbulent stress calculation, defined as:

$$\gamma_{ts} = |\mathbf{nA}| \frac{\rho u_\tau}{u^+} \quad (3.46)$$

where  $u_\tau$  and  $u^+$  are shear velocity and normalized wall-parallel velocity, respectively.

These velocities are defined as:

$$u_\tau = \sqrt{\tau_w / \rho} \quad (3.47)$$

$$u^+ = \frac{u_{parallel}}{u_\tau}. \quad (3.48)$$

The shear velocity  $u_\tau$  is computed according to the specific turbulence model. The value of  $u^+$  is obtained (as a function of  $y^+$ ) from the appropriate wall law (see next subsection for details of non-dimensional quantities).

In order to compute the pressure gradient term in equation (3.43), the pressure is evaluated at each face according to a weighted average:

$$p_f = \frac{\bar{a}_0 p_{f0} + \bar{a}_1 p_{f1}}{\bar{a}_0 + \bar{a}_1} \quad (3.49)$$

where  $\bar{a}_0$  and  $\bar{a}_1$  are the average of the momentum coefficients for all components of momentum for cells 0 and 1, respectively.  $p_{f0}$  and  $p_{f1}$  are interpolated from cell values and reconstruction gradients according to equations (3.8) and (3.9).

Assuming no source terms, the discrete continuity equation is written as:

$$\sum_f \dot{m}_f = \sum_f (\dot{m}_f^* + \dot{m}_f') = 0 \quad (3.50)$$

where symbols "\*" and "'" refer to predictor and correction values, respectively. The uncorrected face mass flow rate  $\dot{m}_f^*$  is computed after the discrete momentum equations have been solved. The mass flow rate correction  $\dot{m}_f'$  is required to ensure that the total mass is conserved. For interior faces, the uncorrected mass flow rate may be written in terms of the cell variables as follows (STAR-CCM+ Manual, 2012):

$$\dot{m}_f^* = \rho_f \left[ \mathbf{n}A \cdot \left( \frac{\mathbf{U}_0^* + \mathbf{U}_1^*}{2} \right) \right] - (Y_{RC})_f \quad (3.51)$$

where  $\mathbf{U}_0^*$  and  $\mathbf{U}_1^*$  are the cell velocities after the discrete momentum equations have been solved,  $(Y_{RC})_f$  is the Rhie & Chow-type dissipation at the face, given by:

$$(Y_{RC})_f = Q_f \left( p_1^* - p_0^* - \overline{\nabla p}_f^* \cdot (\mathbf{x}_1 - \mathbf{x}_0) \right) \quad (3.52)$$

with

$$Q_f = \rho_f \left( \frac{V_0 + V_1}{a_0 + a_1} \right) \boldsymbol{\alpha}_m \cdot \mathbf{n}A \quad (3.53)$$

where  $V_0$  and  $V_1$  are the volumes for cell 0 and cell 1,  $p_0^*$ ,  $p_1^*$  are the cell pressures from the previous iteration,  $\overline{\nabla p}_f^*$  is the volume-weighted average of the cell gradients of pressure,  $\nabla p_0^*$  and  $\nabla p_1^*$ , and the vector  $\boldsymbol{\alpha}_m$  is defined in equation (3.14). The pressure correction equation is set up after calculating the intermediate velocities and uncorrected mass flow rates from equation (3.51) at all faces (see Versteeg & Malalasekera, 2007 for more details).

In the cases where the boundary velocity is specified, such as wall and inlet boundaries, the value of  $\dot{m}_f^*$  is calculated directly from the known velocity  $\mathbf{U}_f^*$  on the boundaries as:

$$\dot{m}_f^* = \rho_f (\mathbf{n}A \cdot \mathbf{U}_f^*). \quad (3.54)$$

For these boundaries, a Neumann condition is used for the pressure correction:

$$p'_f = p'_0 \quad (3.55)$$

and the mass flux corrections are zero.

On a specified-pressure boundary (stagnation inlet, pressure outlet), the pressure corrections will not be zero. The uncorrected boundary mass flux is given by:

$$\dot{m}_f^* = \rho_f(\mathbf{n}A \cdot \mathbf{U}_f^*) - (Y_{RC})_f \quad (3.56)$$

with

$$(Y_{RC})_f = Q_f \left( p_f^* - p_0^* - \nabla p_0^* \cdot (\mathbf{x}_1 - \mathbf{x}_0) \right) \quad (3.57)$$

$$Q_f = \rho_f \left( \frac{V_0}{a_0} \right) \alpha_m \mathbf{n} dA. \quad (3.58)$$

Finally, the SIMPLE algorithm is used to control the overall solution. The acronym SIMPLE stands for ‘semi-implicit method for pressure-linked equations’. This algorithm may be summarized as follows (Versteeg & Malalasekera, 2007):

- Set up the boundary conditions.
- The reconstruction gradients of velocity and pressure are computed.
- The cell velocity and pressure gradient are computed.
- The discretized momentum equation is solved to create the intermediate velocity field ( $\mathbf{U}^*$ ).
- The uncorrected mass fluxes at faces ( $\dot{m}_f^*$ ) are computed.
- The pressure correction equation is solved to produce cell values of the pressure correction  $p'$ , where  $p' = p - p^*$ .
- The pressure field is updated using

$$p^{k+1} = p^k + \omega_{u.relax} p' \quad (3.59)$$

where  $\omega_{u.relax}$  is the under-relaxation factor for pressure.

- The boundary pressure is corrected.
- The face mass fluxes are corrected using

$$\dot{m}_f^{k+1} = \dot{m}_f^* + \dot{m}'_f. \quad (3.60)$$

- The cell velocities are corrected according to the relation



$$\mathbf{U}^{k+1} = \mathbf{U}^* - \frac{V\nabla p'}{\mathbf{a}_p^U} \quad (3.61)$$

where  $\nabla p'$  is the cell gradient of the pressure corrections,  $\mathbf{a}_p^U$  is the vector of central coefficients for the discretized linear system representing the velocity equation and  $V$  is the cell volume.

- All other discretized transport equations are solved to find the new value, i.e.,  $\phi^{k+1}$ .
- Set  $p^* = p$ ,  $\mathbf{U}^* = \mathbf{U}$ ,  $\phi^* = \phi$  and repeat the iteration until the solution converges.

### 3.7.2 Segregated Fluid Energy Model

There are three Segregated Fluid Energy models in STAR-CCM+; segregated fluid temperature, segregated fluid enthalpy and segregated fluid isothermal. The first two models solve the total energy equation in a continuum using a segregated formulation, while the third uses a constant setting for temperature. In our study, a segregated fluid temperature is used in the simulations.

The segregated fluid temperature model solves the total energy equation with temperature as the independent variable. Enthalpy is then computed from temperature according to the equation of state. The integral form of the energy equation can be written as (STAR-CCM+ Manual, 2012):

$$\begin{aligned} \frac{d}{dt} \int_{CV} \rho E dV + \oint_A (\rho H_e \mathbf{U}) \cdot \mathbf{n} dA \\ = - \oint_A \mathbf{q}'' \cdot \mathbf{n} dA + \oint_A (\mathbf{T} \cdot \mathbf{U}) \cdot \mathbf{n} dA + \int_{CV} \mathbf{f} \cdot \mathbf{U} dV + \int_{CV} S_u dV \end{aligned} \quad (3.62)$$

where  $E$  is the total energy, defined as the sum of internal energy,  $i$ , kinetic energy,  $KE$ , and gravitational potential energy,  $PE$ .  $H_e$  is the total enthalpy,  $\mathbf{q}''$  is the heat flux vector,  $\mathbf{T}$  is the viscous stress tensor,  $\mathbf{U}$  is the mean velocity vector,  $\mathbf{f}$  is the body force vector which represents all body forces on the right hand side of equation (3.40) and  $S_u$  contributes additional energy source terms, such as those specified by the user. The total energy is related to the total enthalpy  $H_e$  by (neglecting the  $PE$ ) :

$$E = H_e - p/\rho \quad (3.63)$$

$$H_e = h_e + |\mathbf{U}|^2/2 \quad (3.64)$$

$$h_e = c_p T . \quad (3.65)$$

The discrete form of equation (3.62) at a cell-centred control volume (volume  $V_0$ ) is:

$$\frac{d}{dt}(\rho E V_0) + \sum_f [(\rho H_e \mathbf{U} + \mathbf{q}'' - \mathbf{T} \cdot \mathbf{U}) \cdot \mathbf{n} A]_f = (\mathbf{f} \cdot \mathbf{U} + S_u) V_0 . \quad (3.66)$$

The unsteady term  $\frac{d}{dt}(\rho E V_0)$  in equation (3.66) is evaluated as described in subsection 3.2.1, the convective term  $\sum_f (\rho H_e \mathbf{U} \cdot \mathbf{n} dA)_f$  is evaluated as described in subsection 3.2.2, and the convective quantity here is the total enthalpy, i.e.,  $\phi = H_e$ . The viscous work term  $\sum_f [(\mathbf{T} \cdot \mathbf{U}) \cdot \mathbf{n} dA]_f$ , is evaluated in a straightforward fashion as illustrated in subsection 3.7.1.

The heat flux vector in the diffusion term  $\sum_f (\mathbf{q}'' \cdot \mathbf{n} dA)_f$  in equation (3.66) is given by:

$$\mathbf{q}'' = -k_{eff} \nabla T \quad (3.67)$$

where  $k_{eff}$  is the effective thermal conductivity given by:

$$k_{eff} = k + \frac{\mu_t c_p}{Pr_t} \quad (3.68)$$

where  $Pr_t$  is the turbulent Prandtl number. The diffusion term is evaluated as described in section 3.2.3 as follows:

$$\begin{aligned} D_f &= \mathbf{q}'' \cdot \mathbf{n}A = -[k_{eff} \nabla T \cdot \mathbf{A}]_f \\ &= -k_{eff} [(T_1 - T_0) \boldsymbol{\alpha}_m \cdot \mathbf{A} + \overline{\nabla T} \cdot \mathbf{A} - (\overline{\nabla T} \cdot \mathbf{ds}) \boldsymbol{\alpha}_m \mathbf{A}] \end{aligned} \quad (3.69)$$

where the definitions of  $\boldsymbol{\alpha}_m$  and  $\overline{\nabla T}$  are given in equations (3.14) and (3.15), respectively.

For boundary faces, the heat flux is zero for inviscid flows. For viscous flows, the heat flux (or heat crossing the boundary) is required. This is specified directly in the case of adiabatic or specified heat flux walls. It can also be inferred as a convective heat transfer condition, such that

$$\mathbf{q}'' \cdot \mathbf{n}A = h(T_{ref} - T_w)A_w \quad (3.70)$$

where  $h$  is a convective heat transfer coefficient,  $T_{ref}$  (or  $T_f$ ) is a reference (or fluid) temperature and  $A_w$  is the control volume face area at the fluid-wall interface. For turbulent flow in which the wall temperature is specified, thermal wall laws are employed as follows:

$$\mathbf{q}'' \cdot \mathbf{n}A = \frac{|\mathbf{n}A| \rho c_p u_\tau}{T^+} (T_{p0} - T_w) \quad (3.71)$$

where  $T_w$  is the local wall temperature and  $T^+$  is defined in terms of the appropriate thermal wall law.

A wall law is a mathematical description of mean flow quantities, such as velocity, temperature and species concentration, in turbulent boundary layers. Numerous experiments have shown that the near-wall region can be largely subdivided into three layers. In the innermost layer, called the viscous sub-layer, the flow is almost laminar, and the (molecular) viscosity plays a dominant role in momentum and heat or mass

transfer. In the outer layer, called the fully turbulent or logarithmic layer, turbulence plays a major role. Finally, there is a buffer region between the viscous sub-layer and the fully turbulent layer where the effects of molecular viscosity and turbulence are equally important. The following non-dimensional quantities are used with the law of the wall for mean velocity:

$$y^+ = \frac{y_{p0} u_\tau}{\nu} \quad (3.72)$$

$$u^+ = \frac{u_{parallel}}{u_\tau} \quad (3.73)$$

$$T^+ = \frac{\rho c_p u_\tau}{q_w''} (T_{p0} - T_w). \quad (3.74)$$

In the above equations,  $y_{p0}$  is the normal distance from the wall to the wall-cell centroid,  $\nu$  is the kinematic viscosity,  $u_{parallel}$  is the component of wall-cell velocity parallel to the wall,  $q_w'' (= \mathbf{q}'' \cdot \mathbf{n})$  is the wall heat flux. The wall laws are set up to provide  $u^+$  and  $T^+$  as a function of  $y^+$  and other relevant quantities, such as molecular and turbulent Prandtl numbers.

The wall laws differ only in their treatment in the buffer region; the viscous sub-layer and log-layer behaviours are identical. For the viscous sub-layer ( $y^+ < 5$ ), the velocity distribution is modeled as:

$$u_{lam}^+ = y^+. \quad (3.75)$$

The temperature distribution in the viscous sub-layer is modeled as:

$$T_{lam}^+ = Pr (u_{lam}^+ - q_{lam}^+) \quad (3.76)$$

where  $q_{lam}^+$  is the effect of viscous dissipation, given as

$$q_{lam}^+ = \frac{\rho u_\tau u_{parallel}^2}{2q_w''}. \quad (3.77)$$

The logarithmic law for mean velocity is known to be valid for  $30 < y^+ < 300$ . In the logarithmic layer, the velocity distribution is modeled as:

$$u_{trb}^+ = \frac{1}{\kappa} \ln(E' y^+) \quad (3.78)$$

with

$$E' = \frac{E_w}{f_r} \quad (3.79)$$

where the default values of the coefficients are  $\kappa = 0.42$  and  $E_w = 9.0$ .  $f_r$  in equation (3.79) is the roughness function, its value is unity for a smooth wall, as in our study. The temperature distribution is modeled as:

$$T_{trb}^+ = Pr_t (u_{trb}^+ + P + q_{trb}^+) \quad (3.80)$$

where  $P$  is a function of Prandtl number defined by Jayatilleke (1969) as:

$$P = 9.24 \left[ \left( \frac{Pr}{Pr_t} \right)^{3/4} - 1 \right] \left[ 1 + 0.28 \exp \left( \frac{-0.007 Pr}{Pr_t} \right) \right] \quad (3.81)$$

and the effect of viscous dissipation is modeled as:

$$q_{trb}^+ = \frac{\rho u_\tau}{2q_w''} \left[ u_{parallel}^2 - \left( \frac{Pr}{Pr_t} - 1 \right) (u_c^+ u_\tau)^2 \right]. \quad (3.82)$$

The quantity  $u_c^+$  is a fictitious non-dimensional velocity that would occur at the intersection of the laminar and turbulent temperature profiles. It is computed from equation (3.81) as:

$$u_c^+ = \frac{P}{Pr - Pr_t} \quad (3.83)$$

where  $Pr$  is the molecular Prandtl number and  $Pr_t$  is the turbulent Prandtl number.

The standard wall laws have slope discontinuities between the laminar and logarithmic regions. They are given by:

$$u^+ = \begin{cases} u_{lam}^+ & \text{for } y^+ \leq y_m^+ \\ u_{trb}^+ & \text{for } y^+ > y_m^+ \end{cases} \quad (3.84)$$

and

$$T^+ = \begin{cases} T_{lam}^+ & \text{for } y^+ \leq y_l^+ \\ T_{trb}^+ & \text{for } y^+ > y_l^+ \end{cases} \quad (3.85)$$

The procedure of applying the law-of-the-wall for temperature is as follows. Once the physical properties of the fluid being modeled are specified, its molecular Prandtl number is computed. Then, given the molecular Prandtl number, the thermal sub-layer thickness,  $y_l^+$ , is computed from the intersection of the linear and logarithmic profiles, and stored. A similar process is used to find  $y_m^+$ . During the iteration, depending on the  $y^+$  value at the near-wall cell, either the linear or the logarithmic profile in equations (3.84) and (3.85) is applied to compute the velocity, wall temperature or heat flux (depending on the type of the thermal boundary condition).

Blended wall laws may also be used to describe the quantities at near-wall locations. The blended wall laws are intended to represent the buffer layer by appropriately blending the viscous sub-layer and logarithmic regions. For momentum, Reichardt's law (Reichardt, 1951) is used:

$$u^+ = \frac{1}{\kappa} \ln(1 + \kappa y^+) + C_b \left[ 1 - \exp\left(-\frac{y^+}{D_b}\right) - \frac{y^+}{D_b} \exp(-B_b y^+) \right] \quad (3.86)$$

where

$$D_b = y_m^+ \quad (3.87)$$

$$C_b = \frac{1}{\kappa} \ln\left(\frac{E'}{\kappa}\right) \quad (3.88)$$

$$B_b = \frac{1}{2} \left( \frac{D_b \kappa}{C_b} + \frac{1}{D_b} \right). \quad (3.89)$$

For temperature, Kader's law (Kader, 1981) is used to calculate the non-dimensional temperature as follow:

$$T^+ = \exp(-\Gamma) (T_{lam}^+ - q_{lam}^+) + \exp\left(-\frac{1}{\Gamma}\right) (T_{trb}^+ - q_{trb}^+) \quad (3.90)$$

where  $\Gamma$  is a blending function, for a smooth wall this function is given as:

$$\Gamma = \frac{0.01(Pr y^+)^4}{1 + 5Pr^3 y^+}. \quad (3.91)$$

Finally, equation (3.70) may be rewritten for the wall cells as:

$$\mathbf{q}'' \cdot \mathbf{n} = q_w'' = h(T_{p0} - T_w). \quad (3.92)$$

Comparing equations (3.74) and (3.92), the local heat transfer coefficient can be written as:

$$h(y_{p0}) = h_{local} = \frac{\rho(y_{p0})c_p(y_{p0})u_\tau}{T^+(y^+(y_{p0}))}. \quad (3.93)$$

All physical properties stated in equation (3.93) are for fluid. The independent variables, i.e., density, specific heat and non-dimensional temperature are function of the distance  $y_{p1}$ . Equation (3.93) also can be written in terms of temperature as:

$$T_{local} = T_{p0} = T_w + \frac{q_w''}{h_{local}}. \quad (3.94)$$

### 3.7.3 Segregated Volume of Fluid Model

The flow field in this study involves two different immiscible fluids, requiring a numerical model that can handle two-phase flow. Volume of fluid (VOF) (Hirt and Nicholls, 1981) is a simplified and efficient method that provides an approach to capture

the movement of the interface between the mixture phases. In VOF, the various fluids are assumed to share a common velocity, pressure and temperature field. The solutions are obtained by solving the same set of basic governing equations as in a single phase flow (see subsections 3.7.1 and 3.7.2) for an equivalent fluid whose physical properties are calculated as functions of the physical properties of its constituent phases and their volume fractions. Therefore, the equivalent fluid properties in each control volume can be calculated as:

$$\rho = \sum_i \rho_i \alpha_i \quad (3.95)$$

$$\mu = \sum_i \mu_i \alpha_i \quad (3.96)$$

$$c_P = \sum_i (c_P)_i \rho_i \alpha_i / \sum_i \rho_i \alpha_i \quad (3.97)$$

where  $\rho_i$ ,  $\mu_i$ ,  $(c_P)_i$  and  $\alpha_i$  are the density, molecular viscosity, specific heat and volume fraction of the  $i^{\text{th}}$  phase. The volume fraction  $\alpha_i$  of the  $i^{\text{th}}$  phase in the control volume is defined as:

$$\alpha_i = \frac{V_i}{V}. \quad (3.98)$$

The segregated VOF solver controls the solution update for the phase volume fractions. More specifically, it solves the discretized volume fraction conservation equation for each phase present in the flow. The transport of volume fractions  $\alpha_i$  is described by using equation (3.2) with  $\phi = \alpha_i$  and  $\Gamma_\phi = 0$ :

$$\frac{\partial}{\partial t} \int_{CV} \rho_i \alpha_i dV + \int_{CV} \nabla \cdot (\rho_i \alpha_i \mathbf{U}) dV = \int_{CV} S_{\alpha_i} dV \quad (3.99)$$

which can be expanded as



$$\int_{CV} \rho_i \left[ \frac{\partial \alpha_i}{\partial t} + \mathbf{U} \cdot \nabla \alpha_i \right] dV + \int_{CV} \alpha_i \left[ \frac{\partial \rho_i}{\partial t} + \nabla \cdot \rho_i \mathbf{U} \right] dV = \int_{CV} S_{\alpha_i} dV \quad (3.100)$$

where  $S_{\alpha_i}$  is the source or sink of the  $i^{\text{th}}$  phase in the control volume. One can see that in the case when phases have constant densities and have no sources, the continuity equation reduces to  $\nabla \cdot \mathbf{U} = 0$  and equation (3.100) reduces to:

$$\int_{CV} \frac{\partial \alpha_i}{\partial t} dV + \int_{CV} \mathbf{U} \cdot \nabla \alpha_i dV = 0. \quad (3.101)$$

The discretization of the transient term  $\int_{CV} \frac{\partial \alpha_i}{\partial t} dV$  in equation (3.101) is straightforward as illustrated in subsection 3.2.1. However, for the convective term, the conventional schemes, i.e., upwind, linear upwind and central differencing, fail to approximate large spatial variations of phase volume fraction, which are usually represented by the Heaviside unit step function. Therefore, the main task in VOF is to discretize the convective term  $\int_{CV} \mathbf{U} \cdot \nabla \alpha_i dV$  in equation (3.101) in a way that prevents artificial smearing of the step interface profile due to numerical diffusion.

Over the years, a number of advection schemes have been developed that can be generally classified as either interface tracking methods or interface capturing methods. Interface tracking methods are based on the concept of geometric interface reconstruction, and usually give a good approximation for the interface and allow for proper calculation of the fluxes through the faces of control volumes. However, their application is often restricted to structured grids. Furthermore, the computational effort is increased since estimation of the spatial orientation of the interface from the distribution of the volume fraction needs an extensive number of numerical operations (Zaleski, 2002). Interface capturing methods are more efficient and commonly used to compute

multiphase flows. Unlike geometric interface reconstruction methods, interface capturing methods do not introduce a geometrical representation of the interface but try to satisfy the boundedness criterion by a properly chosen discretization scheme. Generally, in interface capturing methods, a compressive scheme is used for discretization. However, this has been found to create an interface stepping whenever the flow is not aligned with the computational grid. High-resolution schemes are an alternative option used to resolve this issue. The normalized variable diagram (NVD) provides the methodology used in constructing high-resolution schemes (Leonard, 1991). The Compressive Interface Capturing Scheme for Arbitrary Meshes (CICSAM) (Ubbink and Issa, 1999) and the High-Resolution Interface Capturing scheme (HRIC) (Muzaferija et al., 1998) are the most commonly used high-resolution schemes for interface capturing with the VOF model. Waclawczyk and Koronowicz (2008) give a detailed comparison of the performance of the CICSAM and HRIC schemes. The HRIC scheme is used to capture the interface in the present work.

The normalized variable diagram (NVD) is very useful for analyzing boundedness properties of convective discretization schemes. Figure 3.1 below shows three cells in the vicinity of a cell face  $f$ , across which the velocity is known. The nodal variable values are labeled  $\alpha_D$ ,  $\alpha_C$  and  $\alpha_U$ , representing the downwind, central, and upwind positions relative to each other.

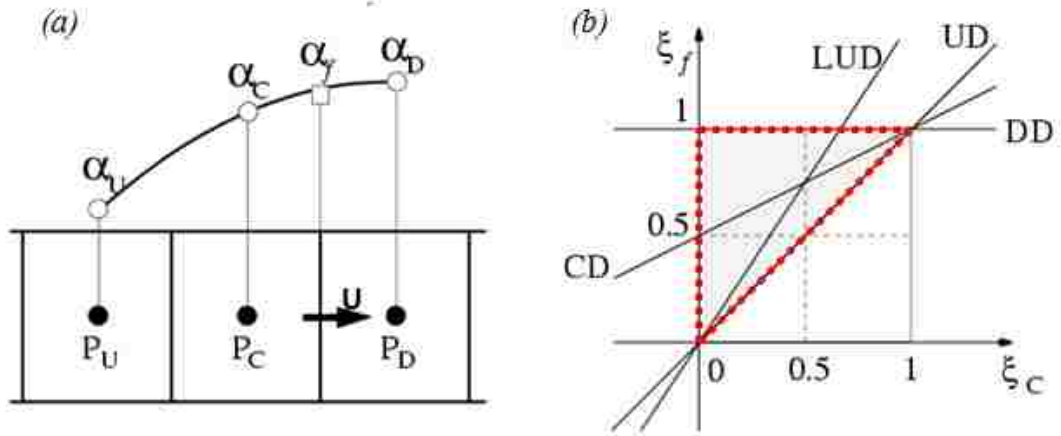


Figure 3.1: (a) Convective boundedness criterion (CBC) on the three control volumes; upwind (U), central (C) and downwind (D), (b) Normalized variable diagram (NVD); upwind differencing (UD), downwind differencing (DD), central differencing (CD) and linear upwind differencing (LUD)

We can introduce a normalized variable  $\xi_{(x,t)}$ , which can be calculated at any point, by

$$\xi_{(x,t)} = \frac{\alpha_{(x,t)} - \alpha_U^n}{\alpha_D^n - \alpha_U^n}. \quad (3.102)$$

Now, in a case when  $\xi_f$  is a function of  $\alpha_D$ ,  $\alpha_C$ , and  $\alpha_U$ , the normalized face value is a function only of its adjacent upstream node value and the normalized values of node U and D are constant, so that:

$$\xi_f^n = f(\xi_C^n) \quad (3.103)$$

$$\xi_U^n = 0 \text{ and } \xi_D^n = 1. \quad (3.104)$$

For first-order upwind scheme, equation (3.103) becomes:

$$\xi_f^n = \xi_C^n. \quad (3.105)$$

For first-order downwind scheme, equation (3.103) becomes:

$$\xi_f^n = 1. \quad (3.106)$$

For central differencing scheme, equation (3.103) becomes:

$$\xi_f^n = \frac{\frac{\alpha_D^n + \alpha_C^n}{2} - \alpha_U^n}{\alpha_D^n - \alpha_U^n} = \frac{\frac{\alpha_D^n - \alpha_U^n}{2} + \frac{\alpha_C^n - \alpha_U^n}{2}}{\alpha_D^n - \alpha_U^n} = \frac{1}{2}(1 + \xi_C^n). \quad (3.107)$$

For the Lax-Wendroff method (Hoffmann & Chiang, 2000), equation (3.103) becomes:

$$\xi_f^n = \frac{1}{2}(1 + \xi_C^n) \quad (3.108)$$

which gives a similar result as central differencing.

For the second-order upwind scheme, equation (3.103) becomes:

$$\xi_f^n = \frac{3}{2}\xi_C^n. \quad (3.109)$$

Finally, for Fromm's method (Anderson, 1995)

$$\xi_f^n = \frac{1}{4} + \xi_C^n. \quad (3.110)$$

The normalized variable diagram for some of the linear convective schemes, plotted as a functional relationship in the form of equation (3.103), is illustrated in Figure 3.1b. Note that all the spatially second-order methods pass through the point (0.5, .75) which lies in the bounded region.

In order to avoid non-physical oscillations in the solution  $\xi_C^n$  has to be locally bounded between  $0 \leq \xi_C^n \leq 1$ . Consequently, monotonic behaviour imposes a necessary condition on  $\xi_f^n$ :

$$\xi_C^n \leq \xi_f^n \leq 1. \quad (3.111)$$

If  $\xi_u^n$  represents the face value of the adjacent upstream control volume (C) (not shown in Figure 3.1), then:

$$0 \leq \xi_u^n \leq \xi_C^n. \quad (3.112)$$

Now, the discrete form of equation (3.101) may be written in normalized form for control volume (C) as:

$$\xi_C^{n+1} = \xi_C^n - C(\xi_f^n - \xi_C^n) \quad (3.113)$$

where  $C$  is a local Courant number. In order to maintain monotonicity, the new  $\xi_C^{n+1}$  value must be constrained by:

$$\xi_U^{n+1} \leq \xi_C^{n+1} \leq \xi_D^{n+1}. \quad (3.114)$$

For pure advection at constant velocity, the right hand inequality is less restrictive than  $\xi_f^n \geq \xi_C^n$ , but the left hand inequality results in

$$\xi_f^n \leq \xi_U^n + \frac{1}{C}(\xi_C^n - \xi_U^{n+1}). \quad (3.115)$$

Since  $\xi_U^n$  is nonnegative and  $\xi_U^{n+1}$  (see equation (3.104)) is nonpositive (see equation (3.104)), the worst case condition is given by  $\xi_U^n = 0$ , i.e.,

$$\xi_f^n = \frac{\xi_C^n}{C} \quad \text{for } 0 \leq \xi_C^n \leq 1. \quad (3.116)$$

This is combined with equation (3.111) to give

$$\xi_C^n \leq \xi_f^n \leq 1 \quad \text{for } 0 \leq \xi_C^n \leq 1 \quad (3.117)$$

which constitutes the universal limiter in the monotonic range of  $\xi_C^n$ . Therefore, for  $\xi_C^n < 0$  or  $\xi_C^n > 1$ , a simple condition is imposed:

$$\xi_f^n = \xi_C^n \quad \text{for } \xi_C^n < 0 \text{ or } \xi_C^n > 1. \quad (3.118)$$

Equation (3.118) is equivalent to the first-order upwind scheme and is used by other non-linear schemes (second-order or higher). It does not erode the accuracy of the overall scheme, which is determined by behaviour in the smooth region, i.e.,  $\xi_C^n \rightarrow 0.5$ .

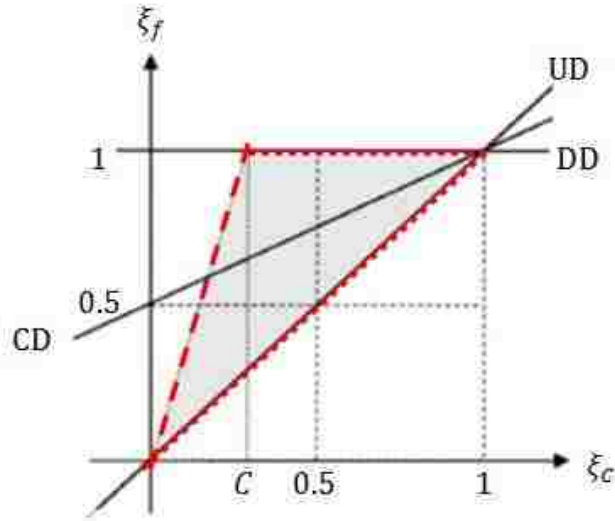


Figure 3.2: NVD shows the universal limiter boundaries. The dashed red boundary has a Courant number dependent slope  $1/C$ . The case shown is for  $C \approx 0.2$

The universal limiter is shown in Figure 3.2, the Courant number dependent boundary,  $\xi_f^n = \xi_c^n / C$  is shown as a dashed red line to emphasize the fact that its slope changes with different values of  $C$ . Therefore, an additional condition where the CBC is satisfied on the Courant number (Courant–Friedrichs–Lewy condition) is required. The Courant–Friedrichs–Lewy (CFL) condition is a necessary condition for stability while solving certain partial differential equations. The value  $C_{max}$  changes with the method that is used to solve the discretised equation, especially depending on whether the method is explicit or implicit. If an explicit (time marching) solver is used, then typically  $C_{max} = 1$ . Implicit solvers are usually less sensitive to numerical instability and so larger values of  $C_{max}$  may be tolerated. Note that for  $C \rightarrow 0$  in Figure 3.2, the red dashed boundary approaches the vertical axis, while for  $C = 1$ , it degenerates into  $\xi_f^n = \xi_c^n$  everywhere.

The face volume fraction of the  $i^{\text{th}}$  phase in equation (3.101) can be calculated as (Waclawczyk and Koronowicz, 2008):

$$\alpha_f = (1 - \beta_f)\alpha_c + \beta_f\alpha_D \quad (3.119)$$

where the blending function  $\beta_f$  is defined as:

$$\beta_f = \frac{\xi_f - \xi_c}{1 - \xi_c}. \quad (3.120)$$

However, to calculate  $\alpha_f$ , one needs to find  $\xi_f$  first. There are two main approaches in high resolution to find the normalized variable, i.e., the high-resolution interface capturing (HRIC) scheme (Muzaferija et al., 1998) and the compressive interface capturing scheme for arbitrary meshes (CICSAM) (Ubbink and Issa, 1999).

The high-resolution interface capturing (HRIC) scheme (Muzaferija et al., 1998) is used in our simulations. This scheme relies on the NVD and normalized variables. Application of the HRIC scheme can be divided into two main steps. Firstly, the normalized cell face value is estimated from a scheme that continuously connects the upwind and downwind schemes on the NVD diagram. The normalized face value  $\xi_f$  is calculated as:

$$\xi_f = \begin{cases} \xi_c & \xi_c < 0, \xi_c \geq 1 \\ 2\xi_c & 0 \leq \xi_c < 0.5 \\ 1 & 0.5 \leq \xi_c < 1 \end{cases} \quad (3.121)$$

Secondly, the calculated  $\xi_c$  value is further corrected according to the local Courant number:

$$C = \frac{\mathbf{U} \cdot \mathbf{n}A}{V} \Delta t \quad (3.122)$$

where  $V$  is the cell volume and  $A$  is the control volume face area. The correction is employed according to restriction that the amount of one fluid convected across a cell face during a time step should always be less than or equal to the amount available in the donor cell. This correction is made according to the following expressions (STAR-CCM+ Manual, 2012):

$$\xi_f^* = \begin{cases} \xi_f & C < C_l \\ \xi_c + (\xi_f - \xi_c) \frac{C_u - C}{C_u - C_l} C_l \leq & C < C_u \\ \xi_c & C_u \leq C \end{cases} \quad (3.123)$$

The default values of  $C_l$  and  $C_u$ , are 0.5 and 1, respectively. They are introduced to control blending of HRIC and upwind differencing schemes depending on the Courant number. For values of  $C < C_l$ , HRIC is used, for  $C_l \leq C < C_u$ , a blend of HRIC and upwind differencing is used, and for  $C_u \leq C$  pure UD is used.

The blending is introduced in order to bring stability and robustness to the scheme in the case when a large time variation of the free surface shape is present, and the time step is too large to resolve details of it. It is especially important if one uses the second-order discretization in time (STAR-CCM+ Manual, 2012). In this case, smaller values of  $C_l$  and  $C_u$  help to promote convergence. Smaller values will activate upwind differencing sooner, and the calculation will be more stable.



### 3.8 Turbulent Model

In order to include and account for the effect of turbulence in the flow field, the equations of fluid motion, i.e., equations (3.39) and (3.40) in section 3.7.1, are modified and amended by turbulence models. There are two approaches to reformulate the Navier-Stokes equations for this purpose. In both approaches, an averaging process is used. The resulting equations are known as the Reynolds-Averaged Navier-Stokes (RANS) equations (Versteeg & Malalasekera, 2007; Hoffmann & Chiang, 2000) and the Favre-Averaged Navier-Stokes (FANS) equations (Hoffmann & Chiang, 2000). In our simulation, the RANS model is used to reformulate the Navier-Stokes equations.

To obtain the Reynolds-Averaged Navier-Stokes (RANS) equations, the instantaneous quantities are decomposed into a mean value and a fluctuating component. As a result, additional terms, known as turbulent (or Reynolds) stresses, appear in the averaged equation due to the turbulence effect (see also section 3.7.1). The challenge is to model the Reynolds stresses in terms of the mean flow quantities, and hence provide closure to the system of governing equations. A turbulence model is a semi-empirical equation relating the fluctuating component to the mean flow variable with various constants provided from experimental investigations. When this equation is expressed as an algebraic equation, it is referred to as a zero-equation model. On the other hand, when partial differential equations are used, they are referred to as one-equation or two-equation models, depending on the number of equations in the model.

In our simulations, one of the important requirements of the computational model is, on one hand, to account for the interaction between the impinging jet and the wall to obtain good results for the heat transfer coefficient. On the other hand, consideration

must be given to the economic cost of the simulation and industrial applicability. The  $k-\omega$  SST turbulence model is a two-equation eddy viscosity model developed by Wilcox (1994, 1998) and Menter (1994). It has been shown to be more accurate in capturing wall effects than other two-equation models, where viscous flows are typically resolved and turbulence models are applied throughout the boundary layer. It has been selected as the turbulence model in our simulations. The  $k-\omega$  SST model solves additional transport equations for turbulent kinetic energy  $k$  and specific dissipation rate  $\omega$ , from which the turbulent kinematic viscosity,  $\nu_t = \mu_t/\rho = k/\omega$  can be derived. The simplest interpretation of  $\omega$  is that it represents the ratio of turbulence dissipation rate to the turbulence mixing energy.

The  $k-\omega$  SST equations look similar to the ones in the standard  $k-\omega$  model, but include an additional non-conservative cross-diffusion term ( $D_\omega$ ) containing the dot product  $\nabla k \cdot \nabla \omega$  (see equations (3.125) and (3.130)). The transport equations for the  $k-\omega$  SST model are (Hoffmann & Chiang, 2000; STAR-CCM+ Manual, 2012):

$$\begin{aligned} \frac{d}{dt} \int_{CV} \rho k dV + \int_A \rho k \mathbf{U} \cdot \mathbf{n} dA \\ = \int_A (\mu + \sigma_k \mu_t) \nabla k \cdot \mathbf{n} dA + \int_{CV} (G_k - \rho \beta^* f_{\beta^*} (\omega k - \omega_0 k_0) + S_k) dV \end{aligned} \quad (3.124)$$

$$\begin{aligned} \frac{d}{dt} \int_{CV} \rho \omega dV + \int_A \rho \omega \mathbf{U} \cdot \mathbf{n} dA \\ = \int_A (\mu + \sigma_\omega \mu_t) \nabla \omega \cdot \mathbf{n} dA + \int_{CV} (G_\omega - \rho \beta f_\beta (\omega^2 - \omega_0^2) + D_\omega + S_\omega) dV \end{aligned} \quad (3.125)$$

where  $S_k$  and  $S_\omega$  are the user-defined source terms,  $k_0$  and  $\omega_0$  are the ambient turbulence values (Spalart and Rumsey, 2007).  $G_k$  is the turbulent production, evaluated as:

$$G_k = \mu_t f_c S^2 - \frac{2}{3} \rho k \nabla \cdot \mathbf{U} - \frac{2}{3} \mu_t (\nabla \cdot \mathbf{U})^2 \quad (3.126)$$

where  $S$  is the modulus of the mean strain rate tensor:

$$S = |\mathbf{S}| = \sqrt{2\mathbf{S}:\mathbf{S}^T} = \sqrt{2\mathbf{S}:\mathbf{S}}. \quad (3.127)$$

The strain rate tensor is defined as:

$$\mathbf{S} = \frac{1}{2}(\nabla\mathbf{U} + \nabla\mathbf{U}^T) = \frac{1}{2} \begin{bmatrix} \left(2\frac{\partial U}{\partial x}\right) & \left(\frac{\partial U}{\partial y} + \frac{\partial V}{\partial x}\right) & \left(\frac{\partial U}{\partial z} + \frac{\partial W}{\partial x}\right) \\ \left(\frac{\partial V}{\partial x} + \frac{\partial U}{\partial y}\right) & \left(2\frac{\partial V}{\partial y}\right) & \left(\frac{\partial V}{\partial z} + \frac{\partial W}{\partial y}\right) \\ \left(\frac{\partial W}{\partial x} + \frac{\partial U}{\partial z}\right) & \left(\frac{\partial W}{\partial y} + \frac{\partial V}{\partial z}\right) & \left(2\frac{\partial W}{\partial z}\right) \end{bmatrix} \quad (3.128)$$

and the inner dot product ( $:$ ) of two tensors is a scalar, i.e.,  $\mathbf{A}:\mathbf{B} = C$ , where  $C = \sum_{i=1}^n \sum_{j=1}^n A_{i,j} B_{j,i}$ . The coefficient  $f_c$  is a curvature correction factor, usually associated with strong (streamline) curvature and frame-rotation. These effects can be incorporated by using a curvature correction factor, which alters the turbulent kinetic energy production term according to the local rotation and vorticity rates. More information about this correction factor is available in Arolla and Durbin, 2013. This coefficient is unity in the absence of the effect of curvature and rotation.

The production of  $\omega$  in equation (3.125) is evaluated as:

$$G_\omega = \gamma \rho \left[ \left( S^2 - \frac{2}{3} (\nabla \cdot \mathbf{U})^2 \right) - \frac{2}{3} \omega \nabla \cdot \mathbf{U} \right] \quad (3.129)$$

where  $\gamma$  is a blended coefficient of the model, defined by using equations (3.141) - (3.143). The term  $D_\omega$  is a cross-derivative term, defined as:

$$D_\omega = 2(1 - F_1) \rho \sigma_{\omega 2} \frac{1}{\omega} \nabla k \cdot \nabla \omega \quad (3.130)$$

with blending function  $F_1$ :

$$F_1 = \tanh \left[ \left\{ \min \left( \max \left( \frac{\sqrt{k}}{0.09\omega y}, \frac{500\nu}{y^2\omega} \right), \frac{2k}{y^2 CD_{k\omega}} \right) \right\}^4 \right] \quad (3.131)$$

where  $\sigma_{\omega 2}$  in equation (3.130) is a constant with  $\sigma_{\omega 2} = 0.856$ . In equation (3.131),  $\nu$  is kinematic viscosity,  $y$  is the distance to the nearest wall and  $CD_{k\omega}$  is a coefficient related to the cross-diffusion term, defined by:

$$CD_{k\omega} = \max \left( \frac{1}{\omega} \nabla k \cdot \nabla \omega, 10^{-20} \right). \quad (3.132)$$

The turbulent viscosity in equations (3.124) and (3.125) is computed as:

$$\mu_t = \rho k t' \quad (3.133)$$

where  $t'$  is a turbulent time scale computed as (Durbin, 1996):

$$t' = \min \left( \frac{\alpha^*}{\omega}, \frac{a_1}{S F_2} \right) \quad (3.134)$$

with function  $F_2$ :

$$F_2 = \tanh \left[ \left( \max \left( \frac{\sqrt{k}}{\beta^* \omega y}, \frac{500\nu}{y^2\omega} \right) \right)^2 \right] \quad (3.135)$$

where  $\alpha^* = 1$ ,  $a_1 = 0.31$ ,  $\beta^* = 0.09$ .

The function  $f_\beta$  in equation (3.125) is a "vortex-stretching modification" designed to overcome the round-jet/plane-jet anomaly. It is defined as (Wilcox, 1998):

$$f_\beta = \frac{1 + 70X_\omega}{1 + 80X_\omega} \quad (3.136)$$

where

$$X_\omega = \frac{(\mathbf{W} \cdot \mathbf{W}) : \mathbf{S}}{(\beta^* \omega)^3} \quad (3.137)$$

and  $\mathbf{W}$  is the rotation rate tensor which is given by:

$$\mathbf{W} = \frac{1}{2}(\nabla\mathbf{U} - \nabla\mathbf{U}^T) = \frac{1}{2} \begin{bmatrix} 0 & \left(\frac{\partial U}{\partial y} - \frac{\partial V}{\partial x}\right) & \left(\frac{\partial U}{\partial z} - \frac{\partial W}{\partial x}\right) \\ \left(\frac{\partial V}{\partial x} - \frac{\partial U}{\partial y}\right) & 0 & \left(\frac{\partial V}{\partial z} - \frac{\partial W}{\partial y}\right) \\ \left(\frac{\partial W}{\partial x} - \frac{\partial U}{\partial z}\right) & \left(\frac{\partial W}{\partial y} - \frac{\partial V}{\partial z}\right) & 0 \end{bmatrix} \quad (3.138)$$

If the vortex-stretching modification is not required,  $f_\beta$  is set to unity.

The function  $f_{\beta^*}$  is designed to improve the dependence of the model on free-stream boundary conditions. It is defined as follows:

$$f_{\beta^*} = \begin{cases} 1 & X_k \leq 0 \\ \frac{1 + 680X_k^2}{1 + 400X_k^2} & X_k > 0 \end{cases} \quad (3.139)$$

where

$$X_k = \frac{\nabla k \cdot \nabla \omega}{\omega^3}. \quad (3.140)$$

If the vortex-stretching modification is not required,  $f_{\beta^*}$  is set to unity.

The rest of the model coefficients, which appear in equations (3.124), (3.125) and (3.129), are calculated using the blending function  $F_1$ , such that each coefficient  $\varphi$  is given by:

$$\varphi = F_1\varphi_1 + (1 - F_1)\varphi_2 \quad (3.141)$$

The coefficients of sets 1 and 2 ( $\varphi_1$  and  $\varphi_2$ ) are:

$$\beta_1 = 0.0750, \sigma_{k1} = 0.85, \sigma_{\omega1} = 0.5, \kappa = 0.41, \gamma_1 = \frac{\beta_1}{\beta^*} - \sigma_{\omega1} \frac{\kappa^2}{\sqrt{\beta^*}} \quad (3.142)$$

$$\beta_2 = 0.0828, \sigma_{k2} = 1.0, \sigma_{\omega2} = 0.865, \kappa = 0.41, \gamma_2 = \frac{\beta_2}{\beta^*} - \sigma_{\omega2} \frac{\kappa^2}{\sqrt{\beta^*}} \quad (3.143)$$

with coefficients  $\alpha^* = 1, \beta^* = 0.09$ .

At near-wall locations, the following equations present the wall treatment formulations:

Wall-cell production:

$$G_k = \begin{cases} \frac{1}{\mu} \left( \rho u_\tau \frac{u_{parallel}}{u^+} \right)^2 \frac{\partial u^+}{\partial y^+} & high - y^+ (y^+ > 30) \\ \mu_t S^2 & low - y^+ (y^+ < 5) \\ g_b \mu_t S^2 + (1 - g_b) \frac{1}{\mu} \left( \rho u_\tau \frac{u_{parallel}}{u^+} \right)^2 \frac{\partial u^+}{\partial y^+} & all - y^+ \end{cases} \quad (3.144)$$

Wall-cell specific dissipation:

$$\omega = \begin{cases} \frac{u_\tau}{\sqrt{\beta^* \kappa y_{p0}}} & high - y^+ (y^+ > 30) \\ \frac{6\nu}{\beta y_{p0}^2} & low - y^+ (y^+ < 5) \\ g_b \frac{6\nu}{\beta y_{p0}^2} + (1 - g_b) \frac{u_\tau}{\sqrt{\beta^* \kappa y_{p0}}} & all - y^+ \end{cases} \quad (3.145)$$

where  $g_b$  is a blending function defined as:

$$g_b = \exp\left(-\frac{Re_y}{11}\right) \quad (3.146)$$

with

$$Re_y = \sqrt{k} y_{p0} / \nu . \quad (3.147)$$

In the above equations,  $y_{p0}$  is the normal distance from the wall to the wall-cell centroid,  $\nu$  is the kinematic viscosity and  $u_{parallel}$  is the component of wall-cell velocity parallel to the wall. At walls, a Neumann boundary condition is used for the turbulent kinetic energy  $k$ , that is,  $(\partial k / \partial n)_w$  is specified. The specific dissipation rate  $\omega$  is specified in the wall cells according to the appropriate method in the wall treatment.

### 3.8.1 $k$ - $\omega$ Turbulence Solver

This solver controls the solution of the  $k$ - $\omega$  model in all the continua for which the model is activated. For each transported variable  $k$  and  $\omega$ , the basic steps that are involved in the solution update are as follows:

- The boundary conditions are updated.
- The reconstruction gradient and cell gradient are computed [see section 3.3 through section 3.5].
- A linear system of equations is generated after discretizing the transport equations of  $k$  and  $\omega$ , i.e., equations (3.124) and (3.125).
- The residual vector is computed as stated in section 3.6.1.
- The linear system is solved to obtain new values of  $k$  and  $\omega$ .
- The transported field variables are updated.
- Iteration continues until the residual is driven to a small value and attains the convergence.

### 3.9 Final Remarks

As mentioned earlier, the volume of fluid (VOF) model is used in our simulations. However, it is worthwhile at this stage to review the other models that are used in simulation of two-phase flow to show the preference of the VOF model over the other multiphase models.

Generally, there are three major multiphase numerical models:

- Eulerian–Lagrangian model; designed for a system consisting mainly of a single continuous phase carrying a relatively small volume of discrete particles, i.e.,

droplets, bubbles, etc. This model is best suited where the interaction between the discrete phase and physical boundary is important.

- Volume of fluid (VOF); convenient for a system containing two or more immiscible fluid phases. The VOF model provides an approach to capture the movement of the interface between the fluid phases. (One set of conservation equation is required for all phases).
- Multiphase model (Eulerian-Eulerian model); suitable for a system containing two or more generalized phases, miscible or immiscible. (One set of conservation equation is required for each phase).

The Lagrangian model was examined during our investigation and many simulations were carried out using different droplet sizes. In these simulations, a fluid film was used to model the heat transfer in the Lagrangian formulation. This model accounts for transport of conserved quantities within the film and interaction with the surroundings. The conclusion from these simulations was that modeling heat transfer in a Lagrangian setup results in an increase in the target surface temperature with droplet size. This may be attributed to the decrease of the total surface area of the droplets with increase of the droplet diameters. The larger surface area or smaller droplet diameters will enhance the heat transfer from the target.

The multiphase model is used to model Eulerian multiphase cases. The multiphase segregated flow model solves a set of conservation equations for each Eulerian phase present in the simulation. The pressure is assumed the same in all phases. The volume fraction gives the share of the flow domain that each phase occupies. Each phase has its own velocity and physical properties. Interfaces separate the multiple phases present in



the simulation. The motions of the phases influence the interface between each pair of phases. The phases can be any kind of fluid in the sense of moving gas, liquid or solid particles. The conservation equations for each phase variable require closure by the definition of phase interactions at each phase interface. This definition consists of suitable models for the interfacial area, and for the rates of interphase transfer of mass, momentum and energy. These closures characterize and vary between different multiphase flow patterns. The Eulerian-Eulerian multiphase model is very expensive in term of CPU time and not feasible from the industrial point of view.

The VOF is an efficient technique to capture the interface in multiphase flow. An important quality of an immiscible phase mixture is that the fluid components remain separated by a sharp interface at all times. In the VOF model, the set of governing equations are solved (i.e., momentum, volume fraction and energy equations), thus the physics of the problem is properly represented and provides results that are more realistic. However, it is a very expensive approach in terms of CPU time, especially when used in conjunction with the conjugate heat transfer method. The conjugate method allows for a coupled heat transfer solution between the solid and fluid, therefore internal iterations are required. The conjugate heat transfer method is discussed in the next chapter.

## CHAPTER 4

### HEAT TRANSFER DUE TO AN IMPINGING JET IN A CONFINED SPACE: STATIONARY DISC

#### 4.1 Introduction

As mentioned earlier, and prior to launching into a full-scale detailed investigation on a complete engine geometry, a generic model is used to enhance our understanding of the underlying physics of an impinging jet. The first set of simulations was carried out to study the heat transfer by an impinging oil jet on a stationary smooth plate with constant heat flux.

In this chapter, a numerical investigation using unsteady three-dimensional Reynolds-Averaged Navier-Stokes (RANS) equations with the  $k-\omega$  SST (shear stress transport) turbulence model was conducted to determine the flow and thermal characteristics of an unsubmerged axisymmetric oil jet in air, impinging normally on to a heated flat disc with finite radius, bounded by cylindrical walls maintained at constant temperature. A 10 mm thick disc subjected to a high uniform heat flux was located at impingement distances ranging from 40 to 80 mm from the nozzle exit, for nozzle exit diameters of  $d = 1.0, 2.0$  and 4.0 mm. The volume of fluid (VOF) method with a high-resolution interface capturing scheme was implemented in STAR-CCM+. A conjugate heat transfer formulation was used to couple the heat transfer solution between the solid and fluid at the interface. In the conjugate approach, one deals simultaneously with conduction in the solid and convection in the fluid.

Using the computational results, a new methodology has been developed to predict the extent of the stagnation zone from the impingement point. Correlations to predict the

dimensionless radial velocity gradient and Nusselt number have also been developed in this chapter.

#### **4.2 Conjugate Heat Transfer (CHT)**

The heat transfer between a solid body and a fluid flowing past it is a conjugate problem, because the heat transfer inside the body is governed by the elliptic Laplace equation, or by a parabolic differential equation, while the heat transfer in the fluid is governed by the elliptic Navier-Stokes equations or by the parabolic boundary layer equation. The solution of such a problem gives the temperature and heat flux distributions on the interface, and there is no need for a heat transfer coefficient, which can be calculated later using the simulation results (Miyamoto et al., 1980; Pozzi & Lupo, 1988; Vynnycky & Kimura, 1996).

The conjugate method allows for a coupled heat transfer solution between the solid and fluid, and thus predicts the heat transfer coefficient more accurately than a decoupled solution. The conjugate heat transfer technique is used in the present simulations to estimate the heat transfer coefficient on the solid surface due to the impingement of the oil jet. In the CHT approach, two separate simulations are set up, one for the fluid analysis and another for the solid thermal analysis. Using an assumed temperature on the wall boundaries, the fluid flow problem is solved to determine local heat transfer coefficients and their corresponding fluid reference temperatures on the walls. The wall temperatures are fed to the solid thermal simulation to evaluate the temperature distribution in the disc, completing one cycle of the iteration. The wall temperatures predicted by the solid thermal simulation are then fed back to the transient flow

simulation and applied to the wall boundaries, and this process continues until a steady-state condition is reached.

### 4.3 Model Setup and Boundary Conditions

The present numerical simulation is used to predict steady-state thermal and flow characteristics when an axisymmetric oil jet (SAE 5W30 oil) impinges onto a finite aluminum disc with 10 mm thickness (typical for a piston application) placed in a cylindrically confined space. The physical domain with relevant boundary conditions is shown in Figure 4.1. Assuming that the flow remains axisymmetric, a 1/20 wedge segment of the entire geometry is used as the computational domain to reduce mesh size and hence the calculation time. The oil exits the nozzle with a temperature of 130°C, flows as a jet towards the disc and spreads out radially along the disc to the cylindrical side walls, eventually falling under gravity to the sump.

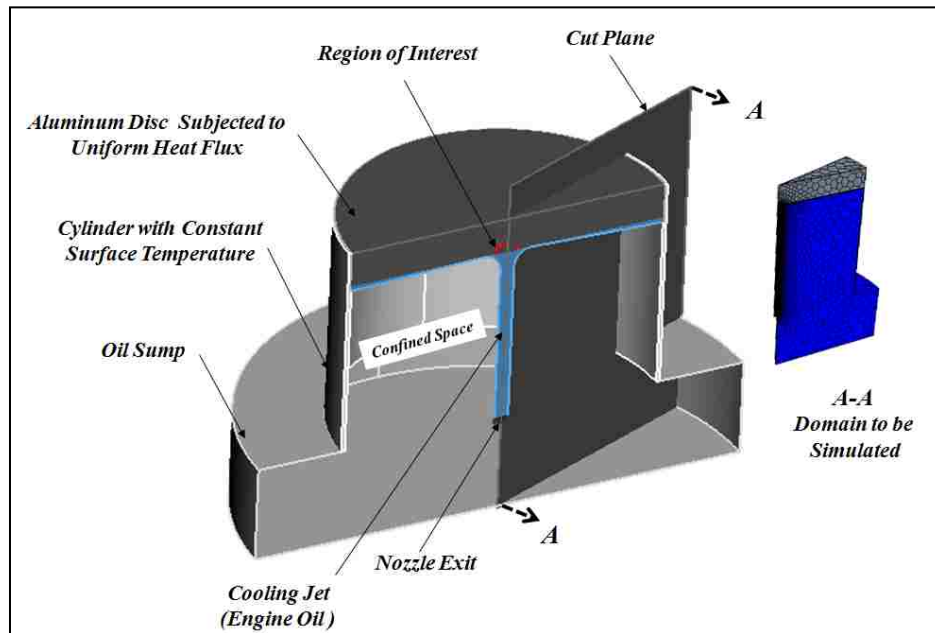


Figure 4.1: Computational domain and relevant boundary conditions

Polyhedral cells were clustered along the jet trajectory, with a cell size of 0.075 mm, to reduce the smearing associated with numerical diffusion and preserve the sharpness of the oil-air interface. The major advantage of polyhedral cells is that they generally have many neighbours (typically of order 10), so gradients can be much better approximated using linear functions. Along the wall and corners, a polyhedral cell is likely to have at least a couple of neighbours, which allows for a reasonable prediction of both gradients and local flow distribution. The fact that there are more neighbours means more storage and computing operations per cell, but the benefit is higher accuracy. A grid sensitivity study was carried out, with a minimum of 31,000 cells for a nozzle with  $d = 2.0$  mm and  $H/d = 20$  to a maximum of 106,000 cells for the  $d = 4.0$  mm nozzle with  $H/d = 15$ . The final cell number chosen for subsequent simulations was obtained from both the grid refinement study, i.e., negligible change in the local heat transfer coefficient, and the validation process, i.e., comparison of the heat transfer coefficient from the simulation with the empirical correlations. Based on analysis of these results, eight layers of fine prism cells were employed in the current study to resolve the wall effect and reduce the artificial dissipation. These prism layers were packed in a 0.4 mm width with a stretching factor of 1.25, producing a  $y^+$  value less than 5.0 at the solid-fluid interface.

A pipe flow was simulated to generate a fully-developed turbulent flow profile, which was then taken as the inlet boundary condition to the computational domain. Three nozzle sizes,  $d = 1.0, 2.0$  and  $4.0$  mm, each at three different nozzle-to-disc spacing  $H = 40, 60$  and  $80$  mm, were used. Symmetry boundary conditions have been assumed on the opposite faces of the  $1/20$  wedge segment, while the disc face and cylindrical side are no-

slip walls. The thermal boundary conditions are also illustrated in Figure 4.1. The top surface of the 90 mm diameter disc is subjected to uniform heat flux of  $270 \text{ kW/m}^2$ , while the cylinder and circumferential disc surfaces are kept at constant temperature  $T = 130^\circ\text{C}$ . All oil and air properties, i.e., dynamic viscosity, density, thermal conductivity and specific heat are evaluated as functions of the local temperature in the computational domain. The input parameters used in this simulation are summarized in Table 4.1.

---

Disc diameter ( $D$ )	90 mm
Disc thickness	10 mm
Oil temperature at nozzle exit ( $T_f$ )	$130^\circ\text{C}$
Circumferential disc surfaces temperature	$130^\circ\text{C}$
Confined cylinder surface temperature	$130^\circ\text{C}$
Sump surface thermal condition	adiabatic
Diameter of fully-developed pipe nozzle ( $d$ )	1.0, 2.0 & 4.0 mm
Bulk velocity of the nozzle exit ( $v_f$ )	20, 40, 60 & 80 m/s for $d=1.0$ & 2.0 mm 10, 20, 30 & 40 m/s for $d=4.0$ mm
Density of air ( $\rho_{air}$ )	Ideal gas
Dynamic viscosity of air ( $\mu_{air}$ )*	Sutherland's law
Air thermal conductivity ( $k_{air}$ )	Sutherland's law
Specific heat of air ( $c_{p-air}$ )	polynomial in $T$
Density of oil ( $\rho_{oil}$ )*	$822 \text{ kg/m}^3$
Dynamic viscosity of oil ( $\mu_{oil}$ )*	$8.424 \times 10^{-3} \text{ kg/m.s}$
Specific heat of oil ( $c_{p-oil}$ )*	$2350 \text{ J/kg.K}$
Oil thermal conductivity ( $k_{oil}$ )*	$0.134 \text{ W/m.K}$
Prandtl number of oil ( $Pr_{oil}$ )*	145
Density of Aluminum ( $\rho_{Al}$ )	$2700 \text{ kg/m}^3$
Specific heat of Aluminum ( $c_{p-Al}$ )	$903 \text{ J/kg.K}$
Aluminum thermal conductivity ( $k_{Al}$ )	$237 \text{ W/m.K}$
Heat flux at disc top surface	$270 \text{ kW/m}^2$

---

\* Parameters evaluated at nozzle exit condition, i.e.,  $130^\circ\text{C}$

Table 4.1: Input parameters for jet impingement onto a stationary disc

As indicated in equation (2.24), the Newton's law of cooling can be stated as:

$$q''_w = q''_{cond.} = q''_{conv.} = -k_f \left( \frac{\partial T}{\partial y} \right)_{y=0} = h(T_{ref} - T_w) \quad (2.24)$$

Here,  $q''_w$  is the convective heat flux at the wall (or interface),  $T_w$  is the wall (or interface) temperature. The convective heat transfer coefficient is evaluated based on specific bulk or reference temperature ( $T_{ref}$ ). In the current simulation, the temperature at the nozzle exit is used as the reference temperature, i.e.,  $T_{ref} = 130^\circ\text{C}$ . The Reynolds number is evaluated at the jet entrance condition, i.e., at  $T_{ref} = 130^\circ\text{C}$ , while the local Nusselt number at the fluid-solid interface is evaluated at the corresponding local temperature. The stagnation zone Nusselt number is calculated by averaging the local Nusselt number over a specific surface area representing the stagnation region corresponding to each case. The time step used in the current simulation is  $\Delta t = 1 \times 10^{-3}$  s with five internal iterations per time step. The maximum Courant number for all cases was found to be less than 1.0, which satisfies the CFL condition discussed in Chapter 3.

One of the crucial issues encountered in heat transfer simulations is the calculation of the thermal eddy diffusivity ( $\alpha_t$ ), which necessitates the prediction of the turbulent Prandtl number ( $Pr_t = \nu_t / \alpha_t$ ). The development of models to predict  $Pr_t$  requires many assumptions regarding the behaviour of turbulence parameters. Alternatively, the turbulent Prandtl number may be evaluated experimentally (Gutfinger, 1975). For very high Prandtl number fluids ( $Pr_{oil} \approx 140$  at  $130^\circ\text{C}$ ), Kays (1994) reported that the experimental value of turbulent Prandtl number must be close to 1.0 in the region  $0 < y^+ < 5$ . The effect of different turbulent Prandtl numbers on the local Nusselt number was numerically investigated by Behnia et al. (1996) and the results are in good agreement with experimental results in the range of  $Pr_t = 0.72 - 0.92$ . Turbulent Prandtl numbers of 0.7, 0.8 and 0.9, which lie in the range suggested in Behnia et al. (1996), were tested for the current simulations. The value  $Pr_t = 0.9$  was found to be most suitable in

terms of Nusselt number comparison between the simulation and the empirical correlation.

First-order implicit time marching and second-order spatial differencing are used to discretize the governing partial differential equations. A segregated flow model, which solves the flow equations in an uncoupled manner, is used to solve the discretized equations. The linkage between the momentum and continuity equations is achieved with a predictor-corrector approach. The complete formulation can be described as an implementation on a collocated variable arrangement with a Rhie and Chow pressure-velocity coupling combined with a SIMPLE algorithm (see Chapter 3). In the current study, the results are considered to have converged when the continuity and momentum residuals fall below  $10^{-6}$ .

#### **4.4 Validation of Numerical Simulation**

The correlations provided in the literature are mostly deduced from experimental data, which are obtained from jets impinging normally on a flat surface placed in an open domain. Therefore, it is worthwhile as a first step in the validation process to examine the effect of the radial confinement on the Nusselt number before performing the comparison between the results from computations and empirical correlations. For this purpose, several simulations corresponding to different nozzle sizes and Reynolds numbers were carried out. The effect of confinement by a cylinder of radius  $R$ , for  $R/d$  ranging from 5.0 to 40.0, is shown in Figure 4.2.



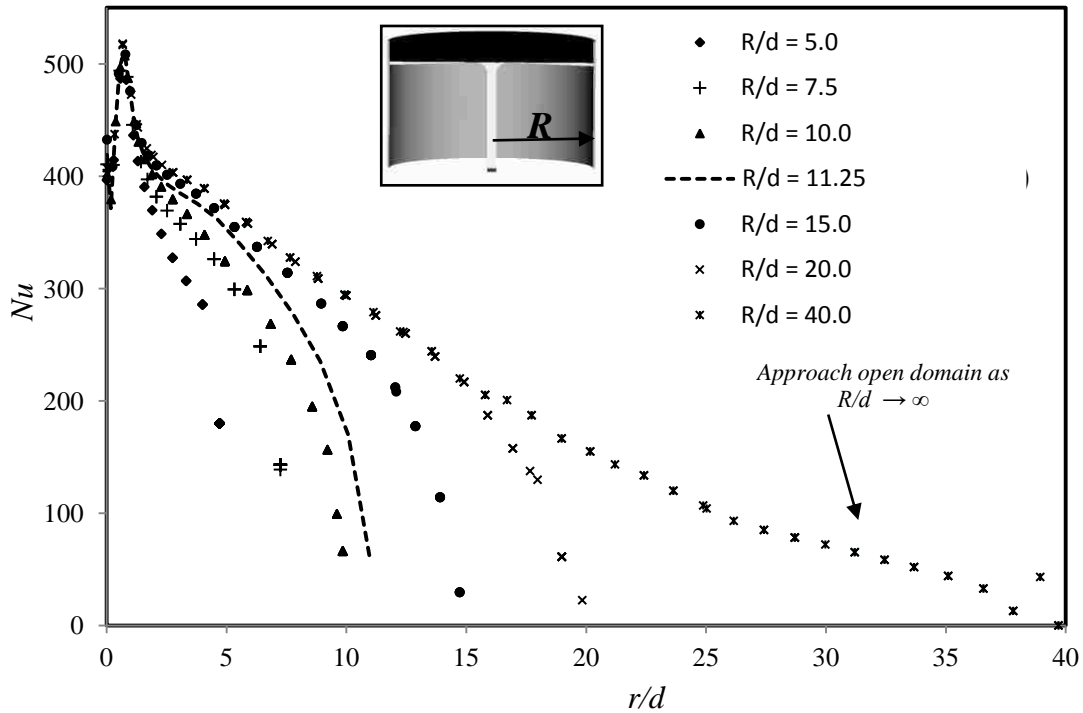


Figure 4.2: Effect of domain confinement on local Nusselt number obtained for nozzle size  $d = 4.0$  mm at  $H/d = 15$  and  $Re_d = 12000$

It is obvious from the above figure that the local Nusselt number varies with  $R$ . However, the location and magnitude of the maximum Nusselt numbers are invariant, regardless of the proximity of the outer wall. For values of  $R/d > 11.25$ , the local Nusselt number profiles in the region near the stagnation point ( $r/d < 5$ ) are nearly identical, with a maximum difference of less than 5%. Hence, the correlations derived from open domain data should still be valid in the region  $0 < r/d < 5$  for the confined domain.

The stagnation zone Nusselt numbers were numerically predicted at fixed nozzle-to-disc spacing of  $H = 60$  mm for three nozzle sizes  $d = 1.0, 2.0$  and  $4.0$  mm and a range of Reynolds numbers. The numerical results are compared with data from equation (2.39)

given in Chapter 2, as shown in Figure 4.3. The empirical correlation given by equation (2.39) predicts the Nusselt number of the stagnation zone which, based on the experimental data, appears to extend to  $r/d \approx 0.75$  (Stevens & Webb, 1991). Therefore, for purposes of this validation, the stagnation zone Nusselt number from the simulation was also computed by averaging the local Nusselt number over a circular area extending between  $0.0 \leq r/d \leq 0.75$ . Although the expression given by equation (2.39) used to correlate the experimental data is intended for the range of  $H/d < 20$ , this correlation produces good results for even larger nozzle-to-disc spacing, e.g.,  $H/d \leq 80$ , in the present work. The comparison between the results for the stagnation zone Nusselt number from the computations and correlation given by equation (2.39) reveals average differences of 3.5, 5.0 and 8.0% corresponding to nozzles sizes of  $d = 1.0, 2.0$  and  $4.0$  mm, respectively.

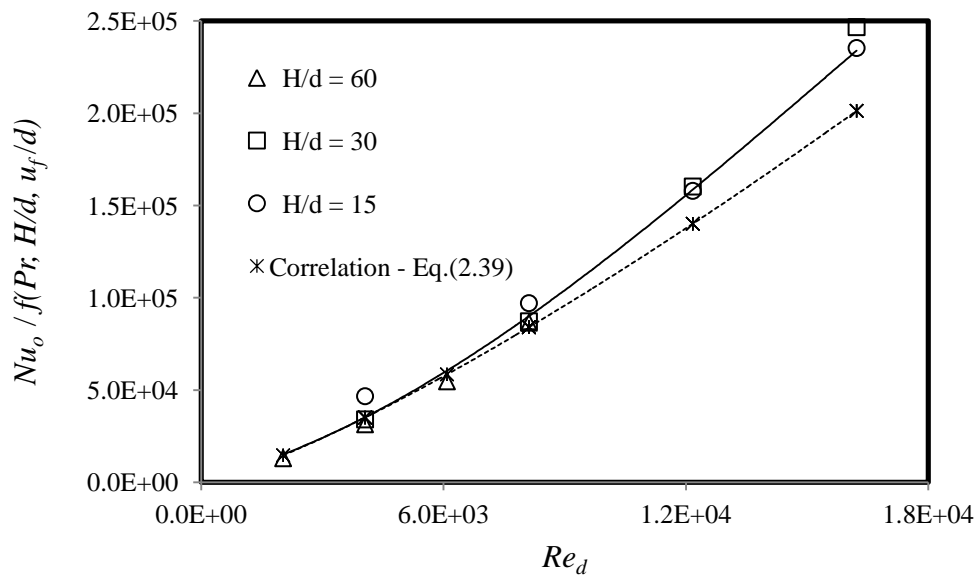


Figure 4.3: Comparison of computed stagnation zone Nusselt number with correlation given by equation (2.39), for  $H = 60$  mm

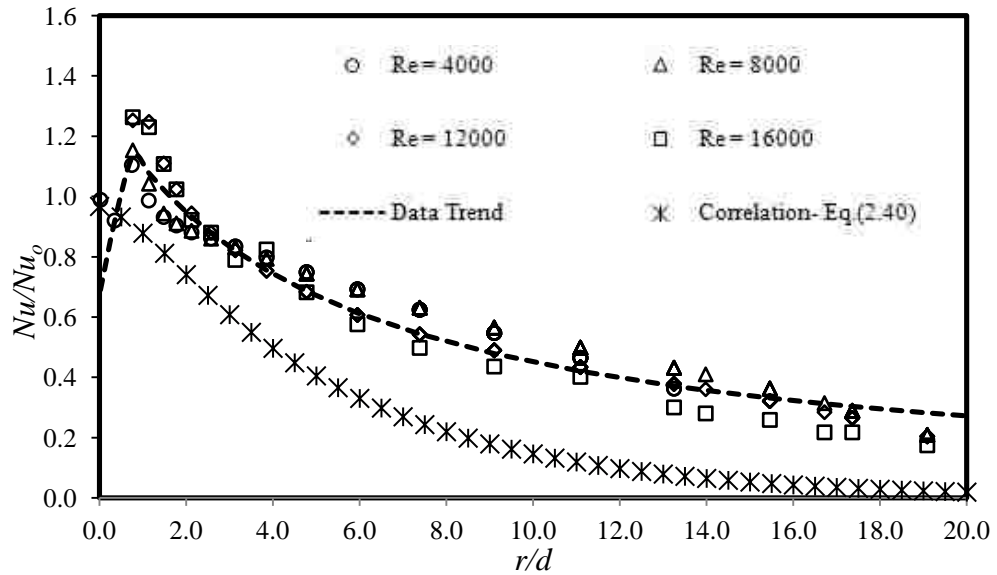


Figure 4.4: Comparison of computed local Nusselt number with correlation given by equation (2.40);  $H = 60$  mm,  $d = 2$  mm

The local Nusselt numbers evaluated from the simulations are also compared in Figure 4.4 with the results from equation (2.40) given in Chapter 2, for nozzle size  $d = 2.0$  mm at  $H/d = 30$ . The correlation given by equation (2.40) applies only to the region before transition to turbulence occurs. Beyond that point, the correlation serves as a lower bound on the local heat transfer but, as reported in Stevens & Webb (1991), does not accurately predict  $Nu/Nu_o$  [see Stevens & Webb (1991), Figures 5 & 6]. This observation is clearly shown in Figure 4.4.

## 4.5 Results

In this section, first, we will investigate the effect of nozzle configuration on thermal characteristics for long jets. This is followed by a discussion of the computational results from the simulation for the stagnation and local Nusselt number due to the jet impingement.

### 4.5.1 Effect of Nozzle Configuration (Long Jet)

In this study, the effect of nozzle geometry on thermal characteristics was examined for long jets. Three nozzle geometries with exit diameter of  $d = 1.0$  mm were employed as shown in Figure 4.5. They consist of a pipe nozzle, a converging nozzle and a converging nozzle with a short pipe exit. A nozzle-to-target spacing of  $H/d = 60$  was used in each case. The computational domain shown in Figure 4.1 is used in these simulations. The bulk exit velocity remains constant for all three nozzles, i.e., 30 m/s and the turbulence intensities in all three cases are less than 3.0%. The top surface of the 90 mm diameter disc is subjected to uniform heat flux of  $50 \text{ kW/m}^2$  (Agarwal et al., 2011), while all other boundary conditions are the same as in Table 4.1.

The velocity gradient is only a function of the velocity profile in the jet if the turbulence intensity is mild, as mentioned in Chapter 2. For long jets, the viscosity tends to eliminate the gradient in the radial direction and hence creates a more uniform velocity profile which results in a constant velocity gradient at the stagnation point. Figure 4.6 illustrates the suppression of the velocity gradient for long jets from a converging nozzle. It is obvious from this figure that the velocity gradient in the radial direction diminishes after  $H/d > 16$  for the converging nozzle, and after  $H/d > 20$  approximately (figure not

shown here) for other two nozzles used in the simulation. A constant velocity gradient at the stagnation point means constant thermal characteristics.

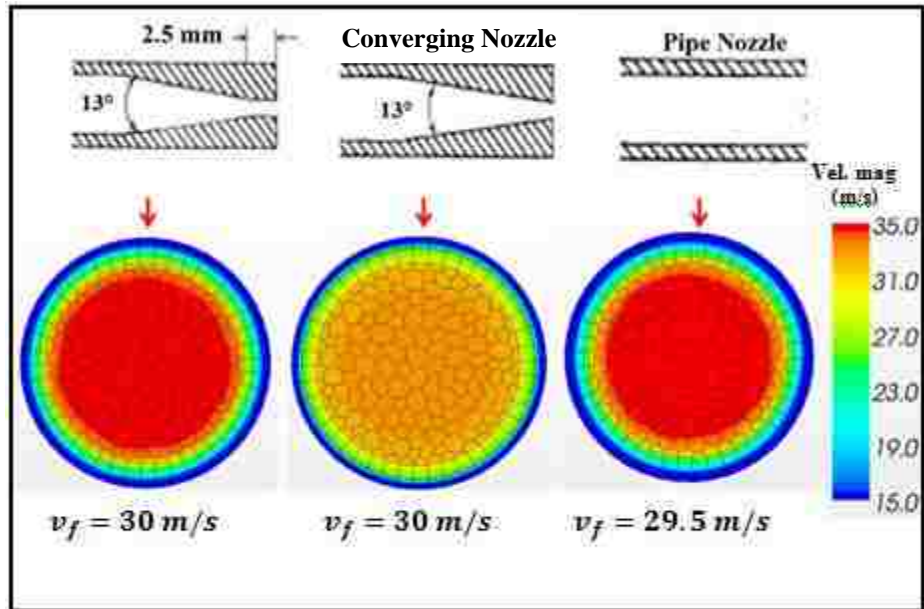


Figure 4.5: Exit velocity profiles for three nozzles sizes

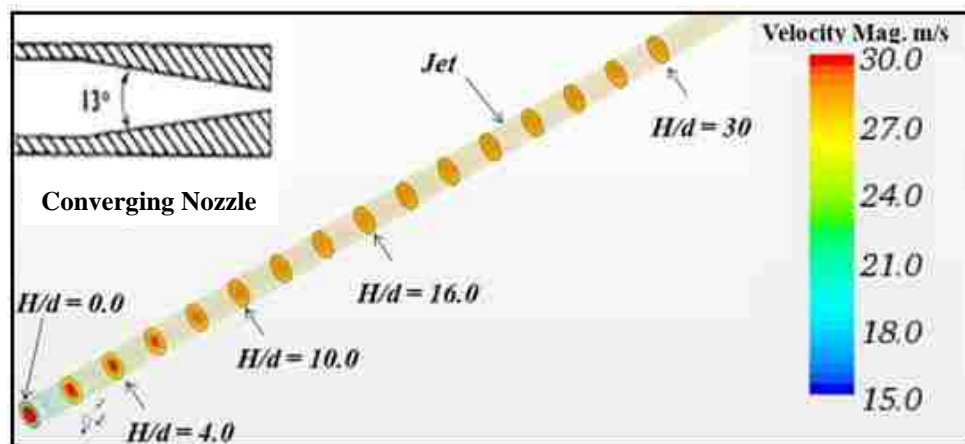


Figure 4.6: Suppression of the velocity gradient in radial direction (velocity relaxation)

More insight into the thermal characteristics can be obtained by extracting the stagnation zone Nusselt number, stagnation zone temperature, disc average temperature and the interface surface average temperature for the three nozzle geometries, as shown in Table 4.2 for  $H/d = 60$ . The key observation from the data in Table 4.2 is that, for long jets impinging on a stationary boundary, the nozzle geometry has no significant effect on the thermal characteristics.

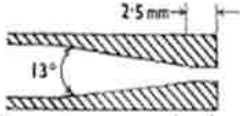
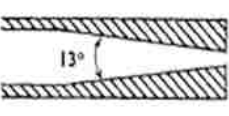

			
Stagnation zone Nusselt number $Nu_o$	138.3	137	138.6
Stagnation zone temperature (°C)	171	171.8	171.7
Disc average temperature (°C)	194.8	195	195
Solid-fluid interface average temp. (°C)	193.4	194	193.8

Table 4.2: Summary of thermal characteristics for different nozzle geometries

Since the effect of nozzle configuration on the thermal characteristics is weak for long jets and the pipe nozzle is the more common type used in industry, all subsequent simulations for the generic models (Chapter 4 & 5) employ the pipe nozzle. However, the final goal of this dissertation is to simulate automotive piston cooling, which is concerned with long jets from oil squirters that have a unique shape. This will be addressed in Chapter 6.

#### 4.5.2 Stagnation Zone Nusselt Number ( $Nu_o$ )

There is no rigid definition for the stagnation zone. The size of the stagnation zone may be theoretically predicted by calculating the radius at which the boundary layer and the region around the stagnation point have the same thickness (Sharan, 1984), which yields  $r/d = 0.787$ . On the other hand, Stevens & Webb (1991) found that the stagnation zone for turbulent jet conditions only extends to  $r/d = 0.75$ . The estimate of stagnation zone proposed in Liu et al. (1991) is based on the criterion that the stagnation zone should include the location of the maximum local heat transfer coefficient.

The radial velocity gradient  $\partial u_r / \partial r$  plays a significant role in the determination of the stagnation zone heat transfer coefficient, and therefore it is more appropriate to incorporate it when identifying the boundaries of the stagnation region. Literature indicates that this velocity gradient is highly dependent on the dimensional quantity  $v_f/d$ , and that the relation is linear in the case of laminar jets (Wang et al., 1989).

Additional insight into the stagnation zone can be gained by examining the contours of the radial velocity gradient beneath the stagnation region, such as those shown in Figures 4.7, 4.8 and 4.9 for the case of  $d = 1.0, 2.0$  and  $4.0$  mm and  $H/d = 60, 30$  and  $15$ , respectively. The upper-left corner of each figure is the stagnation point ( $r/d = 0.0, z/d = 0.0$ ). Our basic estimation of the stagnation zone shows that it extends up to the interface between the positive and negative gradients, i.e., up to the location where the contour of positive radial velocity detaches from the solid wall. The radial location where the radial velocity gradient  $\partial u_r / \partial r$  along the wall becomes insignificant is indicated by the short dashed vertical (red) line. Some relevant observations can be drawn from close examination of these figures. The radial extent of the stagnation zone increases with

Reynolds number for a given nozzle size. The radial velocity gradient increases with the quantity  $v_f/d$ , but achieves its maximum value at  $r/d = 0.5$  for all values of Reynolds number. The high radial velocity gradient levels will enhance the heat transfer at the stagnation region. The extent of the stagnation zone and the Nusselt number for the different nozzles at several Reynolds numbers are tabulated in Table 4.3. The extent of the stagnation zone varies from 0.75 to 0.88 for  $d = 1.0$  and  $2000 < Re_d < 8000$ , and from 0.68 to 0.70 for  $d = 4.0$  and  $4000 < Re_d < 16000$ . This is in contrast to the work of other researchers who have defined the stagnation zone based on a specific fixed value of  $r/d$ . While the effect of the extent of the stagnation zone on the Nusselt number is negligible for larger nozzles, for small diameter nozzles at higher Reynolds number the difference in predicted stagnation zone Nusselt number can be as much as 22%.

Normally, the radial velocity gradient  $\partial u_r/\partial r$  at the stagnation point is analytically evaluated using inviscid theory. As mentioned earlier in Chapter 2, the dimensionless radial velocity gradient  $B = 2(d/v_f)(\partial u_r/\partial r)$  is used in this study. The velocity gradient  $\partial u_r/\partial r$  and the dimensionless velocity gradient  $B$  are evaluated just above the stagnation boundary layer and a linear dependence of radial velocity  $u_r$  on radial location  $r/d$  in the stagnation zone is assumed. The radial velocity gradient results are plotted versus  $v_f/d$  as shown in Figure 4.10. The dimensionless radial velocity gradient  $B$  tends to a constant  $B \approx 2.22$  as  $v_f/d$  exceeds 40,000 as shown in Figure 4.10b. The data in Figure 4.10a were correlated using a power law (dashed line), and the expression for dependence of this velocity gradient on  $v_f/d$  is approximated by:

$$\partial u_r/\partial r = 1.9(v_f/d)^{0.95}. \quad (4.1)$$



The correlation given by equation (4.1) is used to estimate the radial velocity gradient at the stagnation point for long ( $H/d > 10$ ) circular liquid jets.

The dependence of stagnation zone Nusselt number  $Nu_o$  on Reynolds number in the range  $2000 < Re_d < 16,500$  for the three nozzle sizes is shown in Figure 4.11. The general observation extracted from this figure is the minor dependence of  $Nu_o$  on the nozzle-to-disc spacing. All computational data shown in Figure 4.11 can be correlated using the expression

$$Nu_o = 0.0142 Re_d^{0.565} Pr^{0.4} B^{3.41} . \quad (4.2)$$

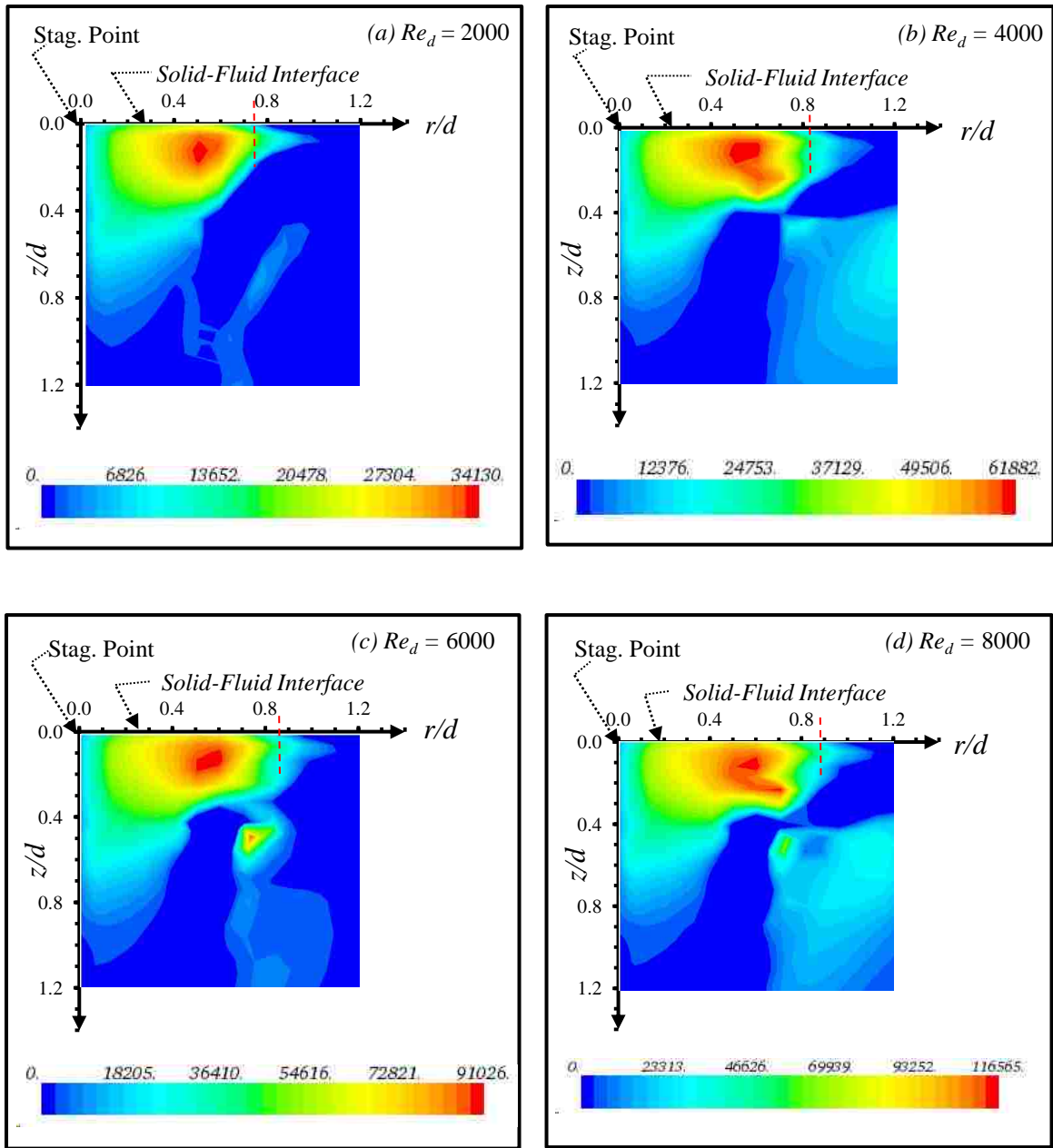


Figure 4.7: Contours of radial velocity gradient  $\partial u_r / \partial r$  and radial extent of the stagnation zone for  $d = 1.0$  mm at  $H/d = 60$ ; (a)  $Re_d = 2000$ , (b)  $Re_d = 4000$ , (c)  $Re_d = 6000$  and (d)  $Re_d = 8000$

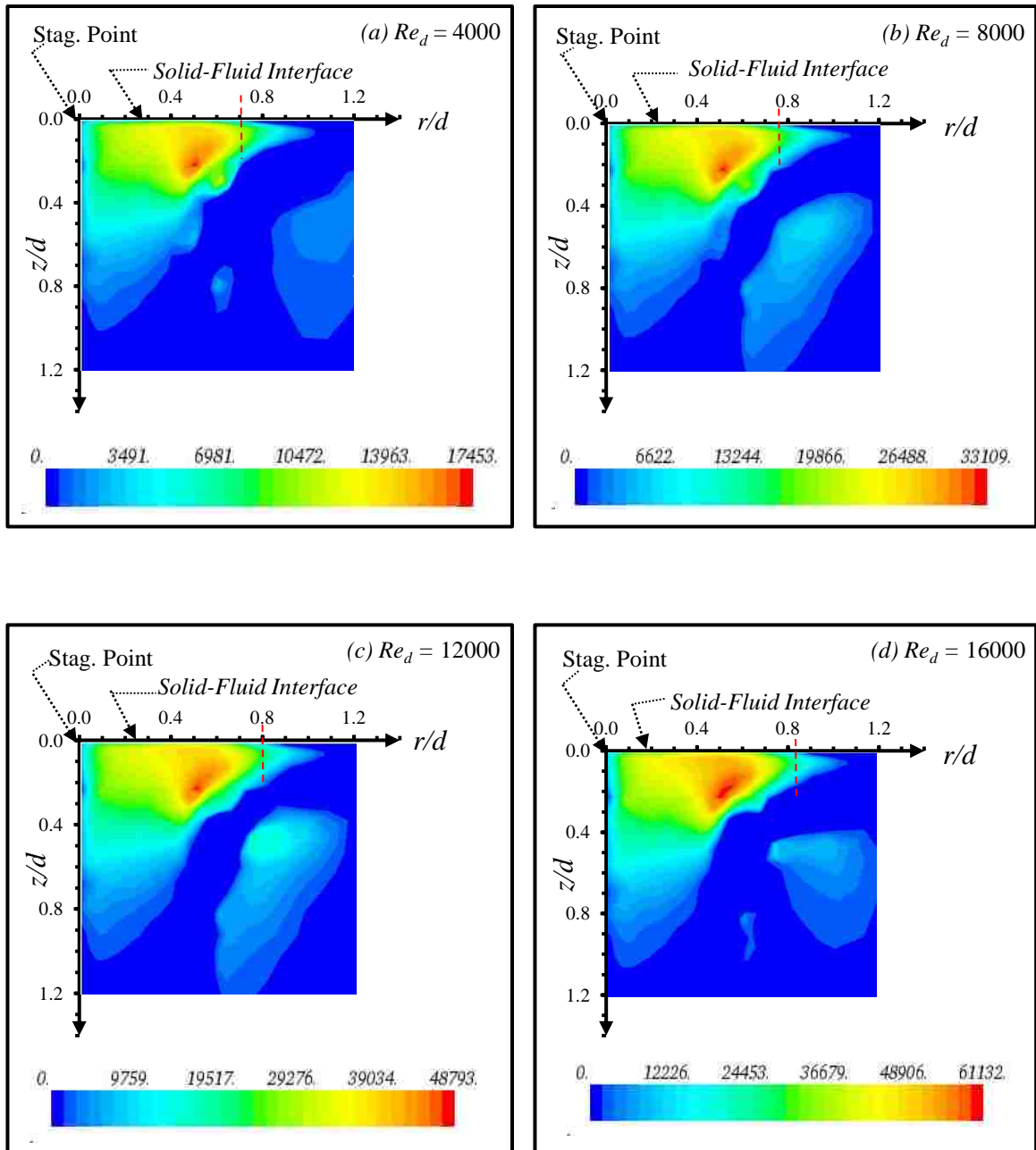


Figure 4.8: Contours of radial velocity gradient  $\partial u_r / \partial r$  and radial extent of the stagnation zone for  $d = 2.0$  mm at  $H/d = 30$ ; (a)  $Re_d = 4000$ , (b)  $Re_d = 8000$ , (c)  $Re_d = 12000$  and (d)  $Re_d = 16000$

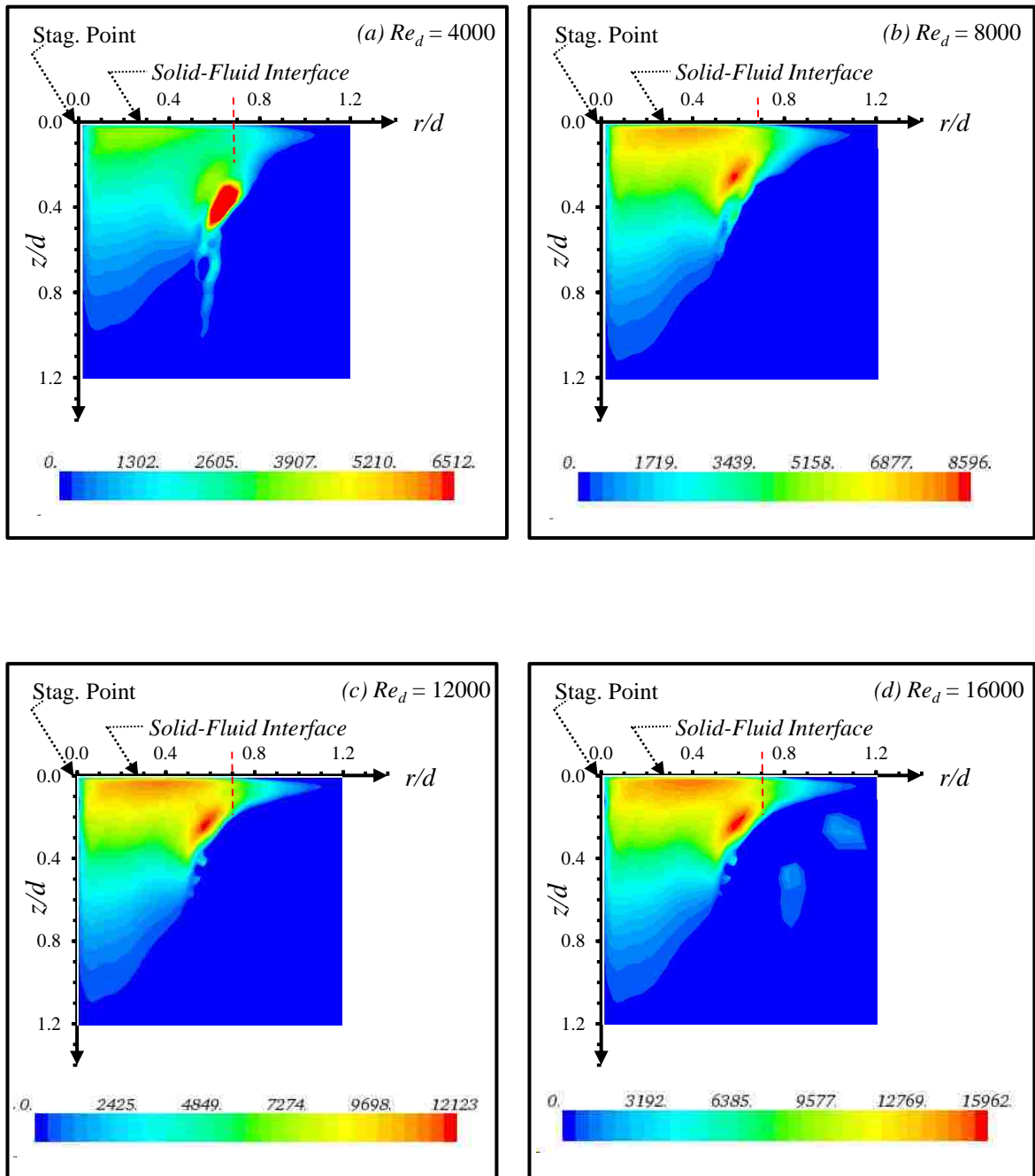
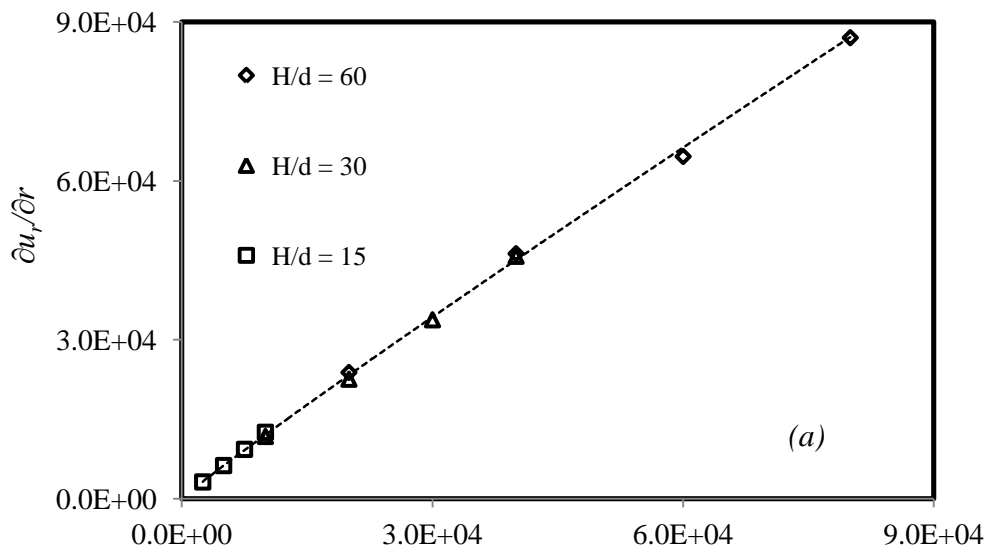


Figure 4.9: Contours of radial velocity gradient  $\partial u_r / \partial r$  and radial extent of the stagnation zone for  $d = 4.0$  mm at  $H/d = 15$ ; (a)  $Re_d = 4000$ , (b)  $Re_d = 8000$ , (c)  $Re_d = 12000$  and (d)  $Re_d = 16000$

$H/d$	$Re_d$	$v_f/d$ (1/s)	Stagnation Zone	
			Extent $r_o/d$	$Nu_o$
60	2000	20000	0.75	118
	4000	40000	0.82	153
	6000	60000	0.85	190
	8000	80000	0.88	236
<hr/>				
30	4000	10000	0.70	181
	8000	20000	0.76	280
	12000	30000	0.8	360
	16000	40000	0.82	431
<hr/>				
15	4000	2500	0.68	351
	8000	5000	0.68	412
	12000	7500	0.70	469
	16000	10000	0.70	522

Table 4.3: Stagnation zone characteristics, for  $H = 60$  mm



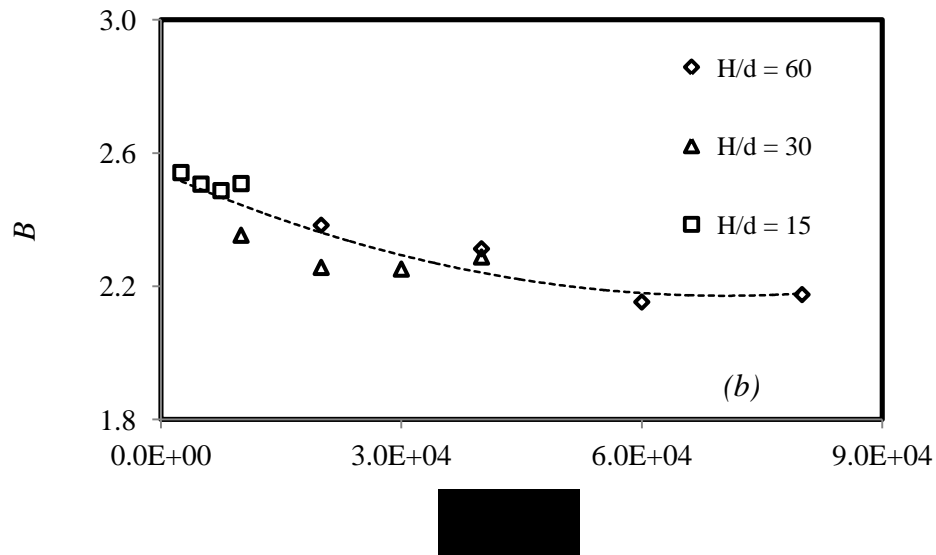


Figure 4.10: Dependence of: (a) stagnation point radial velocity gradient and (b) dimensionless radial velocity gradient, on the parameter  $v_f/d$

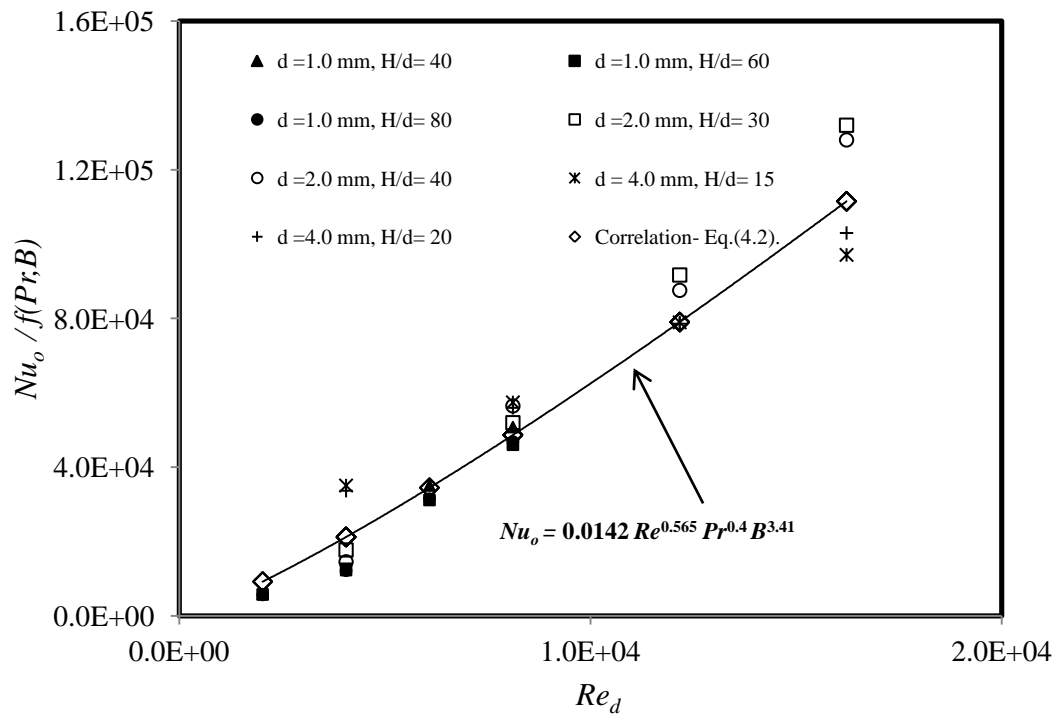


Figure 4.11: Variation of stagnation zone Nusselt number with Reynolds number

Equation (4.2) predicts the computational data with an average error of less than 10%, for all nozzle sizes and jet Reynolds numbers used in this study. A comparison between equation (2.39) and equation (4.2) reveals that they have almost identical exponents of both Reynolds and Prandtl number. However, equation (4.2) does not include the spacing term  $H/d$  because this equation is used to predict the stagnation zone Nusselt numbers only for long jets, where the influence of nozzle-to-target spacing is insignificant. A wide range of Reynolds numbers ( $4000 < Re_d < 55,000$ ) and Prandtl numbers ( $1.0 < Pr < 300$ ) have been used to compare equation (2.39) and equation (4.2). The average difference in the results from these equations is less than 10%. Contrary to equation (2.39), all parameters used in equation (4.2) are dimensionless quantities.

#### **4.5.3 Local Nusselt Number ( $Nu$ )**

Following impingement, the flow turns and enters a wall jet region where the flow moves laterally outwards parallel to the wall. Within the stagnation zone, the oil jet flow is strongly influenced by the disc, and is rapidly decelerated in the axial direction and rapidly accelerated in the radial direction. Due to the conservation of momentum, the wall jet accelerates after the flow turns and as the boundary layer develops. The thickness of the liquid film adjacent to the wall initially decreases with radius but, as the accelerated flow is transformed into a decelerated wall jet, the liquid film thickens. The wall jet has a minimum thickness and a maximum speed within  $0.75d - 3.0d$  from the jet axis (Zuckerman & Lior, 2006).

The profiles of local Nusselt number normalized by  $Nu_o$  for the three nozzle sizes are shown in Figure 4.12. It is worthwhile to mention that the amount of local heat transfer is

implicitly embedded in the non-dimensional expressions for Nusselt number given in this figure. Several observations can be drawn from Figure 4.12; first, the normalized local Nusselt number, for a given nozzle diameter, can be considered as a function of  $r/d$  only and the Reynolds number dependence is very slight in the region of interest. Second, the local Nusselt number is not constant in the stagnation zone, contrary to that reported by previous studies, but follows the distribution of the radial velocity gradient in this region (see Figures 4.7- 4.9). The uniform local Nusselt number found in the experiments may be due to inadequate spatial resolution to capture the temperature distribution in the narrow stagnation region. Third, beyond the stagnation region, the profile of normalized local Nusselt number is shifted upward and becomes more flattened with the increase of the nozzle size. This may be attributed to the mass flow rate, which increases with nozzle size for a given Reynolds number. A higher mass flow rate creates a thicker oil sheet adjacent to the wall and retains the thermal boundary layer below the surface of the fluid sheet. This will maintain the free stream temperature of the wall jet, i.e., the surface temperature of the film remains at the inlet temperature of the jet. On the contrary, in a smaller jet, the thermal boundary layer approaches the free surface and the temperature of the liquid surface increases with the radius. Both cases are illustrated in Figure 4.13. Here,  $t$  is the distance from the wall through the layer. Consequently, a more uniform temperature distribution at the interface between the oil sheet and the impinging surface will be obtained in the case of larger nozzles rather than smaller ones, as shown in Figure 4.12. The temperature contours show a gradual change for nozzle size  $d = 2.0$  mm, while they are more uniform for  $d = 4.0$  mm. As a result, a more uniform heat transfer coefficient along the wall will be attained for larger nozzles, which nearly flattens the



profile of the local Nusselt number. Fourth, as shown in Figure 4.12, a drop in local Nusselt number occurs within a narrow strip immediately away from the stagnation point for jets whose radial velocity gradients are small, i.e.,  $v_f/d \leq 2.0 \times 10^4 \text{ s}^{-1}$ , or  $B > 2.3$ .

Additional insight into the flow characteristics can be obtained by examining the contours of the radial velocity as shown in Figure 4.15. In these figures, the radial velocity contours for the three nozzle sizes 1.0, 2.0 and 4.0 mm corresponding to  $v_f/d = 8.0 \times 10^4$ ,  $4.0 \times 10^4$  and  $1.0 \times 10^4$ , respectively, are displayed immediately beneath the impinging region, over the range  $0 \leq r \leq 0.5$  mm. The upper-left corners are the stagnation point ( $r/d = 0.0$ ), while the upper-right corners are the radial distances from the stagnation point ( $r/d = 0.5, 0.25$  and  $0.125$ ) corresponding to the three nozzle sizes. It is evident that the radial velocity is highly correlated with the quantity  $v_f/d$ . The radial velocity around the stagnation point is very small (nearly zero) for nozzle size of 4.0 mm, but the radial velocities are  $u_r = 7.0$  and  $5.0$  m/s for nozzle sizes  $d = 1.0$  and  $2.0$  mm, respectively. The drop in Nusselt number will occur in the regions where the radial velocity is almost equal to zero. Subsequently, the Nusselt number will increase when the radial velocity increases, thereby enhancing the local heat transfer coefficient. Based on these results, it is postulated that the heat transfer coefficient strongly depends on the fluid velocity parallel to the wall, i.e., the radial velocity.

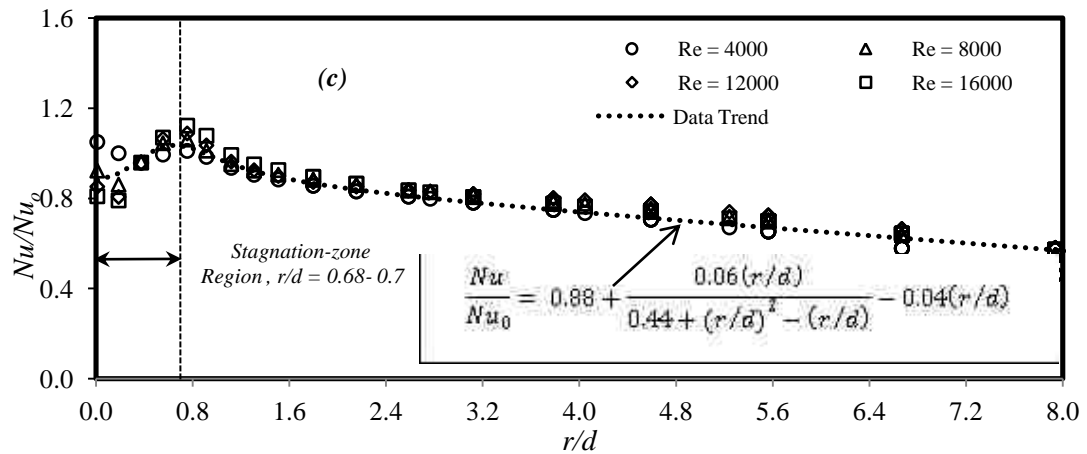
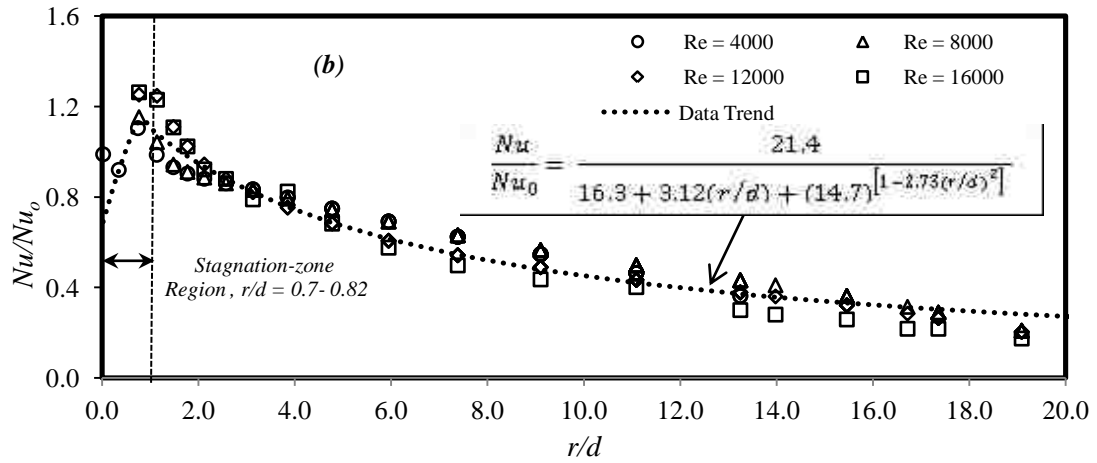
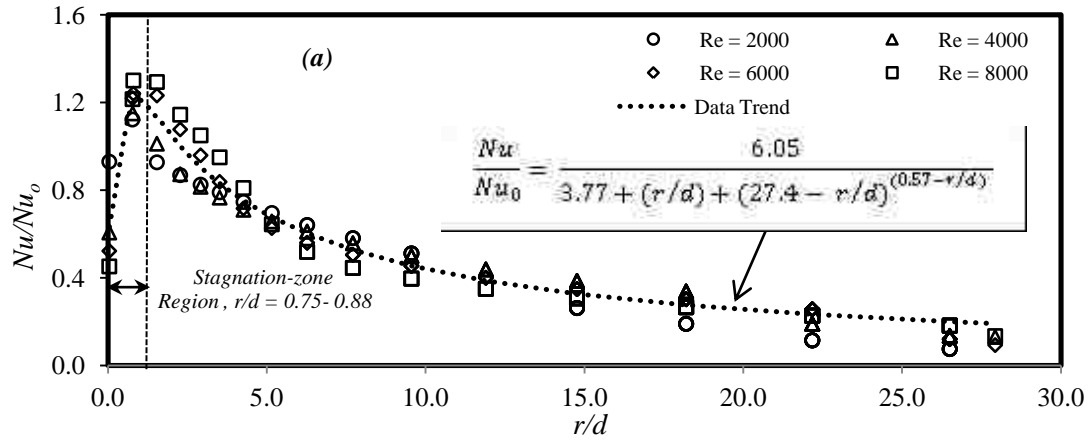


Figure 4.12: Local Nusselt number  $Nu$  normalized by  $Nu_0$ ,  $H = 60$  mm:

(a)  $H/d = 60$ , (b)  $H/d = 30$ , (c)  $H/d = 15$

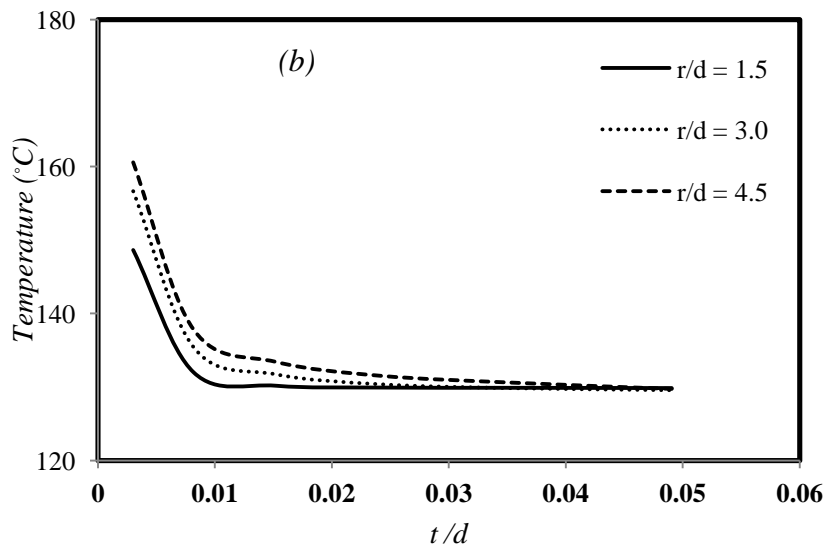
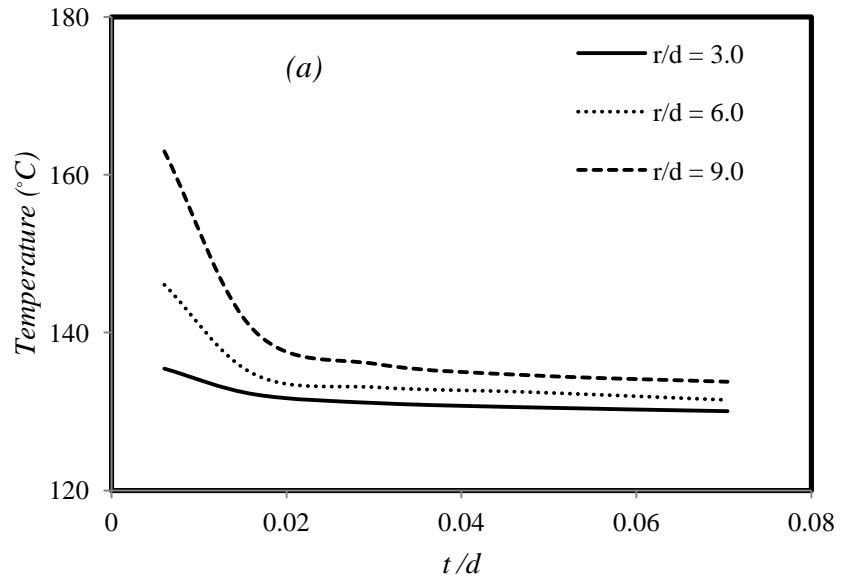


Figure 4.13: Temperature distribution across the fluid film at three different locations downstream of the stagnation point,  $H = 60$  mm,  $Re_d = 12000$ ;

(a)  $H/d = 30$ , (b)  $H/d = 15$

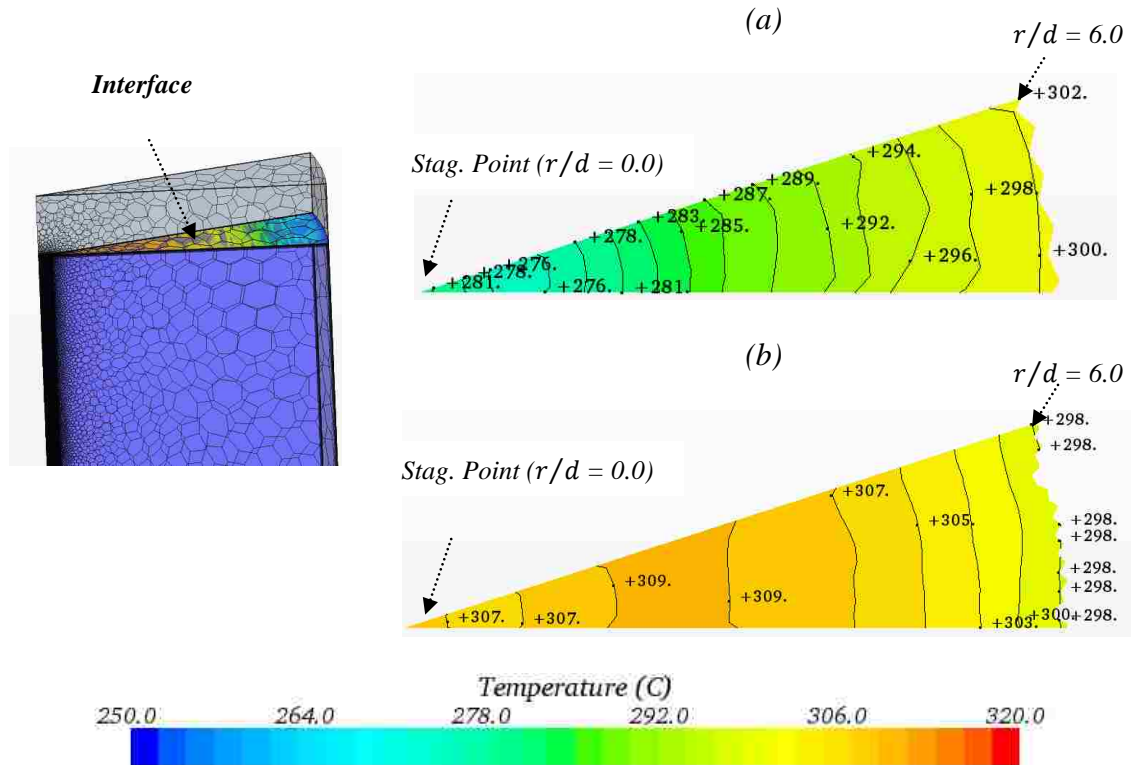


Figure 4.14: Temperature distribution at the interface between the oil sheet and impinging surface,  $H = 60$  mm,  $Re_d = 12000$ ; (a)  $H/d = 30$ , (b)  $H/d = 15$

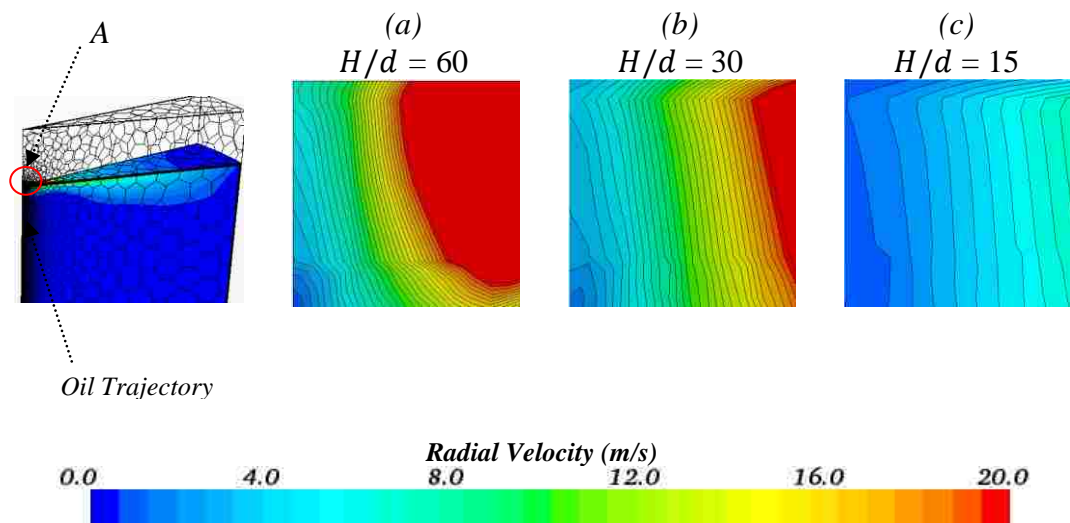


Figure 4.15: Distribution of radial velocity beneath the stagnation region (A);  
 (a)  $d = 1.0$  mm,  $Re_d = 8000$ , (b)  $d = 2.0$  mm,  $Re_d = 16000$ , (c)  $d = 4.0$  mm,  $Re_d = 16000$

#### 4.5.4 Disc Temperature Profile

In view of the previous discussion, it is obvious that smaller size nozzles are more convenient if the goal of the jet impingement is to cool down a small region. For a given Reynolds number, smaller nozzles require less mass flow rate to provide a higher heat transfer coefficient, compared with larger size nozzles. However, the larger size nozzle is appropriate if the purpose of the jet impingement is to get a more uniform temperature distribution on the impinging surface. A proper understanding of the thermal characteristics can be gained by examining the effect of Reynolds number and nozzle sizes on the average temperature of the disc in the stagnation zone, as illustrated in Figure 4.16. For a given Reynolds number, e.g.,  $Re = 8000$ , Figure 4.16a shows that the temperature of the disc in the stagnation zone drops by 5% for nozzle size  $d = 2.0$  mm, and by 15% for  $d = 1.0$  mm, respectively, compared to the 4.0 mm nozzle. This can be attributed to the radial velocity gradient in the stagnation region, which increases for smaller size nozzles. Consequently, this enhances the heat transfer coefficient and reduces the stagnation region temperature. Comparing the average temperature of the stagnation zone with and without jet cooling, the average drop corresponding to all Reynolds number is 40% and 36% for nozzle sizes of 2.0 and 4.0 mm, respectively. Figure 4.16b also demonstrates that the average temperature of the disc is independent of the nozzle size for a specific Reynolds number.

The disc temperature profiles corresponding to the three nozzle sizes and different Reynolds numbers are shown in Figure 4.17. For a given nozzle size, the contours of higher temperature move towards the upper surface of the disc as Reynolds number increases. It is obvious that the nozzle size has a slight effect on temperature profile for

specific Reynolds number. Therefore, increasing the nozzle size, i.e., increasing the mass flow rate for specific Reynolds number, will not significantly change the temperature profile, but rather provide a more homogeneous temperature distribution at the impinging surface.

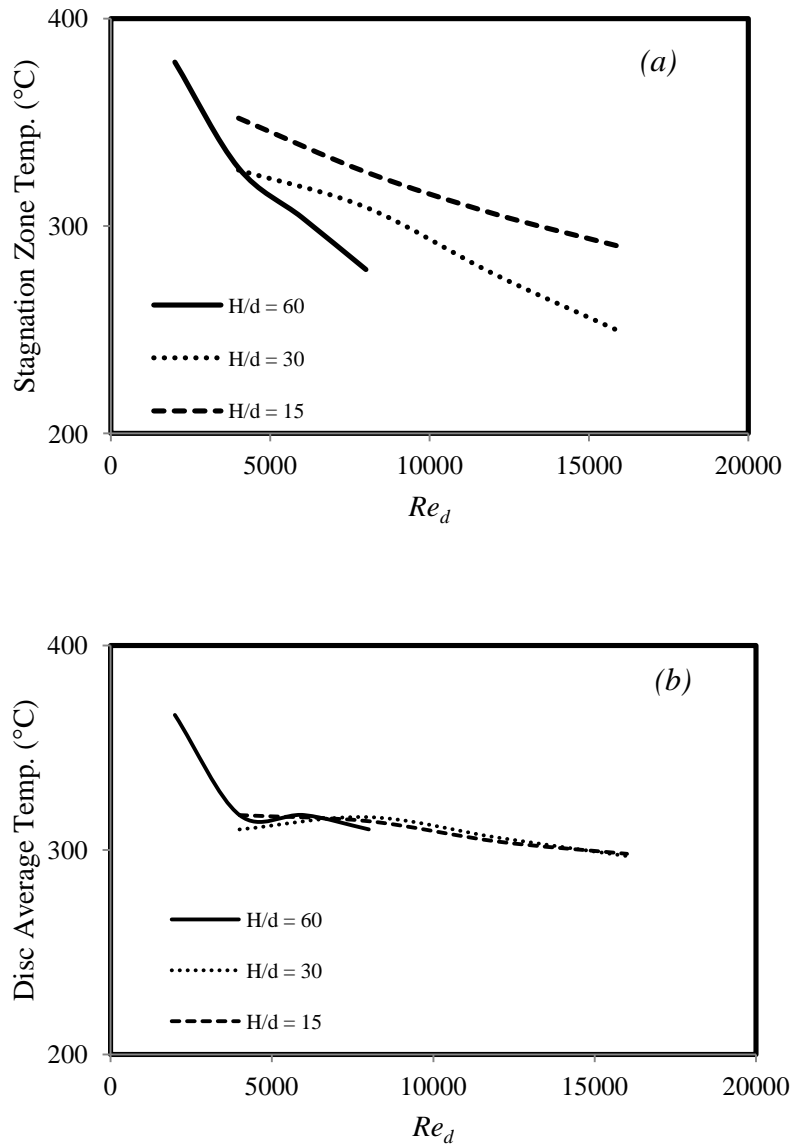


Figure 4.16: Effect of Reynolds number on (a) stagnation zone average temperature, (b) disc average temperature;  $H = 60$  mm

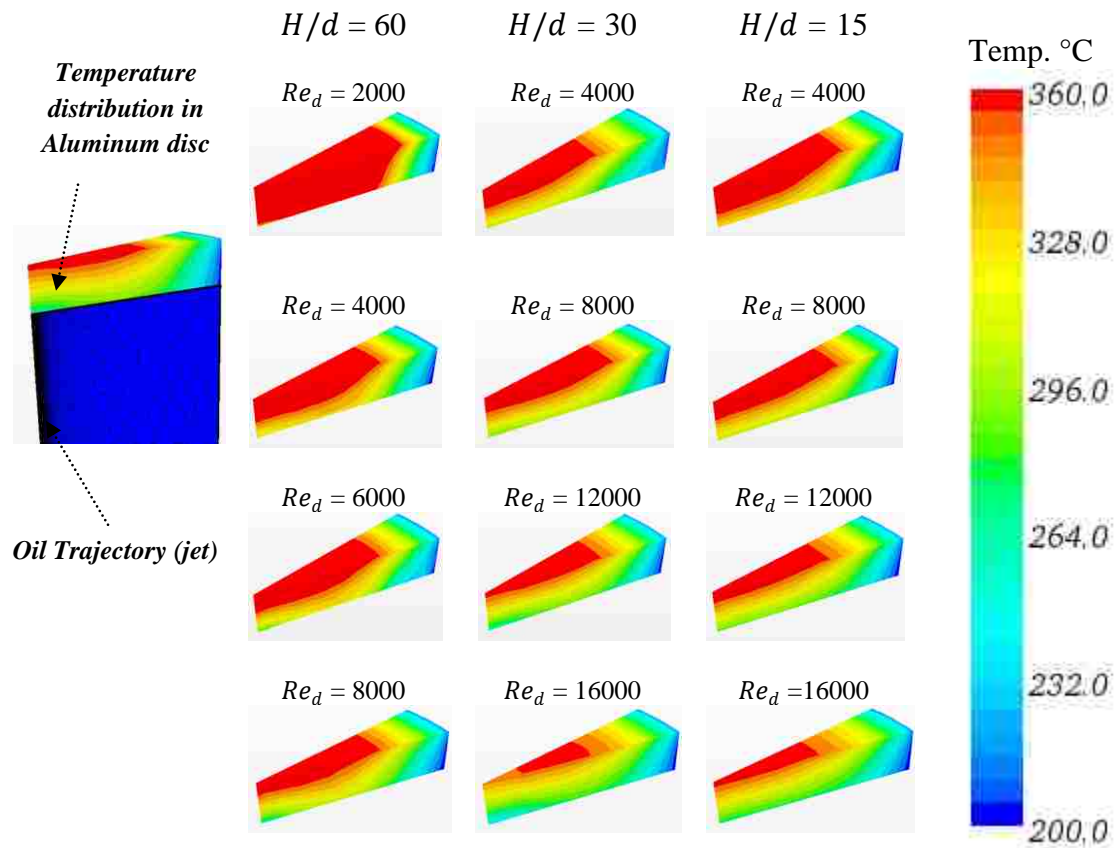


Figure 4.17: Contours of temperature for the constant heat flux disc, for different nozzle sizes and jet Reynolds numbers;  $H = 60$  mm

#### 4.6 Conclusions

A numerical study of a circular oil jet impinging on a flat disc with uniform wall heat flux was carried out using the volume of fluid method. A fully-developed turbulent pipe flow profile was employed at the exit of the nozzle. Large jet length-to-nozzle diameter ratios ( $10 \leq H/d \leq 80$ ) were considered in this study. The conclusions can be summarized as follow:

- The radial extent of the stagnation region beneath the jet is not uniform, but is a function of the radial velocity gradient  $\partial u_r / \partial r$  in this region.
- A correlation describing the stagnation zone Nusselt number has been developed, applicable over a wide range of Reynolds numbers and Prandtl numbers. This correlation is expressed in terms of Reynolds number, Prandtl number and a non-dimensional radial velocity gradient. It does not explicitly depend on the nozzle-to-target spacing since it is applicable only for long jets, i.e.,  $H/d > 10.0$ .
- The normalized local Nusselt number varies weakly with Reynolds number for a specific nozzle size. It can be approximately considered to be a function of  $r/d$  only.
- The local Nusselt number decreases in a narrow strip around the stagnation point, when the velocity gradient falls below a specific value. It then increases to its maximum value within the stagnation zone before monotonically decreasing out to the edge of the disc.
- For a given Reynolds number, the temperature distribution on the impinging surface will be more uniform for larger nozzles compared to smaller nozzles. Smaller nozzles provide more efficient cooling at the stagnation region and subsequently lower temperature. Larger nozzles cool the surface more uniformly.
- For  $Re_d > 5000$ , the average temperature in the disc is independent of nozzle size and slightly dependent on Reynolds number. However, the actual temperature distribution does change with nozzle size.
- The effect of nozzle geometry on thermal characteristics is insignificant. The viscosity tends to eliminate the velocity gradient in the radial directions for long jets, which results in a constant velocity gradient at the stagnation point.



## CHAPTER 5

### HEAT TRANSFER DUE TO A CONFINED JET IMPINGING ON TO A MOVING DISC

#### 5.1 Introduction

In this chapter, a transient numerical investigation has been conducted to determine the thermal effects of an axisymmetric oil jet impinging on a high-speed reciprocating disc subjected to uniform heat flux and bounded by a cylindrical wall. The motion of the disc results in minimum and maximum impingement distances of 20 and 100 mm from the nozzle. Two angular velocities, 210 and 630 rad/s, are chosen to mimic the motion of the disc. The two-phase air-oil simulations are performed using the volume of fluid (VOF) method with a high-resolution interface capturing scheme. The three-dimensional Navier-Stokes equations and energy equation are numerically solved using a finite volume discretization. The conjugate heat transfer (CHT) method is used to obtain a coupled heat transfer solution between the disc and fluid, yielding a more accurate prediction for the heat transfer coefficient. To overcome the high computational cost of such a simulation, a new methodology is presented to accelerate the solution. The simulation process involves several stages, including the simulation of the heat transfer of a stationary disc with a cooling jet at different impingement distances from the nozzle exit and simulation of a moving disc without the cooling jet and subjected to constant heat flux. Following this, the flow field and thermal characteristics of a reciprocating disc with constant heat flux and an impinging cooling jet is considered.

In addition to the acceleration methodology, the other requirement of the transient simulation in this chapter is to find the appropriate time steps required to prevent jet

smearing and preserve the sharpness of the liquid-air interface. This requirement becomes more substantial if the simulation includes both heat transfer and a high-speed moving boundary. The appropriate time step will subsequently be used in the transient simulation of flow in a four-cylinder engine geometry presented in the next chapter.

## 5.2 Model Setup and Boundary Conditions

The present numerical simulation is used to predict the thermal characteristics when an axisymmetric oil jet impinges onto a high-speed reciprocating aluminum disc with a thickness of 10 mm and placed in a cylindrically confined space. The computational domain with relevant thermal boundary conditions is shown in Figure 5.1. The parameters used in the simulation are summarized in Table 5.1.

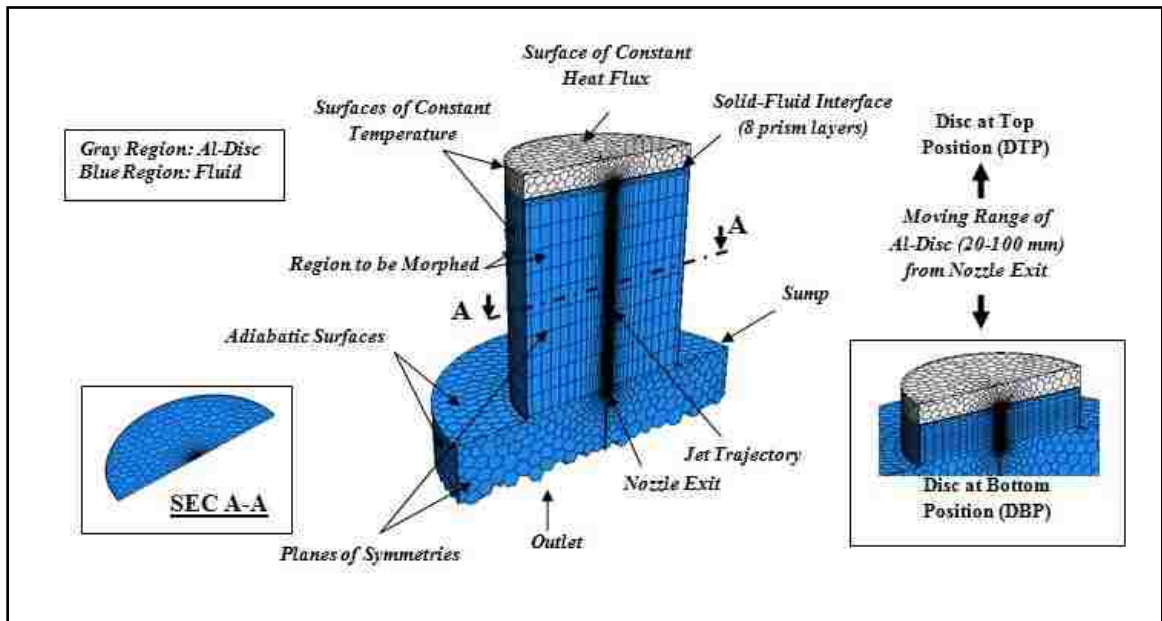


Figure 5.1: Computational domain and relevant thermal boundary conditions

---

Disc diameter ( $D$ )	90 mm
Disc thickness	10 mm
Oil temperature at nozzle exit ( $T_f$ )	130°C
Circumferential disc surfaces temperature	130°C
Confined cylinder surface temperature	130°C
Sump surface thermal condition	adiabatic
Diameter of fully-developed pipe type nozzle ( $d$ )	1.0 mm
Bulk velocity of the nozzle exit ( $v_f$ )	30 m/s
Density of air ( $\rho_{air}$ )	Ideal gas
Dynamic viscosity of air ( $\mu_{air}$ )*	Sutherland's law
Air thermal conductivity ( $k_{air}$ )	Sutherland's law
Specific heat of air ( $c_{p-air}$ )	polynomial in $T$
Density of oil ( $\rho_{oil}$ )*	822 kg/m <sup>3</sup>
Dynamic viscosity of oil ( $\mu_{oil}$ )*	8.424 x 10 <sup>-3</sup> kg/m.s
Specific heat of oil ( $c_{p-oil}$ )*	2350 J/kg.K
Oil thermal conductivity ( $k_{oil}$ )*	0.134 W/m.K
Prandtl number of oil ( $Pr_{oil}$ )*	145
Density of Aluminum ( $\rho_{Al}$ )	2700 kg/m <sup>3</sup>
Specific heat of Aluminum ( $c_{p-Al}$ )	903 J/kg.K
Aluminum thermal conductivity ( $k_{Al}$ )	237 W/m.K
Heat flux at disc top surface	50 kW/m <sup>2</sup>

---

\* Parameters evaluated at nozzle exit condition, i.e., 130°C

Table 5.1: Input parameters for current numerical simulation

The generic model with relevant boundary conditions, meshing scheme, turbulence model and solution algorithm that were presented in Chapter 4 are used here again with the following differences:

- In the simulation of the moving disc, a piston motion equation to produce a reciprocating motion is used to model the movement of the aluminum disc. Two angular velocities of 210 and 630 rad/s are chosen. The relative velocity between the jet and disc is between 20 to 40 m/s during the cycle with the angular velocity of 210 rad/s, and between 2 to 56 m/s during the cycle with angular velocity of 630 rad/s (Figure 5.2). The linear displacement of the aluminum disc in the computational domain corresponds to impingement distances of 20 to 100 mm from the nozzle exit as shown in Figure 5.1. The physical time for one cycle (360°) is 0.03 and 0.01 s,

corresponding to the two angular velocities. The time steps in the current simulation are  $\Delta t = 1.0 \times 10^{-6}$  s (for 210 rad/s) and  $3.3 \times 10^{-7}$  s (for 630 rad/s) with twenty internal iterations. The computational time step is small enough to accurately capture the physics of the process. The maximum Courant number over the cycle is less than 1.0 for both cases, which satisfies the CFL condition discussed in Chapter 3.

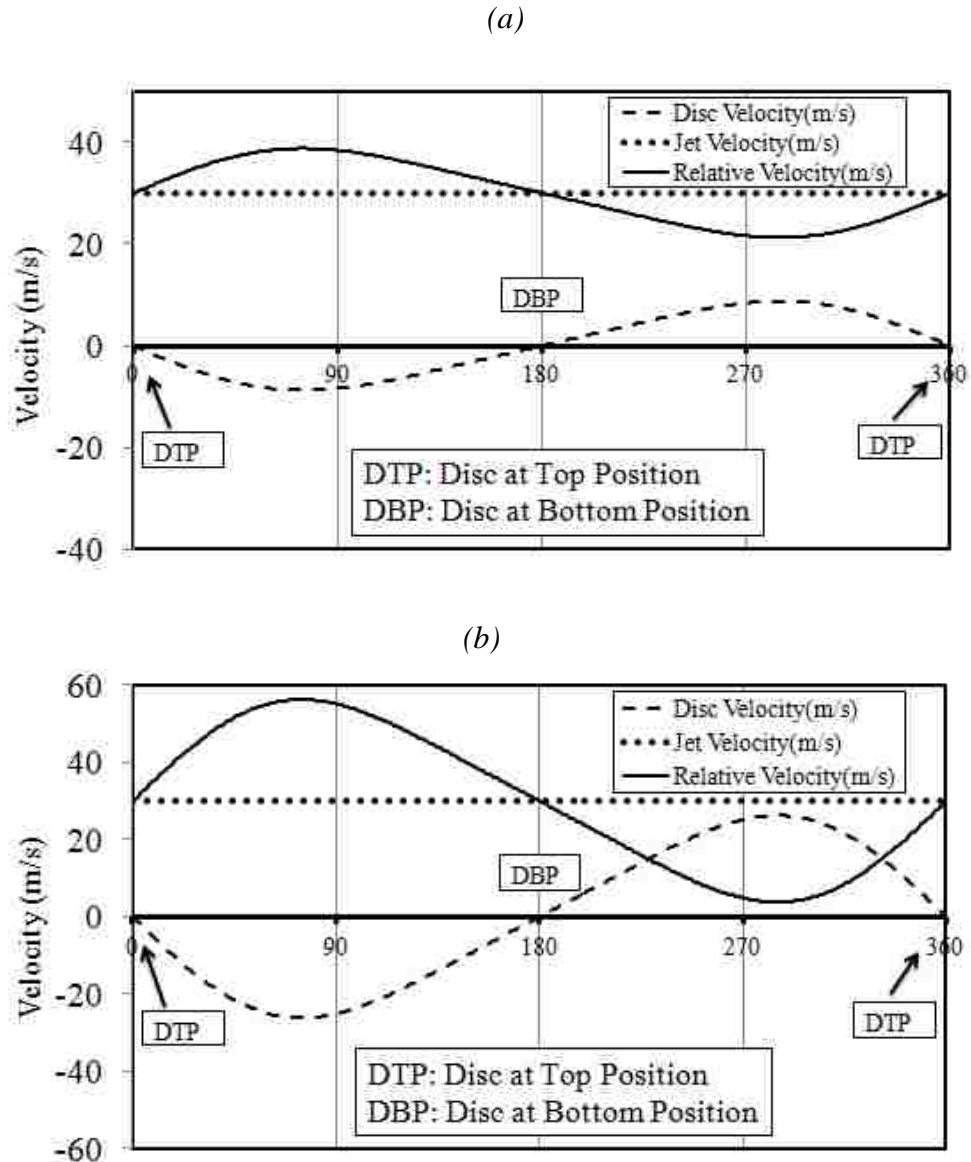


Figure 5.2: Motion profile over one cycle for two angular velocities of the disc; (a)

210 rad/s, (b) 630 rad/s

- Unlike the jet impingement onto a stationary disc, where a  $(1/20)^{\text{th}}$  wedge segment of the entire geometry was used as the computational domain, a larger domain corresponding to half of the entire geometry is used (see Figure 5.1). Difficulties arose while simulating the moving disc using a 1/20-wedge segment; the fine cells at the sharp edge of the wedge disintegrate due to the morphing process and cause a computational error. The plane symmetric boundary with a half portion of the entire geometry prevents the disintegration of the cells. The morphing motion redistributes mesh vertices in response to the movement of control points. The mesh morpher uses control points and their associated displacements to generate an interpolation field throughout the region, which can then be used to displace the actual vertices of the mesh. Each control point has an associated distance vector, which specifies the displacement of the point within a single time step (STAR-CCM + Manual, 2012).
- Simulation of jet impingement onto a moving disc is very expensive in term of CPU time, therefore only one nozzle size is considered with the earlier defined angular velocities. In the current transient simulation, a smooth pipe nozzle with 1.0 mm diameter is used to produce a fully-developed turbulent pipe flow profile, which is implemented as an inlet boundary condition to the computational domain. The Reynolds number of the issuing jet lies in the turbulent regime ( $Re_d \approx 3000$ ).
- The top surface of the 90 mm diameter disc is subjected to uniform heat flux of  $q'' = 50 \text{ kW/m}^2$  instead of  $270 \text{ kW/m}^2$  (Agarwal et al., 2011). The convective heat transfer coefficient is evaluated based on specific bulk or reference temperature, i.e.,  $T_{ref} = 130^\circ\text{C}$  (similar to the jet impingement onto a stationary disc).

- The value of  $y^+$  for jet impingement onto a moving disc is less than 3.5 at the solid-fluid interface for both angular velocities and over the entire cycle.

### 5.3 Results and Discussion

The transient simulation of jet impingement heat transfer on a high-speed moving boundary is a computationally expensive process. Preliminary simulations indicated that even with 48 CPUs, a very long time would be required to effectively simulate the process and achieve a steady temperature distribution in the disc. This distribution is referred to as “steady” since it will not change significantly during the cycle because the time scale of the heat transfer from the disc is very large compared with the time scale of the problem itself (i.e., cycle duration).

For practical implementation in an industrial environment, it is essential to develop a methodology to accelerate the solution. To this end, the fluid-solid interface is split into nine regions, as shown in Figure 5.3.

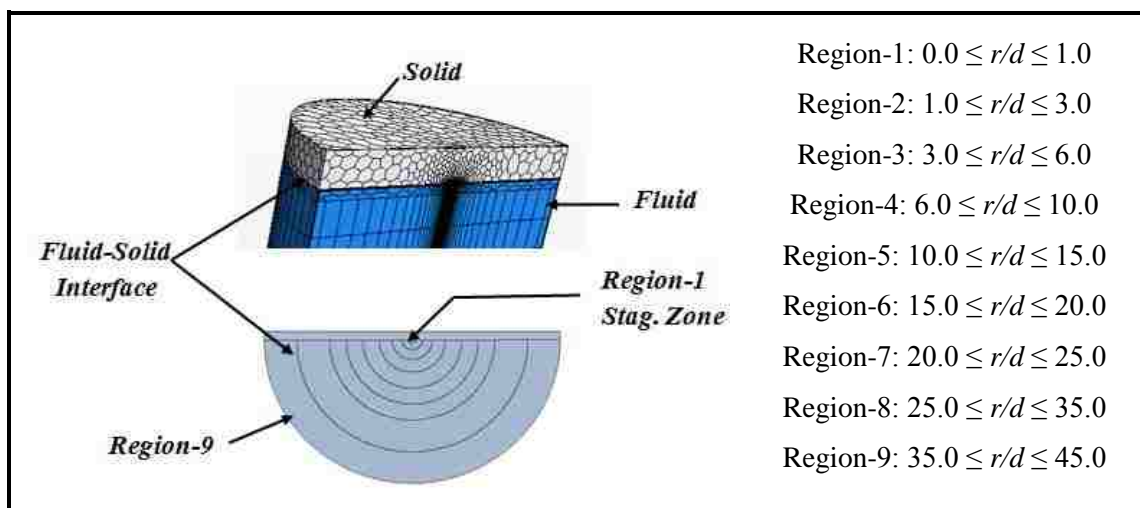


Figure 5.3: Delineation of the nine regions at the fluid-solid interface

In Figure 5.3, Region-1 represents approximately the stagnation region due to jet impingement, while Region-9 represents the outer peripheral region of the disc. In the stagnation region or stagnation zone, a very thin viscous layer is formed which exhibits little resistance to the heat flow.

In this section, the computational results from the simulation without and with jet impingement are discussed. A methodology to accelerate the computational solution for the case of jet impingement is also presented.

### **5.3.1 Moving Boundary without Jet**

In order to evaluate the effectiveness of the jet cooling process, computational results of jet impingement heat transfer should be compared with some non-cooled reference data. Therefore, simulations were first carried out to evaluate the thermal characteristics in the absence of the cooling jet. The results from these simulations are used as a benchmark for comparison purposes. Figure 5.4 shows the final steady temperature distribution in the disc at two angular velocities, i.e., 210 and 630 rad/s. It is obvious from Figure 5.4 that angular velocity has a negligible effect on the temperature distribution in the absence of the cooling jet. In both cases, the maximum surface temperatures are very similar ( $\sim 210$  °C) and occur at the centre of the disc.

The surface average heat transfer coefficients and corresponding Nusselt numbers (averaged over one cycle) are shown in Table 5.2 for the nine regions defined in Figure 5.3. It is obvious from Table 5.2 that the overall surface average heat transfer coefficient increases by 140% at 630 rad/s in comparison with that at 210 rad/s. However, even at

the higher angular velocity, the heat transfer coefficient at the fluid-solid interface remains insignificant.

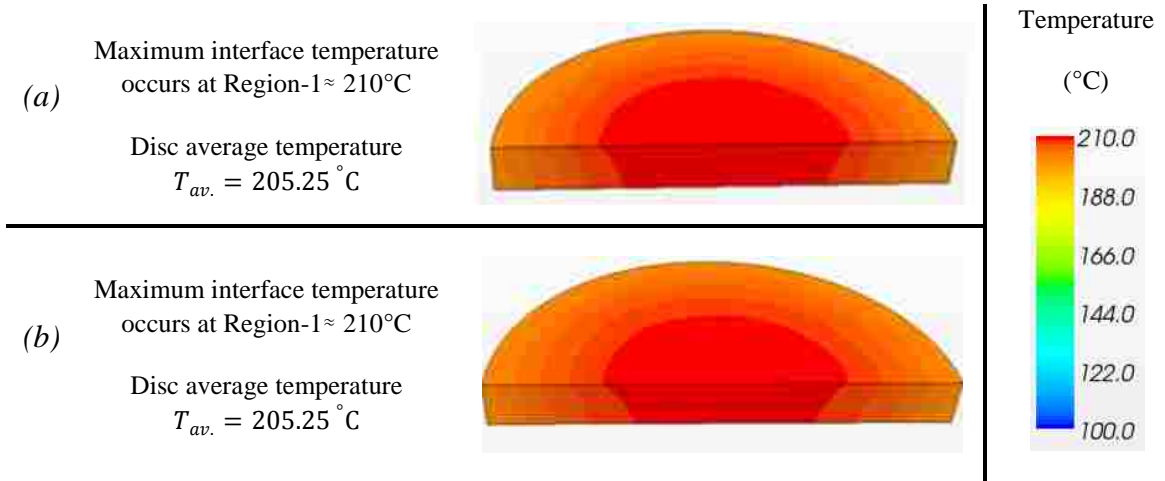


Figure 5.4: Temperature profile in the disc without cooling jet;

(a)  $\omega = 210$  rad/s, (b)  $\omega = 630$  rad/s

(a)

(b)

Region No.	$Nu$	HTC ( $W/m^2.K$ )	Region No.	$Nu$	HTC ( $W/m^2.K$ )
Region-1	0.15	20	Region-1	0.33	43
Region-2	0.17	22	Region-2	0.36	48
Region-3	0.19	25	Region-3	0.38	51
Region-4	0.19	25	Region-4	0.35	47
Region-5	0.17	23	Region-5	0.31	42
Region-6	0.16	22	Region-6	0.31	41
Region-7	0.15	21	Region-7	0.31	42
Region-8	0.13	18	Region-8	0.24	32
Region-9	0.26	35	Region-9	0.44	59
Total Interface Average	0.14	19	Total Interface Average	0.34	46

Table 5.2: Surface average Nusselt number (averaged over one cycle) at solid-fluid

interface without jet cooling, (a)  $\omega = 210$  rad/s, (b)  $\omega = 630$  rad/s



Additional insight into the flow characteristics influencing the heat transfer can be obtained by extracting the contours of the average radial velocity along the interface (averaged over an entire cycle) as shown in Figure 5.5. It is evident from this figure and Table 5.2 that the maximum heat transfer coefficient occurs at the fluid-solid interface immediately adjacent to the cylindrical side wall (Region-9). It can be concluded from this figure that the heat transfer coefficient strongly depends on the fluid velocity parallel to the solid-fluid interface, i.e., the radial velocity.

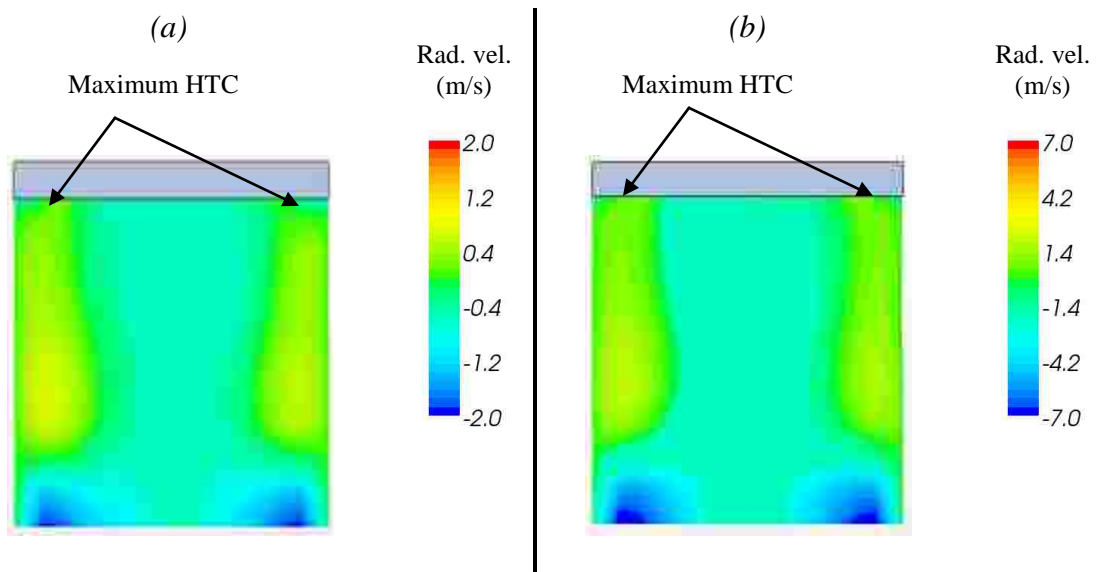


Figure 5.5: Contours of mean radial velocity averaged over one cycle;

(a)  $\omega = 210$  rad/s, (b)  $\omega = 630$  rad/s

### 5.3.2 Moving Boundary with Jet

The present study is concerned with heat transfer as a consequence of jet impingement on a disc in a highly turbulent surrounding. This chaotic surrounding ensues as a result of the high reciprocating motion of the disc. In the present study, the maximum radial (crossflow) velocity components during the cycle is found to be 7.0 m/s, yielding a maximum crossflow Weber number of less than 3 for  $\omega = 630$  rad/s. This velocity component will deflect the oil jet slightly (see section 2.5.2 in Chapter 2). A proper understanding can be gained by extracting the volume fraction contours at the location where the jet deformation is expected, as shown in Figure 5.6. As the disc starts moving upwards to its top position, the relative velocity between the jet and disc begins to approach zero (see Figure 5.2). The negative pressure inside the cylinder will draw in the air and enhance the radial or crossflow component. The momentum flux ratio defined by equation (2.20) decreases as the disc moves upwards, helping to deflect or stretch the jet radially. On the contrary, as the disc moves downwards towards its bottom position or when the disc is moving with lower velocities, the momentum flux ratio increases and the jet remains intact and no sign of deformation occurs.

One of the main requirements in the transient simulation of multiphase flow is the need for a small time step to prevent the smearing associated with numerical diffusion and preserve the sharpness of the liquid-air interface. This requirement becomes more significant if the simulation includes both heat transfer and a high-speed moving boundary. In the current simulation, the appropriate time steps required to prevent jet smearing and preserve the sharpness are found to be  $1.0 \times 10^{-6}$  s and  $3.3 \times 10^{-7}$  s for angular velocities 210 rad/s and 630 rad/s, respectively. At these time steps, about 3000 CPU

hours are required to complete the simulation of one cycle. Therefore, the physical time required to obtain the final temperature distribution in the disc is significant, especially if the initial temperature distribution (initial guess value) in the disc is far from the final distribution. Therefore, we propose a methodology to expedite the solution and reduce the computational cost.

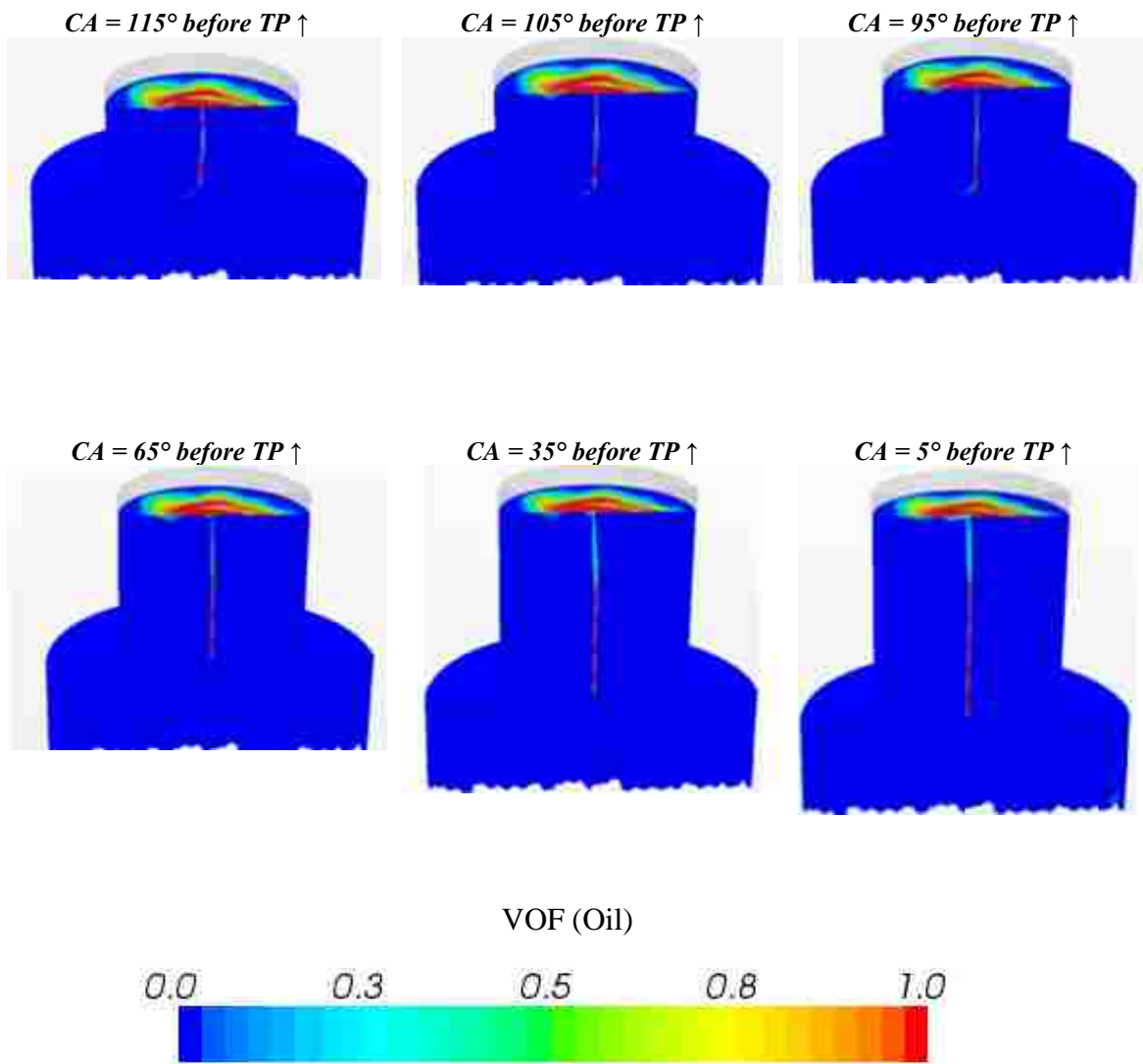


Figure 5.6: Evolution of liquid jet as disc moves towards its top position (TP),

$$\omega = 630 \text{ rad/s}$$

### 5.3.2.1 Initial Estimate of the Temperature Profile

The initial estimate of the temperature profile is very crucial in terms of reducing the CPU time in simulations when the energy equation has been activated. Steady-state simulations were first carried out for the oil jet impinging onto a stationary boundary to estimate the initial temperature distribution for the transient simulation. Two steady-state simulations were performed, one with the disc at its farthest location, i.e., 100 mm from the nozzle exit, and one with the disc at its closest location, i.e., 20 mm from the nozzle exit. In these stationary disc situations, the relative velocity is purely the jet velocity. The temperature profile in the disc for both cases is shown in Figure 5.7.

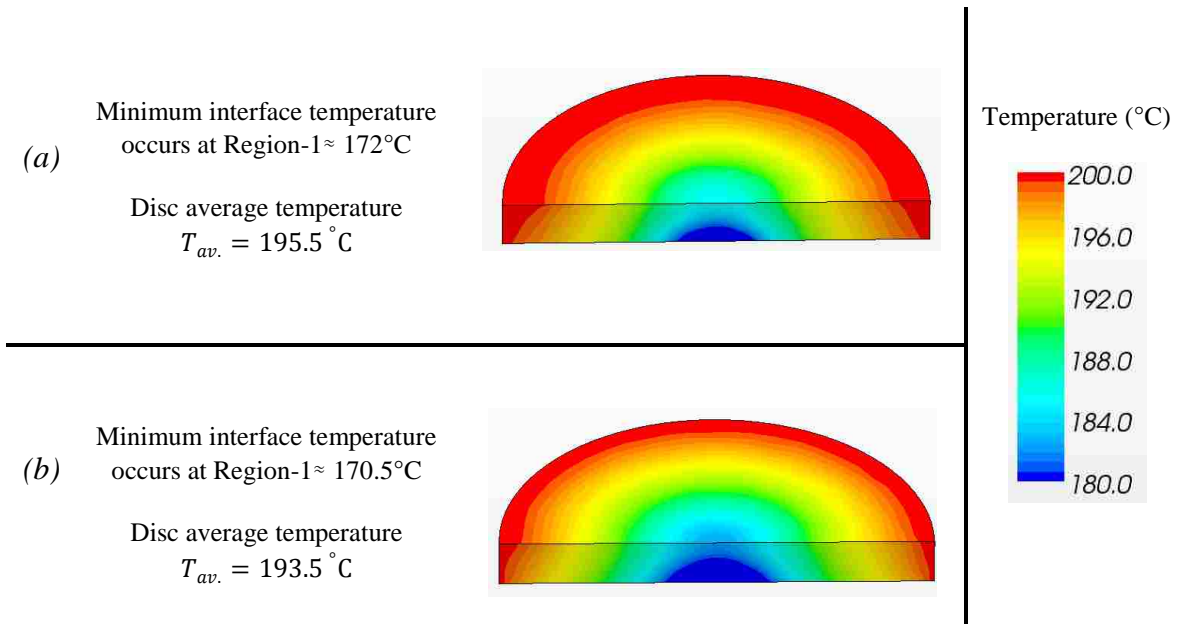


Figure 5.7: Steady-state temperature profile for stationary disc with cooling jet, at two elevations from the nozzle exit: (a)  $H/d = 20$ , (b)  $H/d = 100$

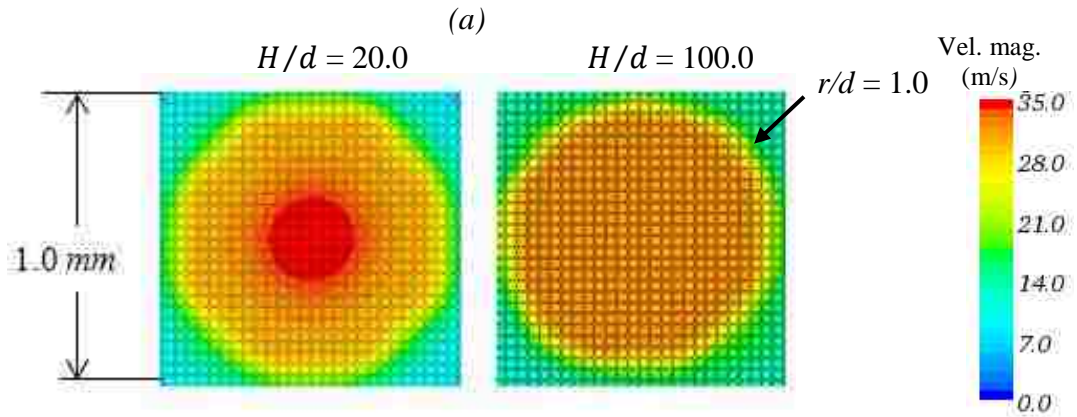
The surface average heat transfer coefficients and corresponding Nusselt numbers for these cases are given in Table 5.3. As shown in the table, the maximum Nusselt numbers occur at the centre of the disc, where the minimum temperature is expected. The minimum heat transfer coefficient and consequently the maximum temperature are observed at the outer edge of the disc. It is evident from Table 5.3 that the stagnation zone Nusselt number is 7.0% higher with the shorter impingement distance. However, the overall surface average Nusselt number is 30.0% higher with the larger impingement distance.

(a)			(b)		
Region No.	$Nu$	HTC (W/m <sup>2</sup> .K)	Region No.	$Nu$	HTC (W/m <sup>2</sup> .K)
Region-1	151.0	20204	Region-1	140.0	18732
Region-2	109.5	14651	Region-2	106.0	14183
Region-3	77.0	10303	Region-3	76.0	10169
Region-4	48.0	6422	Region-4	48.0	6422
Region-5	20.5	2743	Region-5	22.0	2944
Region-6	10.5	1405	Region-6	13.0	1739
Region-7	6.0	803	Region-7	9.5	1271
Region-8	4.0	535	Region-8	7.5	1004
Region-9	2.0	268	Region-9	4.5	602
Average	8.0	1070	Average	10.5	1405

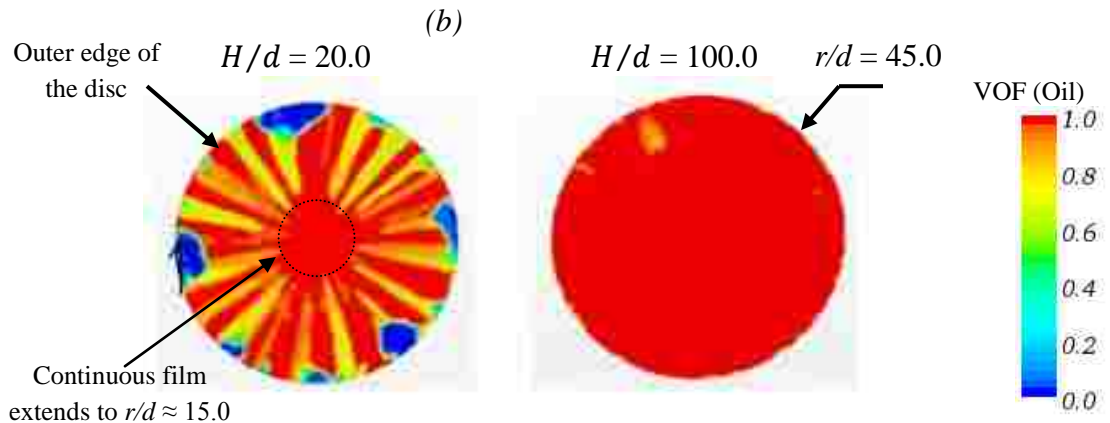
Table 5.3: Surface average Nusselt number at solid-fluid interface, at two elevations from the nozzle exit; (a)  $H/d = 20$ , (b)  $H/d = 100$

A proper understanding of the Nusselt number distribution can be gained by examining the flow characteristics before the impinging point and at the solid-fluid interface as shown in Figure 5.8. It has been postulated that viscosity diffuses the velocity profile towards a uniform profile in a longer jet (Lienhard, 2006). In the current study,

one would expect the velocity profile near the impinging point to be uniform with the longer jet, as corroborated in Figure 5.8a (see also section 5.7 in Chapter 4).



Horizontal section through liquid jet (velocity magnitude)



Solid-fluid interface (VOF)

Figure 5.8: (a) Horizontal section through liquid jet, at 2.0 mm before impinging point (velocity magnitude), (b) Solid-fluid interface (VOF)

For both jets, the oil film is homogeneous and continues up to  $r/d = 10.0$  (see Figure 5.8b), which results in a comparable heat transfer coefficient for short and long jets

within the first five consecutive inner regions as shown in Table 5.3. However, at the stagnation zone, one can notice a higher value of heat transfer coefficient in the case of the shorter jet, which can be attributed to the velocity profile (see cross-sectional contours in Figure 5.8a). This velocity profile results in higher radial velocity gradient at the impinging point and consequently higher heat transfer coefficient in the 20.0 mm long jet. Beyond  $r/d = 10.0$ , the oil film develops in a streaky pattern with the short jet.

Table 5.4 shows the comparison of stagnation zone Nusselt number from the current simulation (Region-1 in Table 5.3) with the results from equation (2.40) and equation (4.2). This comparison provides validation for the procedure used in the present simulation, further to the validation process demonstrated in Chapter 4 for jet impingement onto a stationary disc.

Disc location	$Nu_o$ - current simulation	$Nu_o$ - eqn. (4.2)	$Nu_o$ - eqn. (2.40)
Bottom Position 20 mm from nozzle exit	<b>151</b>	147	140
Top Position 100 mm from nozzle exit	<b>140</b>	147	145

Table 5.4: Comparison of computed  $Nu_o$  with the results from equations (4.2) and (2.40)

Finally, to initialize the temperature for the transient simulation, a single averaged value of heat transfer coefficient for each region defined in Figure 5.3 is calculated from Table 5.3. These values are used as boundary conditions to simulate the steady-state heat conduction inside the solid disc (no fluid domain is considered at this stage) and to approximate the initial temperature distribution inside the solid disc for the transient simulation of the entire domain (fluid and solid).

### 5.3.2.2 Nusselt Number Profile

The surface average heat transfer coefficient as a function of time for each region defined in Figure 5.3 is obtained using a two-phase flow transient simulation. One of the requirements of such simulations is that the time step must be very small; therefore, this is the most expensive stage in the solution procedure. The simulation is carried out for 40-50 cycles for the two angular velocities to extract the cyclic profile of the Nusselt number, as shown in Figure 5.9 (just the last five cycles are shown in this figure). This regular cyclic behaviour cannot be obtained if the solid disc is initialized randomly or at a constant temperature.

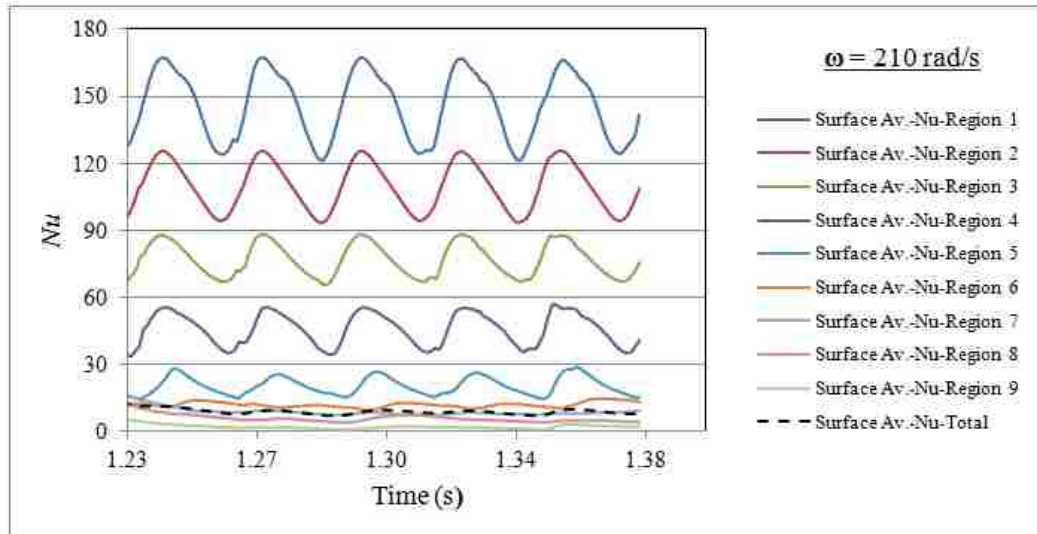
The transient Nusselt number is averaged from the recurring cycles in Figure 5.9 to obtain one average cycle Nusselt number for each region at the fluid-solid interface as shown in Figure 5.10. It is worthwhile to mention that the Nusselt number has a significant value in the regions 1 to 3, i.e.,  $0.0 \leq r/d \leq 6.0$ . As illustrated in Figure 5.10, the profiles of the transient Nusselt number for  $\omega = 210$  rad/s, where the disc-jet relative velocity ranges from 20 to 40 m/s, are smoother compared to  $\omega = 630$  rad/s, where the disc-jet relative velocity ranges from 2 to 56 m/s. One should recall that the disc-jet relative velocity is close to zero during about one-quarter of the cycle for angular velocity 630 rad/s. The irregular Nusselt number profile at  $\omega = 630$  rad/s can be attributed to the low magnitude and large variation in the relative velocity.

The maximum disc-jet relative velocity in Figure 5.10 leads the maximum Nusselt number in the regions at the fluid-solid interface. The phase shift between the two maxima increases as one moves radially away from the stagnation point. The occurrence of maximum HTC lags the turning process by a few degrees. Upon impingement, the



flow turns and enters the wall jet region where the flow moves radially outwards parallel to the disc.

(a)



(b)

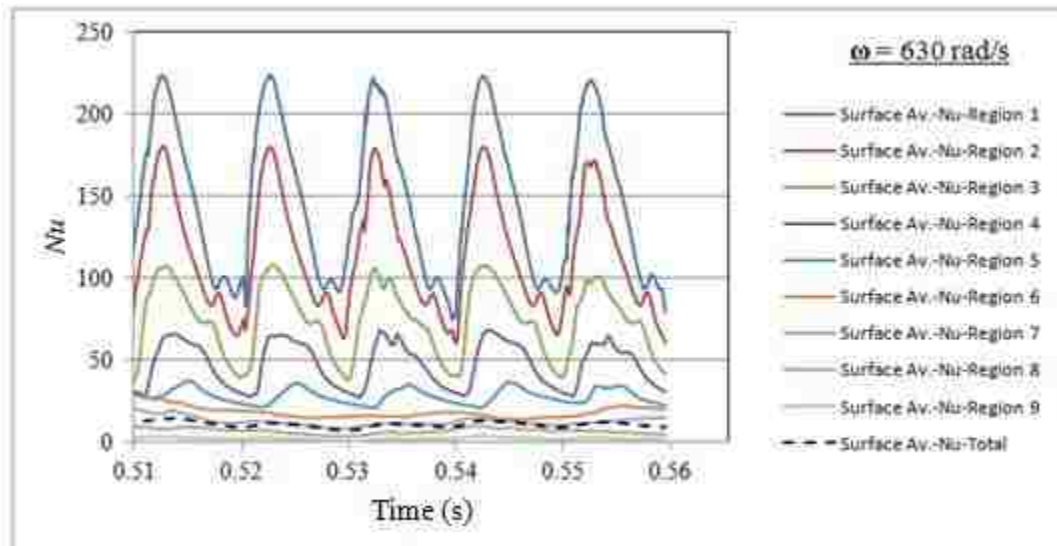


Figure 5.9: Surface (solid-fluid interface) average transient Nusselt number with cooling jet; (a)  $\omega = 210 \text{ rad/s}$ , (b)  $\omega = 630 \text{ rad/s}$

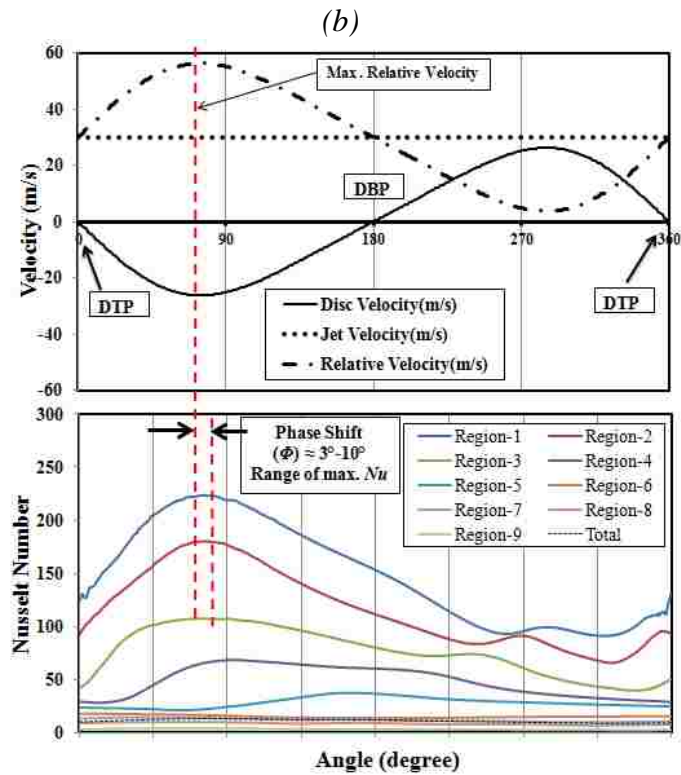
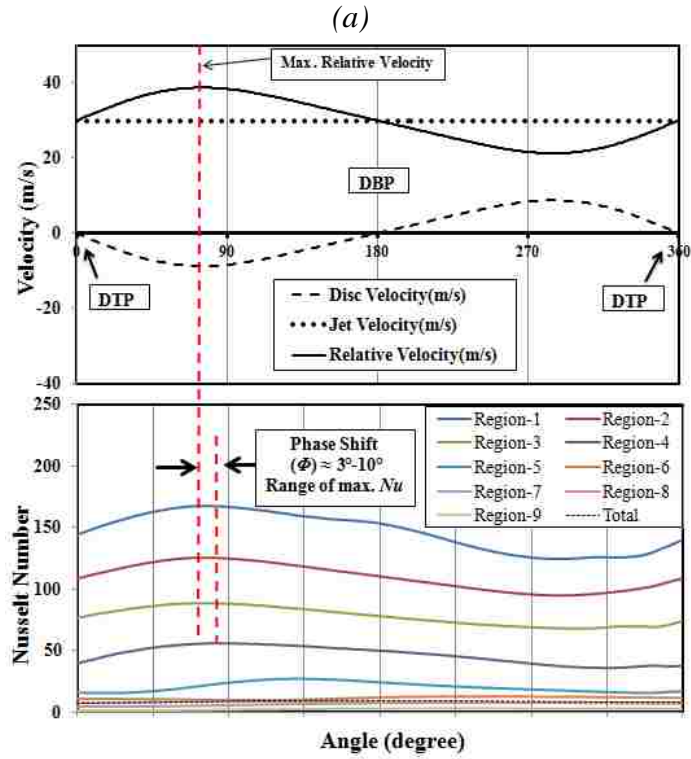


Figure 5.10: Nusselt number profile (one cycle) obtained from average of recurring cycles in Figure 5.9; (a)  $\omega = 210$  rad/s, (b)  $\omega = 630$  rad/s

A proper understanding of the phenomenon that creates this lag can be attained by extracting the contours of volume fraction and radial velocity gradient at the wall jet region immediately underneath the fluid-solid interface. As shown in Figure 5.11, two distinct regions can be identified; the accelerating region where the radial velocity gradient is positive, and the decelerating region where the radial velocity gradient is negative. The region around the stagnation point, referred to as the stagnation zone, extends to approximately  $r/d = 0.9$  in the current simulation. The stagnation zone plays the role of a heat sink where the maximum heat transfer coefficient is expected due to the jet impingement. It is evident from the figure that the stagnation zone region extends up to the interface between the positive and negative gradients, i.e., up to the location where the contour of positive radial velocity detaches from the solid wall (see also section 4.5.1 in Chapter 4).

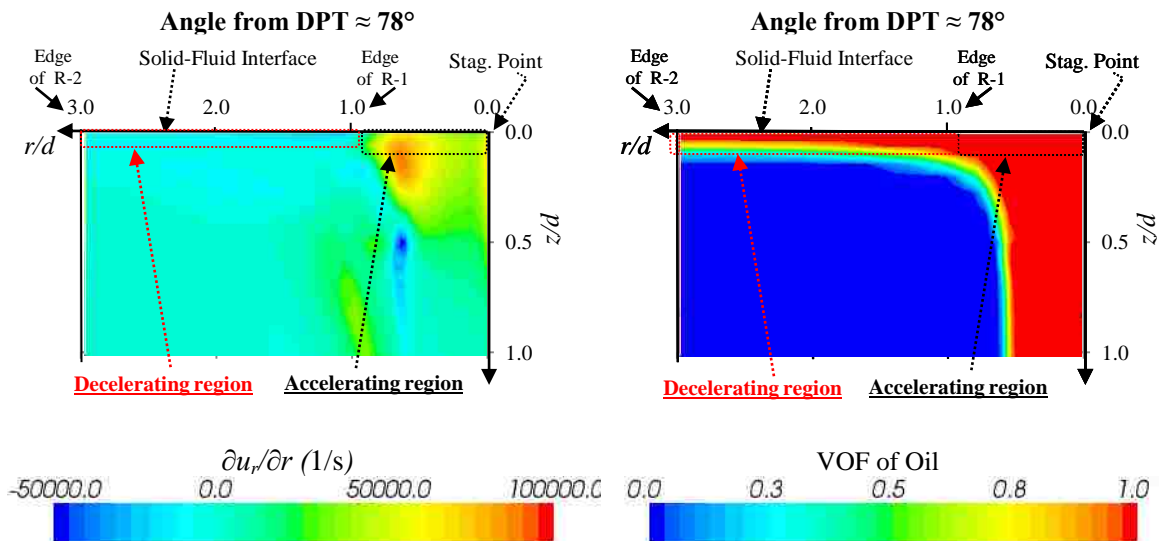


Figure 5.11: Contours of radial velocity and volume fraction of oil adjacent to the solid-fluid interface for two inner regions defined in Figure 5.3 ( $\omega = 630$  rad/s)

The heat transfer coefficient is strongly dependent on the radial velocity gradient adjacent to the wall (Vader, 1991; Donaldson & Snedeker, 1971). Table 5.5 shows the angular position of occurrence of the maximum radial velocity gradient (positive value) and the corresponding Nusselt number with respect to the relative velocity between the jet and the moving disc for Region-1, and similarly for the minimum radial velocity gradient (negative values) and corresponding Nusselt numbers for Region-2 and Region-3. The radial velocity gradient over the range  $0.0 \leq r/d \leq 6.0$  for the angular velocity 630 rad/s is displayed in this table. The maximum disc-jet relative velocity occurs after approximately  $74^\circ$  from the disc at its top position. The maximum Nusselt number corresponding to maximum radial velocity gradient in Region-1 and minimum velocity gradients in Region-2 and Region-3 occur at  $78^\circ$ ,  $80^\circ$  and  $82^\circ$ , respectively. These maximum values are marked in bold in Table 5.5.

Angle after disc @ top position (deg.) (relative velocity m/s)	Region-1(Stag. Region) $0.0 < r/d < 1.0$		Region-2 $1.0 < r/d < 3.0$		Region-3 $3.0 < r/d < 6.0$	
	Max. $(\partial u_r / \partial r)_{r \rightarrow 0}$	$Nu_o$	Min. $(\partial u_r / \partial r)$	$Nu$	Min. $(\partial u_r / \partial r)$	$Nu$
Max. rel. vel. $74^\circ(54.94)$	$9.59 \times 10^4$	222.0	$-2.40 \times 10^4$	174.5	$-2.55 \times 10^4$	102.6
$76^\circ(54.93)$	$9.64 \times 10^4$	222.0	$-2.38 \times 10^4$	175.7	$-2.00 \times 10^4$	103.0
$78^\circ(54.88)$	<b><math>9.70 \times 10^4</math></b>	<b>223.0</b>	$-2.35 \times 10^4$	176.0	$-1.44 \times 10^4$	104.0
$80^\circ(54.80)$	$9.62 \times 10^4$	222.5	$-2.33 \times 10^4$	176.8	$-1.13 \times 10^4$	104.7
$82^\circ(54.65)$	$9.40 \times 10^4$	222.0	<b><math>-2.25 \times 10^4</math></b>	<b>177.0</b>	$-1.05 \times 10^4$	105.0
$84^\circ(54.5)$	$9.00 \times 10^4$	221.5	$-2.37 \times 10^4$	176.5	<b><math>-1.03 \times 10^4</math></b>	<b>106.0</b>

Table 5.5: Angle of occurrence of the maximum  $Nu$  and corresponding velocity gradient  $\partial u_r / \partial r$  near the wall for the first three regions defined in Figure 5.3 ( $\omega = 630$  rad/s)

### 5.3.2.3 Disc Temperature Profile

The heat transfer coefficients evaluated from Figure 5.10 are used as boundary conditions for the nine regions to simulate the heat conduction inside the solid disc (no fluid domain). Since the Nusselt number profile is a function of time (or angle), a transient simulation is performed to evaluate the temperature profile in the disc. At this point, only one CPU is required to run the simulation. A constant temperature (194°C) was used to initialize the temperature in the disc. The simulations were carried out for 350 and 1000 cycles corresponding to the angular velocities of 210 and 630 rad/s, respectively. The criteria used to stop the simulation are such that the disc volume average temperature and the interface surface average temperatures for the nine regions do not change with physical time, as illustrated in Figure 5.12.

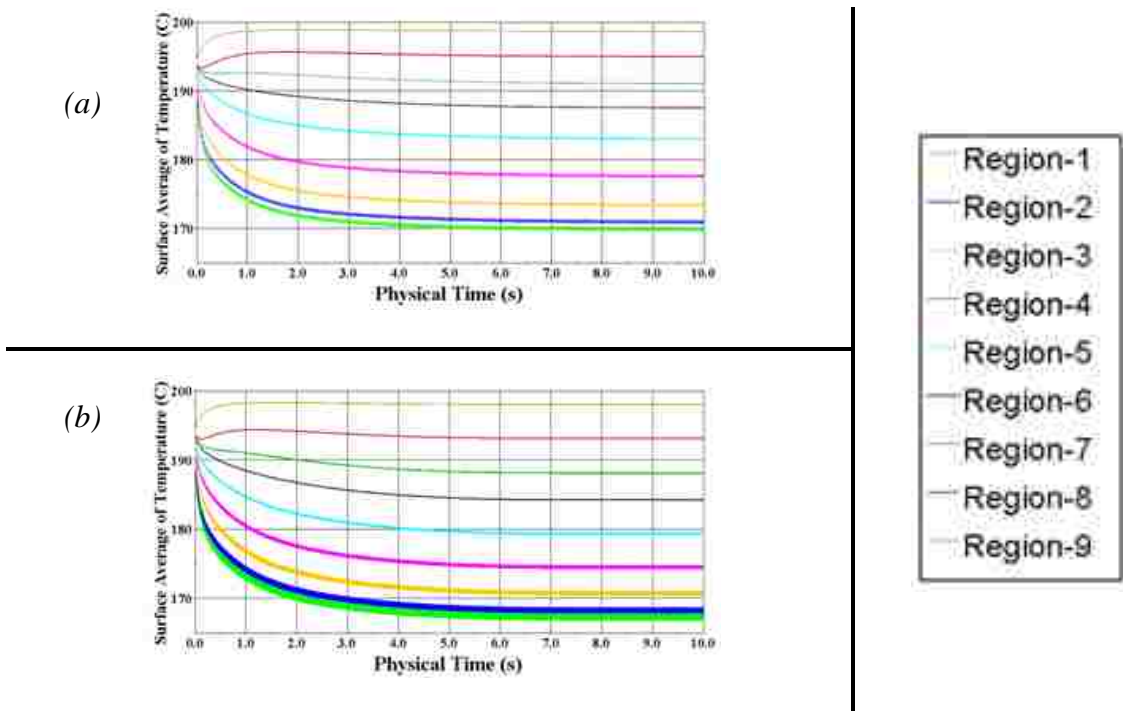


Figure 5.12: Evolution of surface average temperatures at fluid-solid interface with physical time; (a)  $\omega = 210$  rad/s, (b)  $\omega = 630$  rad/s

The final step in the acceleration process is to run the two-phase flow transient simulation for a few cycles using the entire computational domain (fluid and solid). The known temperature distribution from the transient heat conduction simulation is mapped onto the solid disc. The temperature distribution in the fluid region obtained from section 5.3.2.2 is mapped onto the fluid computational domain. The Nusselt number profiles from this simulation are very similar to those in Figure 5.9. The temperature profiles in the disc for both angular velocities are shown in Figure 5.13. The heat transfer coefficients and corresponding Nusselt numbers for the nine regions are provided in Table 5.6.

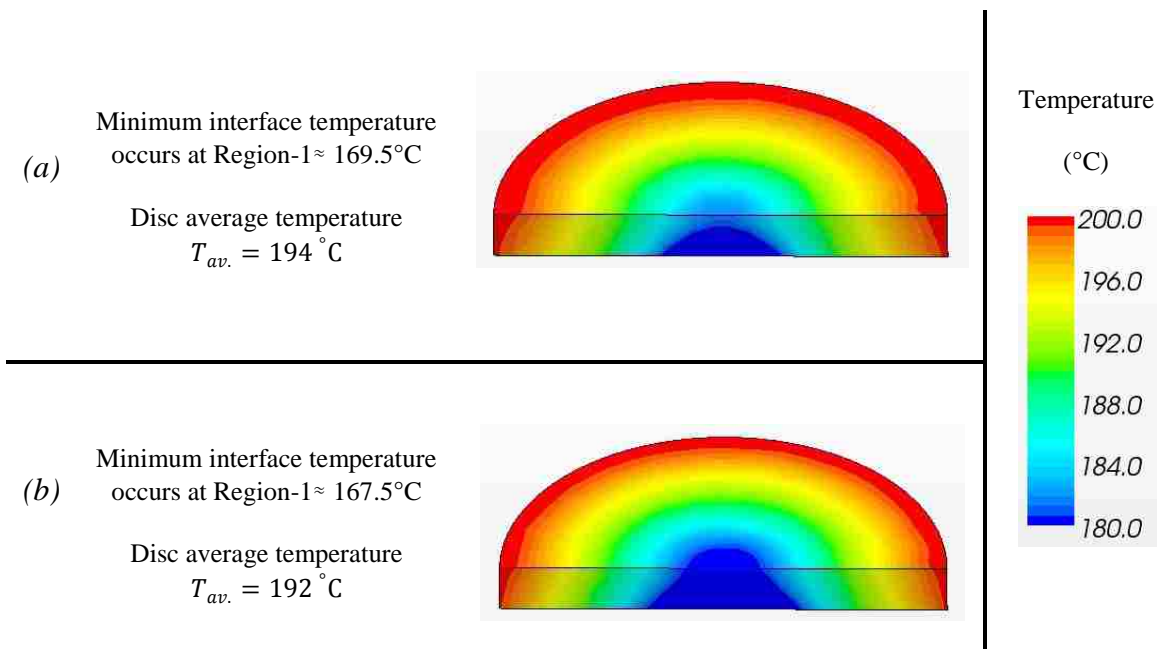


Figure 5.13: Final temperature distribution in the moving disc with the cooling jet;

(a)  $\omega = 210$  rad/s, (b)  $\omega = 630$  rad/s

(a)

Region No.	$Nu$	HTC (W/m <sup>2</sup> .K)
Region-1	146	19554
Region-2	109	14645
Region-3	77	10332
Region-4	46	6171
Region-5	20	2721
Region-6	11	1521
Region-7	8	1042
Region-8	7	876
Region-9	2	282
Average	9	1184

(b)

Region No.	$Nu$	HTC (W/m <sup>2</sup> .K)
Region-1	149	19908
Region-2	116	15560
Region-3	77	10279
Region-4	49	6531
Region-5	28	3802
Region-6	15	2027
Region-7	12	1652
Region-8	8	1109
Region-9	3	462
Average	11	1523

Table 5.6: Surface average Nusselt number (phase-averaged over one cycle) at solid-fluid interface with the cooling jet: (a)  $\omega = 210$  rad/s, (b)  $\omega = 630$  rad/s

Comparing the moving boundary with and without the cooling oil jet, the disc volume average temperature reduces by 6% and 5% corresponding to angular velocities of 210 and 630 rad/s, respectively. The surface average temperatures of the nine regions are summarized in Table 5.7. A number of observations can be drawn upon close examination of Table 5.7. First, the minimum surface average temperature occurs in the moving boundary with the cooling jet at an angular velocity of 630 rad/s. Although the jet-disc relative velocity is close to zero during one-quarter of the cycle, the high relative velocity during the rest of the cycle compensates for the lack in heat transfer coefficient and enhances the cooling efficiency. Second, a comparison between the moving boundaries without and with the cooling jet reveals a reduction in stagnation zone temperature by 19% and 20%, corresponding to the two angular velocities 210 and 630 rad/s, respectively. Third, for a fixed jet Reynolds number, the moving disc volume

average temperature and stagnation zone temperature are reduced by 1.0% and 1.5%, respectively, compared with the stationary disc. In light of the above, it appears that a steady-state simulation of an axisymmetric jet impinging onto a stationary disc will be an inexpensive approach to adequately predict the stagnation zone and volume average temperatures for an axisymmetric jet impinging onto a reciprocating moving boundary.

Boundary	Cooling	R-1	R-2	R-3	R-4	R-5	R-6	R-7	R-8	R-9	Interface Average
Stationary	Jet-20 mm $Re \approx 3000$	172°	173.5°	176°	179.5°	185°	189°	192°	196°	199°	194.5°
	Jet-100 mm $Re \approx 3000$	170.5°	171.5°	174°	177°	182°	186°	189°	193°	197.5°	192°
Moving 210 rad/s	No jet	210°	210°	210°	210°	209.5°	209°	208°	205.5°	202°	205°
Moving 630 rad/s	No jet	210°	209.5°	209.5°	209.5°	209°	208°	207°	205°	202°	205°
Moving 210 rad/s	Jet $Re \approx 3000$	169.5°	170.5°	173°	177°	183°	187.5°	191°	195°	198.5°	192.5°
Moving 630 rad/s	Jet $Re \approx 3000$	167.5°	168.5°	171°	174.5°	179°	184°	188°	193°	198°	190.5°

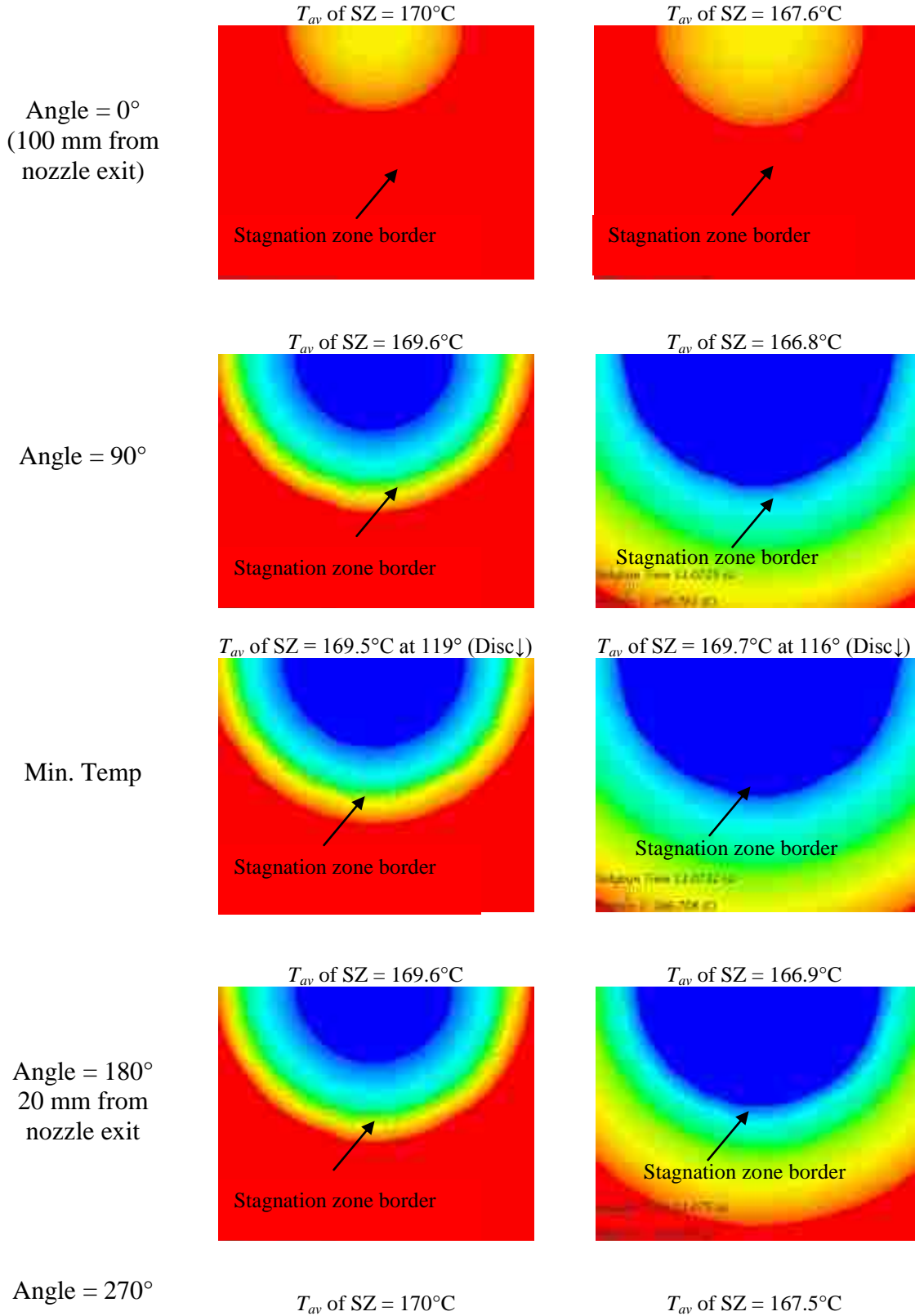
Table 5.7: Surface average of steady-state temperature for the regions defined in Figure 5.3

The temperature variations of the stagnation zone over the cycle were found to be 169.5° and 170.0°, and 166.7° and 167.7° corresponding to the angular velocities 210 and 630 rad/s, respectively. This minor variation may be attributed to the small time scale of the problem, i.e., 0.03 and 0.01 s corresponding to the two angular velocities in comparison with the time scale of the heat transfer from the disc. The variation of stagnation zone temperature over one cycle is shown in Figure 5.14.



$\omega = 210 \text{ rad/s}$   
Contours temp. level (169.5 - 170°C)

$\omega = 630 \text{ rad/s}$   
Contours temp. level (167 - 167.75°C)



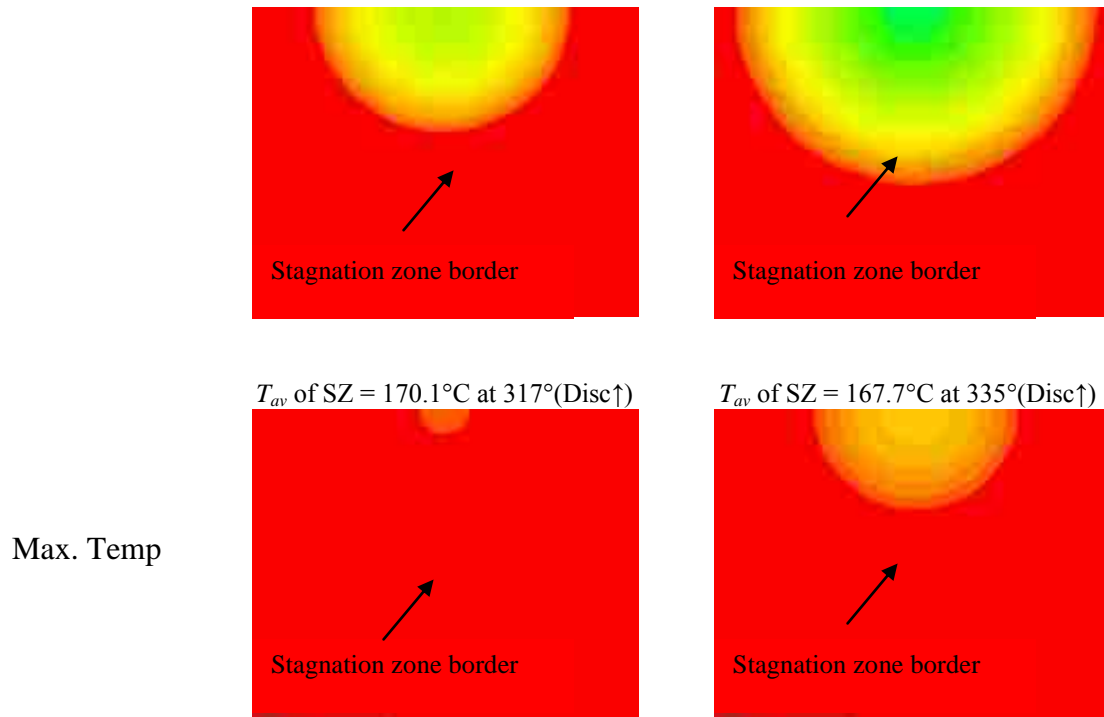


Figure 5.14: Evolution of temperature profile at stagnation zone region (Region-1) for angular velocities 210 rad/s and 630 rad/s

## 5.4 Conclusions

A transient numerical investigation was carried out to determine the thermal effects of a circular oil jet impinging onto a reciprocating disc subjected to a uniform wall heat flux using the volume of fluid (VOF) method. The conclusions from this study can be summarized as follow:

- Generally, transient simulations incorporating VOF, CHT and a high-speed moving boundary are expensive. A small time step is required to prevent smearing associated with numerical diffusion. In terms of CPU time, the simulations in the current study require about 3000 hours to complete one cycle (360°). The physical time required to

obtain the final temperature distribution in the disc is significant, and prohibitive for an industrial application.

- A methodology is presented to accelerate the solution process and reduce the cost in terms of CPU time, utilizing the cyclic profile of the transient Nusselt number. The cyclic profile of the transient Nusselt number only occurs when the temperature distribution in the disc is close to the final temperature distribution.
- Although the relative velocity between the jet and moving disc is close to zero for some period of time during the cycle in the case of higher angular velocity, the cooling is more efficient than at the lower angular velocity. The higher relative velocity between the disc and jet (during the rest of the cycle) compensates for the lower heat transfer coefficient and enhances the cooling efficiency.
- The maximum heat transfer coefficient due to jet impingement occurs in the region within the fluid film where the radial velocity gradient is positive. In other words, the stagnation region exists in the accelerating region around the stagnation point and extends up to the interface between the positive and negative velocity gradients in the liquid film adjacent to the wall.
- The maximum Nusselt number is attained a short time after the relative velocity between the disc and the jet reaches its maximum. The turning process of the jet after impingement lags the occurrence of maximum HTC by a few degrees.
- Once the temperature attains its final steady distribution in the disc, the temperature variation of the stagnation region and elsewhere in the disc is found to be insignificant over the cycle. This normally occurs when the problem time scale (i.e.,

cycle duration) is very small in comparison with the time scale of heat transfer from the disc.

- For industrial applications, it may be reasonable to perform a steady-state simulation to obtain a cost effective prediction of temperature distribution even when the disc has a reciprocating motion.

## CHAPTER 6

### SIMULATION OF PISTON COOLING USING OIL JETS

#### 6.1 Introduction

The aim of this chapter is to evaluate the piston cooling process using an oil jet in a full-scale engine. Transient simulation of Chrysler's full-scale 2.0 L Tigershark Inline 4-cylinder gasoline engine is carried out. The convective heat transfer coefficient distribution on the piston walls and the temperature contours in the pistons are computed to assess the oil jet cooling performance.

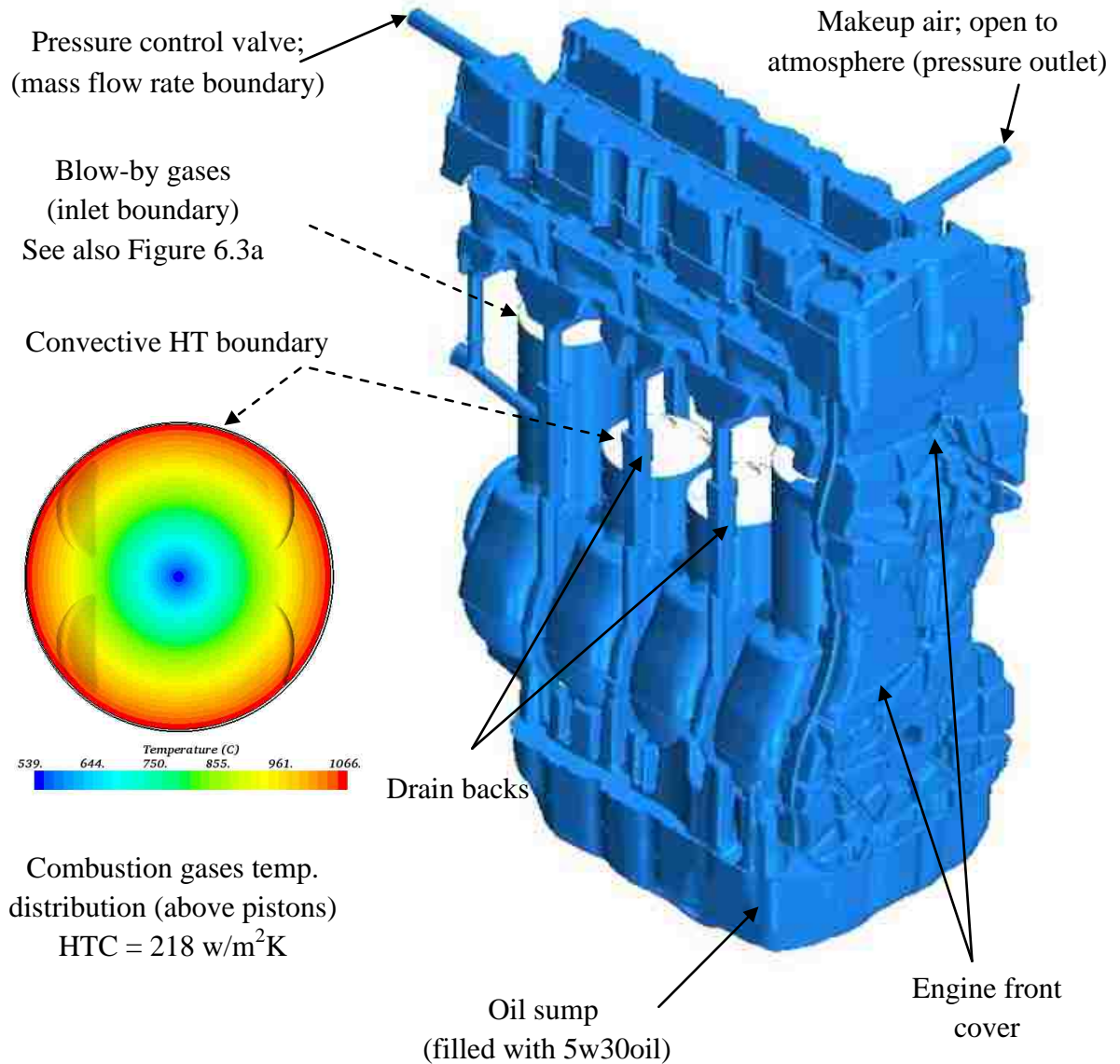
The space under the pistons and above the oil sump is referred to as the crankcase. The crankcase region usually extends up to the cylinder head. The crankcase includes many stationary and moving parts such as the crankshaft, counter weights, connecting rods, pistons, bearings, oil pumps, pipes, etc. Engine oil and air are the main fluids in the crankcase, however exhaust gases are also present. The exhaust gases (or the blow-by gases) infiltrate from the combustion chamber down into the crankcase, through the clearances between the piston rings and cylinder wall (see Figure 6.12 - Detail A). A ventilation system is required to prevent pressurizing of the crankcase. This ventilation is accomplished by redirecting the pressurized air to the intake manifold through a positive crankcase pressure valve (PCV). A "makeup air valve" is used to draw fresh air into the crankcase to compensate for any vacuum caused by the ventilation. The motion of the crank and pistons creates a specific flow pattern inside the crankcase which is responsible to maintain a positive crankcase pressure (Iqbal and Arora, 2013; Edelbauer and Diemath, 2010).

As mentioned earlier, the objective of this chapter is to computationally evaluate the piston cooling process due to an impinging jet and to set up a computational methodology for future work in this area. In such simulation, various meshing techniques are employed. This includes arbitrary sliding interface (ASI) of counter weights and mesh morphing to replicate the piston motion. An unstructured conformal computational mesh with moving cells is used in the simulation. Conformal meshing means that the whole domain, although it contains moving bodies, consists of one single mesh block and it is not decomposed into separate blocks connected by block interfaces. The conformal meshing procedure allows for the consistent modeling of multiple bodies in arbitrary motion. Information from the simulation of the generic models presented in Chapters 4 and 5 is used in the current simulation. This includes the mesh and cell sizes, the number of prism layers adjacent to the wall, time step, discretization schemes, turbulence model, etc. The acceleration methodology, which was introduced in Chapter 5 for the generic model, is also used to accelerate the simulation and reduce the computational cost.

Two simulations, one with and one without the cooling jet are carried out to evaluate the jet impingement performance. In these simulations, the VOF two-phase flow model is used to simulate the air-oil mixture. To prevent the smearing of the oil and maintain the sharpness at the air-oil interfaces, high-resolution meshing is employed at these locations, i.e., between the oil sump and crankcase, and between the oil jet and the surroundings. The blow-by gases into the crankcase as well as the breathing/ventilation process are also considered in the simulations.

## 6.2 Model Setup and Boundary Conditions

The current transient numerical simulations are used to evaluate the performance of the cooling oil jet. Two simulations were carried out, with and without an impinging jet, using the entire engine geometry. Due to the high computational cost, only one engine speed, i.e. 2000 rpm, is used in both simulations. The computational domain with relevant boundary conditions is shown in Figure 6.1. Figure 6.2 shows the interfaces between different regions inside the computational domain. In the current simulations, 7.2 M unstructured conformal polyhedral cells are used to mesh the computational domain in the case without the impinging jet, while approximately 8 M unstructured conformal polyhedral cells are used to mesh the computational domain in the presence of the impinging jet, as shown in Figure 6.3. The two-phase flow model is still required to model the case without the cooling jet, because the computational domain contains the engine oil in the oil sump as well as air, as shown in Figure 6.4. In the current simulations, all physical properties of air and engine oil are functions of the local temperature in the computational domain. The oil squirter used in this study and the velocity profile at the nozzle exit are shown in Figure 6.5a. This squirter has an exit diameter of  $d = 1.8$  mm. The oil bulk velocity at the nozzle exit is 10 m/s. Figure 6.5b shows the motion profiles of the piston and oil jet over one engine cycle. In the current simulations, the  $y^+$  value is less than 5.0, while the Courant number is less than 1.0 in the computational domain, which satisfies the CFL condition discussed in Chapter 3.



Boundary conditions:

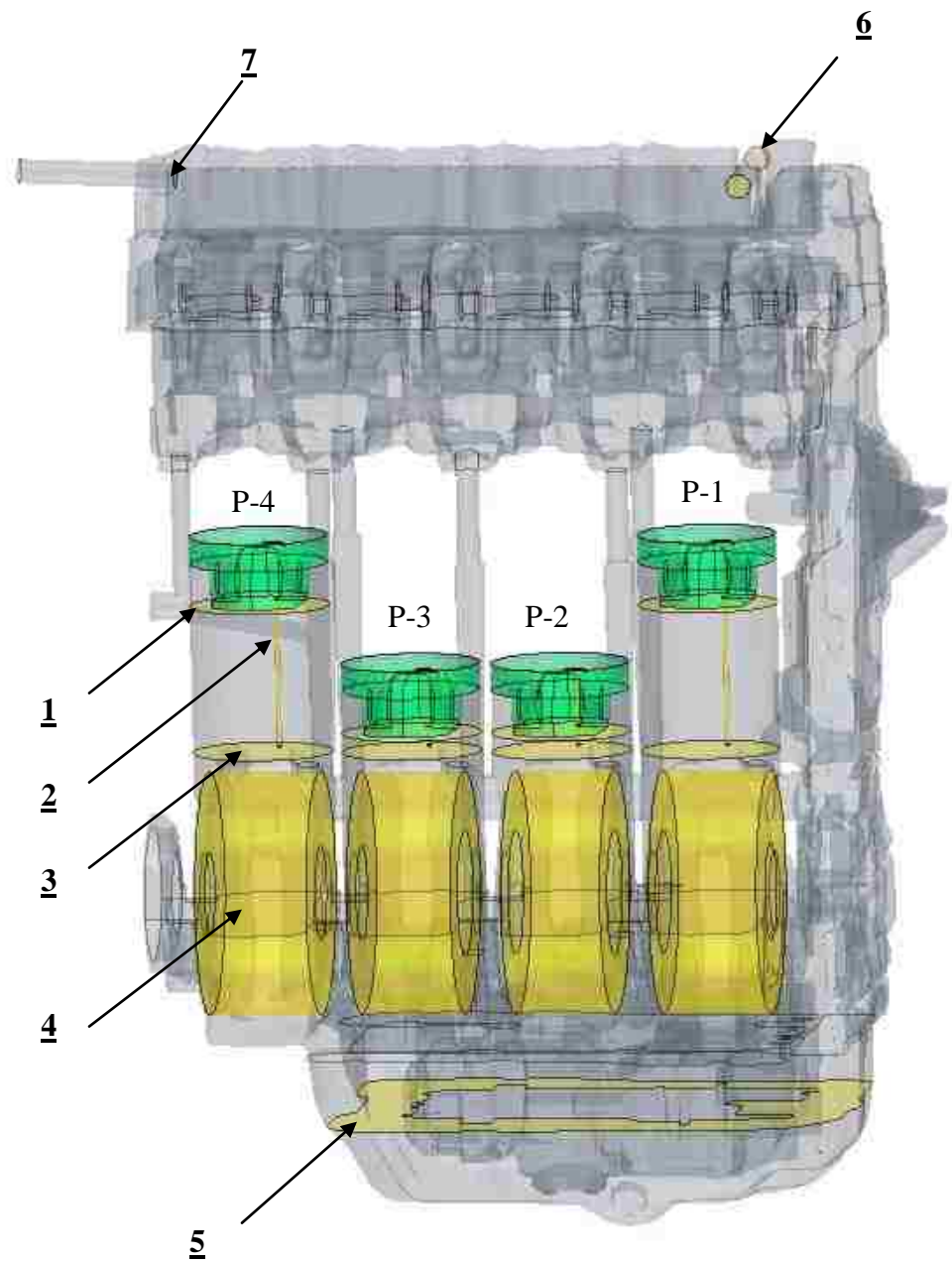
- All fluid boundaries kept at  $80^\circ\text{C}$ , but the oil sump wall and initial oil temperature are kept at  $100^\circ\text{C}$
- Oil issuing temperature is  $90^\circ\text{C}$
- Blow-by temperature is  $655^\circ\text{C}$  with mass flow rate of  $4.58 \text{ g/s}$  (averaged over the cycle) per piston
- Cylinder wall kept at  $130^\circ\text{C}$
- Physical properties of oil and air were provided previously in Table 5.1

Blue region: wetted fluid

White region: solid

Figure 6.1: Computational domain and relevant boundary conditions





- 1- Piston/cylinder interface has a linear motion (rigid body morpher)
- 2- Jet/cylinder interface has a linear motion (floating morpher)
- 3- Cylinder/crankcase interface (fixed)
- 4- Crankshaft/surrounding arbitrary sliding interface (ASI) has a rotating motion
- 5- Oil sump/ crankcase interface represents the oil level in the oil sump
- 6- Makeup air/ atmosphere interface
- 7- PCV/ inlet manifold interface

Figure 6.2: Interfaces (yellow) between different parts inside the computational domain

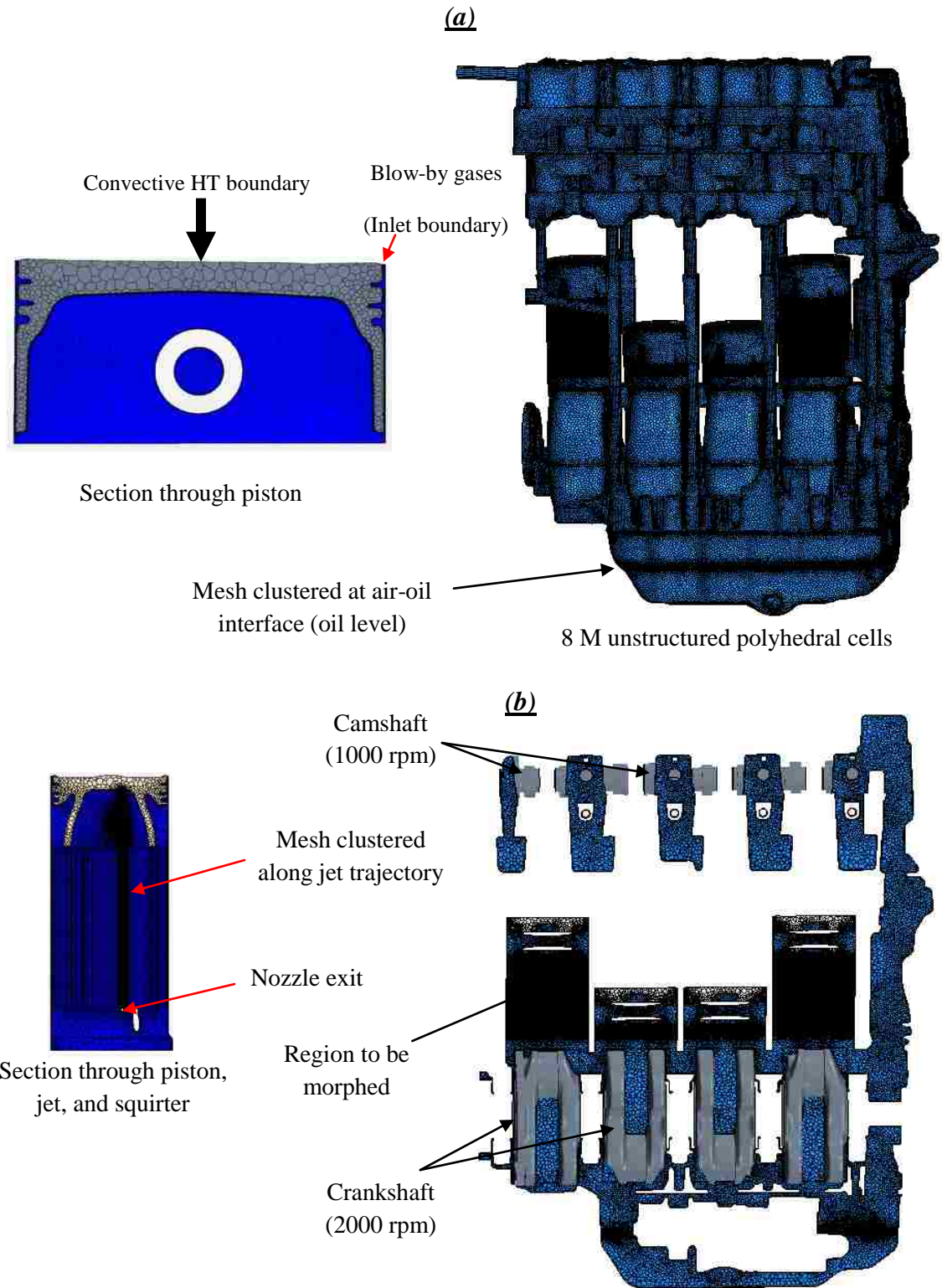


Figure 6.3: (a) Meshed domain; (b) Cross-sectional view through meshed domain

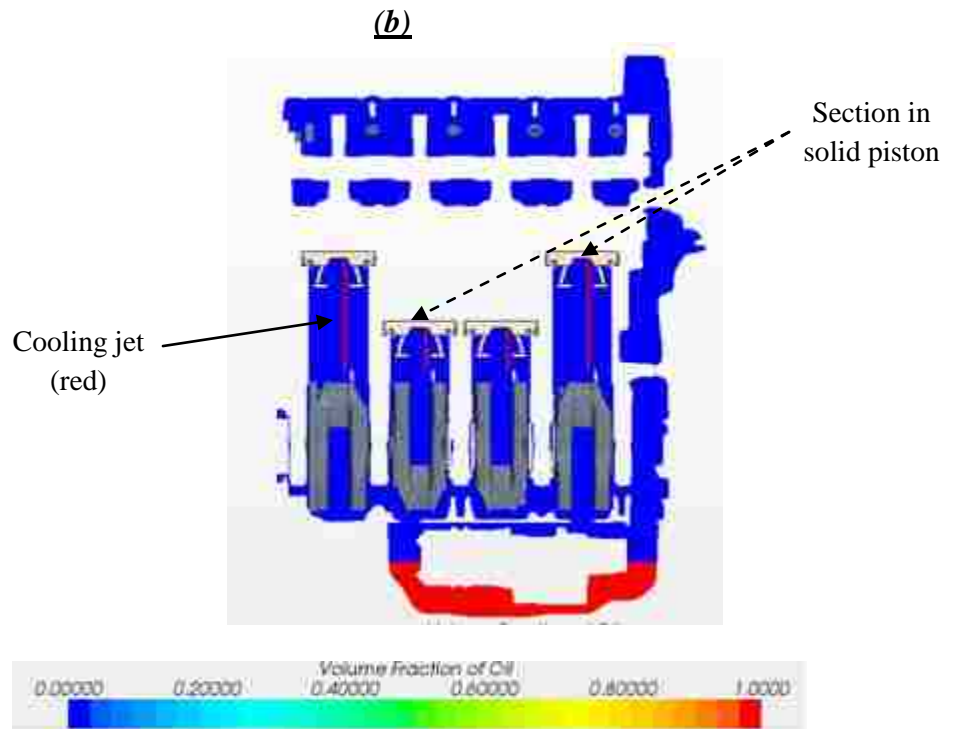
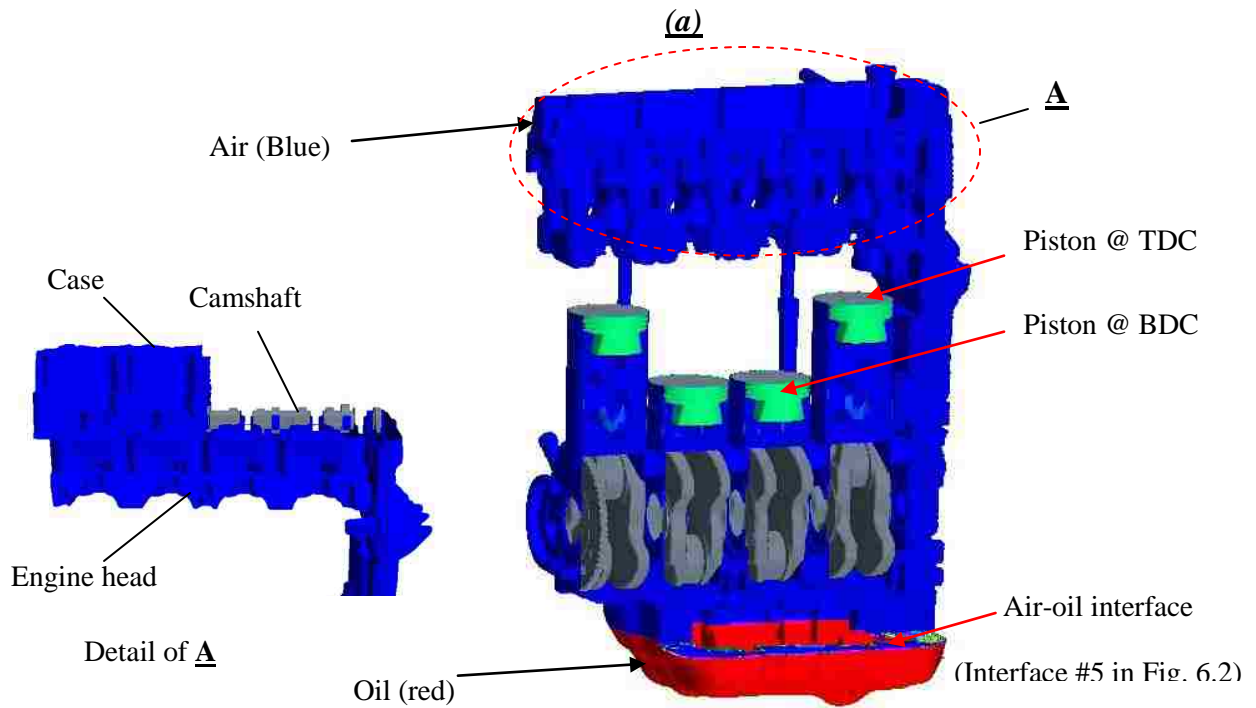


Figure 6.4: (a) VOF contours for the entire computational domain after initialization; (b)

Cross-sectional VOF contours passing through squirter and cooling jets

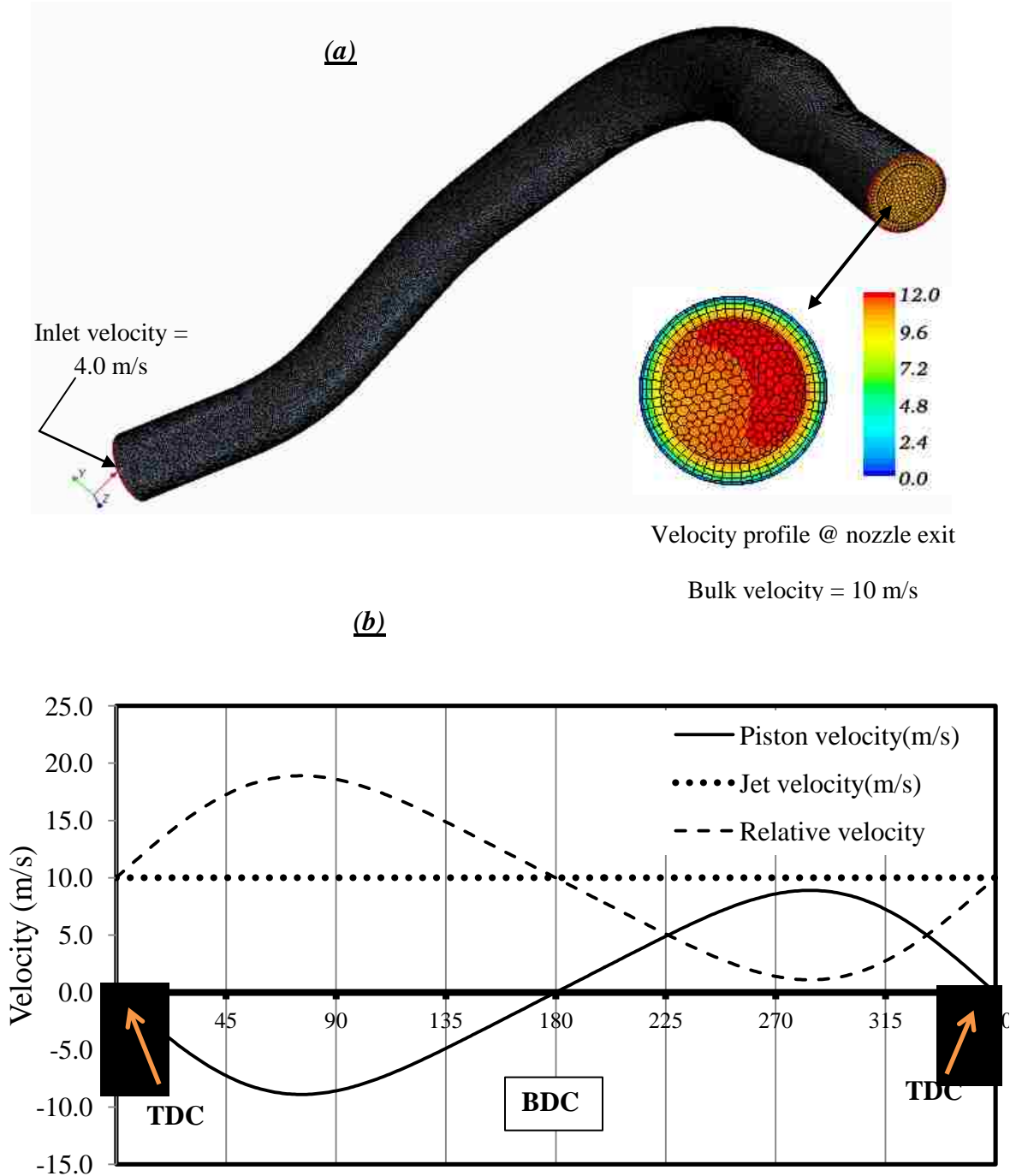


Figure 6.5: (a) Velocity profile at nozzle exit; (b) Motion profile over one cycle for engine speed  $N = 2000$  rpm

## **6.3 Results and Discussion**

### **6.3.1 Domain Initialization**

As stated in Chapter 5, the initial estimate of the temperature profile in the piston is very crucial in terms of reducing the CPU time in simulations that pose many computational challenges. These challenges emerge from the cell size and time step requirements of the VOF model, the extra computational effort due to the energy equation being activated and rotational and linear motion of the moving parts inside the computational domain. The later requires an interpolation field throughout the region at every time step to locate the new positions of the vertices. Furthermore, the computational domain includes a large number of unstructured polyhedral cells. The memory required to generate 1.0 M polyhedral mesh is 1.0 GB, while it requires only 250 MB to generate the same amount of structured mesh (STAR-CCM+ Manual, 2012). Therefore, one can appreciate the computational effort associated with polyhedral cells in comparison with the structured one. Nevertheless, the rationale for using the polyhedral mesh has been discussed in Chapter 4.

To initialize the computational domain, the initial temperature distribution in the solid piston as well as the temperature, velocity, pressure and turbulence intensity distributions inside the fluid domain, are required. The initialization process is carried out as follows:

1. The first step of the initialization process is to remove the oil sump region from the computational domain and run a single-phase simulation to find the flow field and temperature distribution in the fluid domain. At this stage we assume that the heat enters the piston at the top surface will be dissipated to the cylinder wall and the amount of the heat leakage from the piston to the fluid domain is negligible.



Therefore, the piston is considered as an isolated surface at this stage. The computational domain is shown in Figure 6.6.

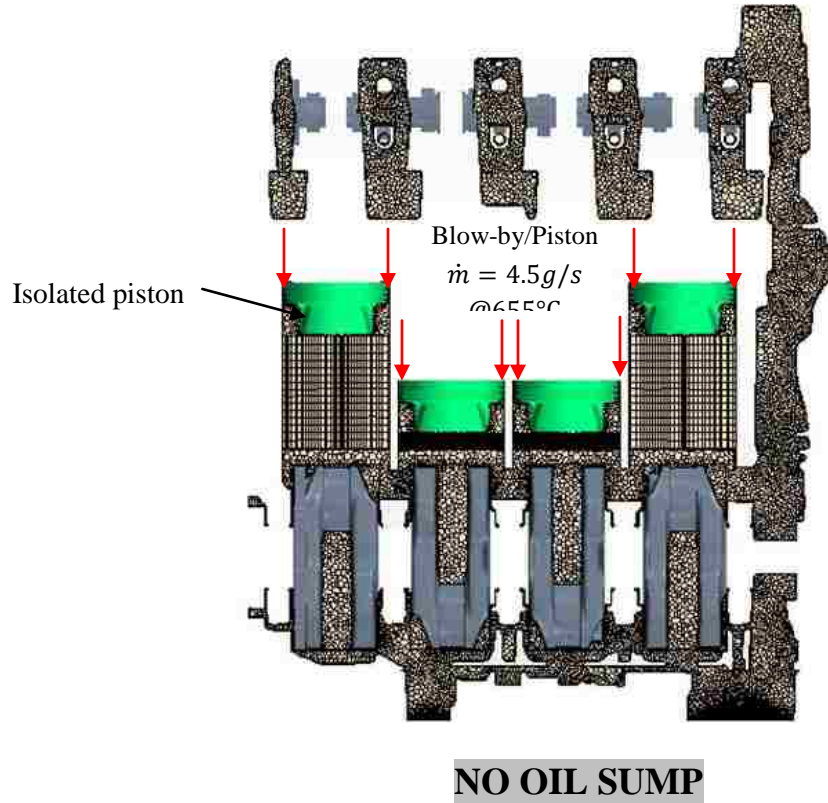


Figure 6.6: Computational domain without oil sump, used for domain initialization

2. The transient simulation for the computational domain shown in Figure 6.6 is carried out until a steady condition is attained, i.e., the domain average pressure and temperature as function of crank angle and the mass flow rate profile from the makeup air do not change for the next cycles. Figure 6.7 shows the velocity, pressure, temperature, and kinetic energy contours after the simulation attains the steady-state condition. These contours are used to initialize the fluid domain for the entire

computational domain shown in Figure 6.1 for both cases, i.e., with and without cooling jet.

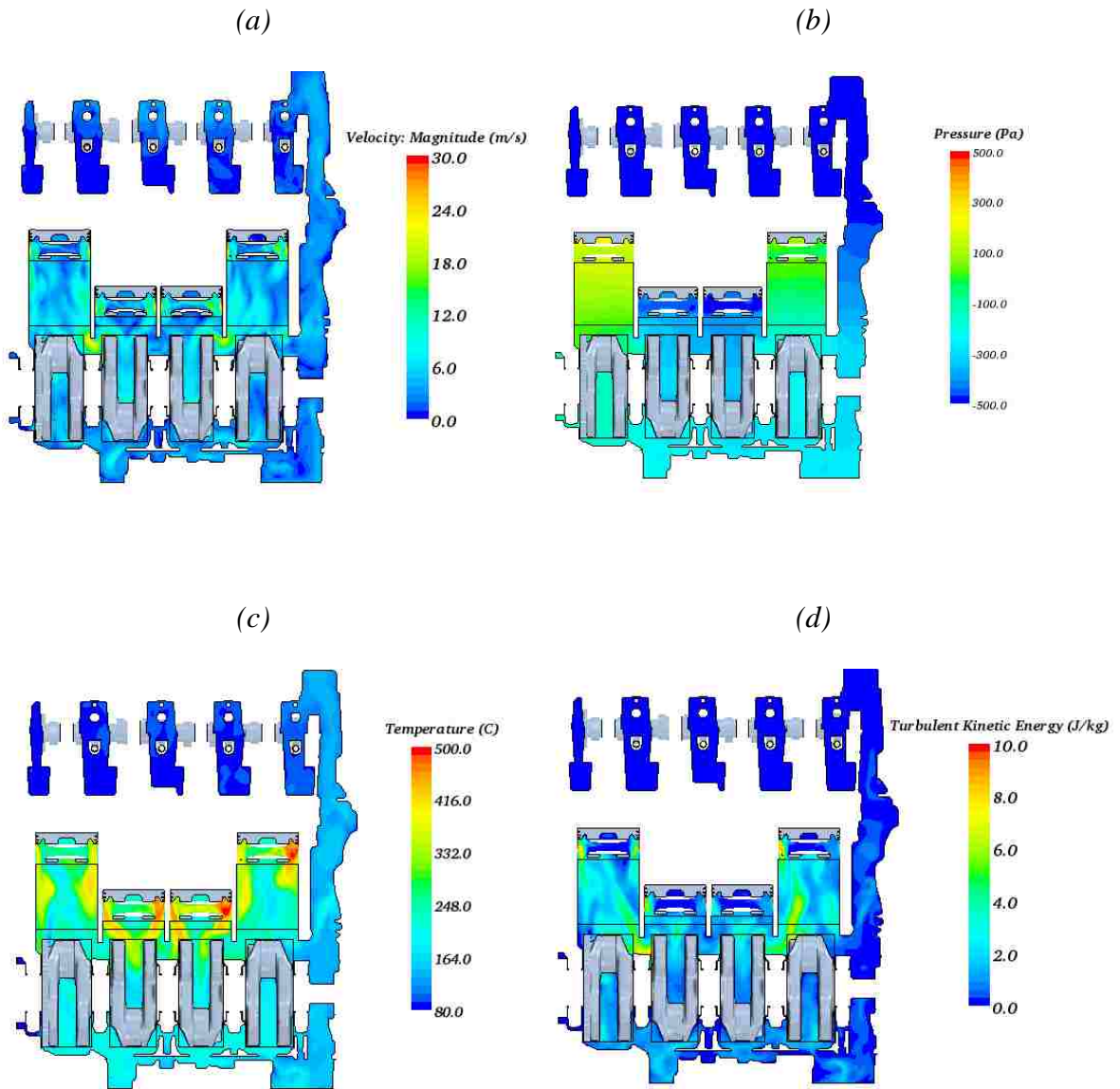


Figure 6.7: Steady-state contours from transient simulation for the computational domain shown in Figure 6.6; (a) Velocity magnitude; (b) Pressure; (c) Temperature; (d)

Turbulent kinetic energy

3. The next step in the process is to find the initial temperature distribution in the solid piston for both cases. To this end, only a portion of the entire computational domain is used, i.e., one piston and one cylinder. In the current simulation, the cylinder and piston number 4 shown in Figure 6.8 was used for this purpose.

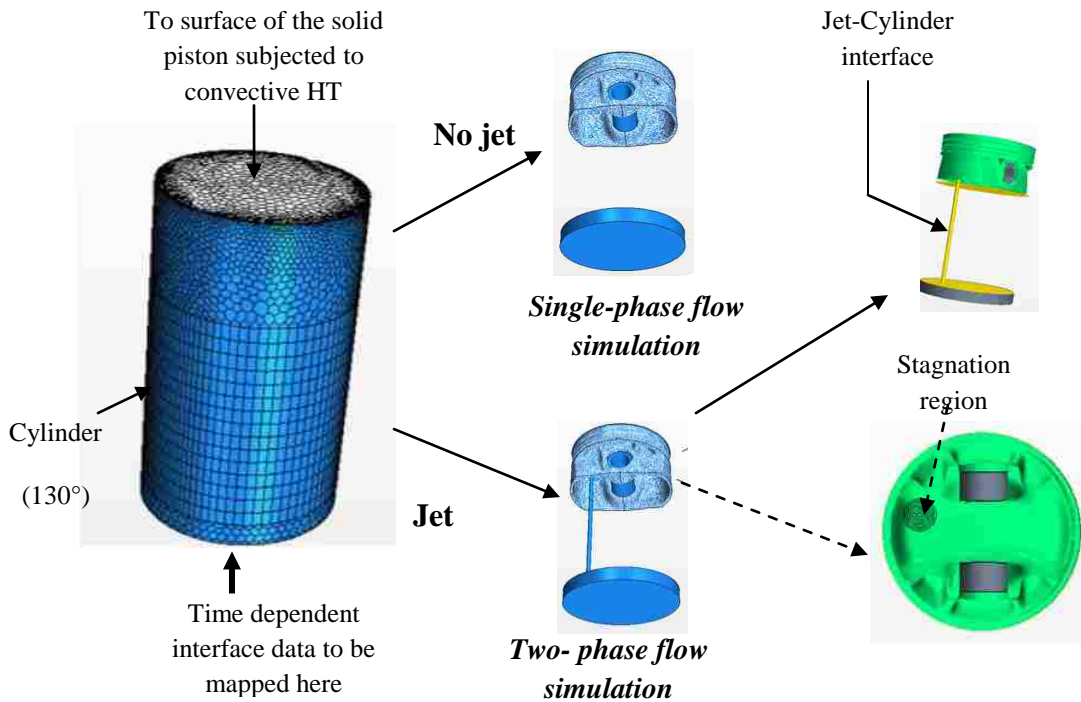


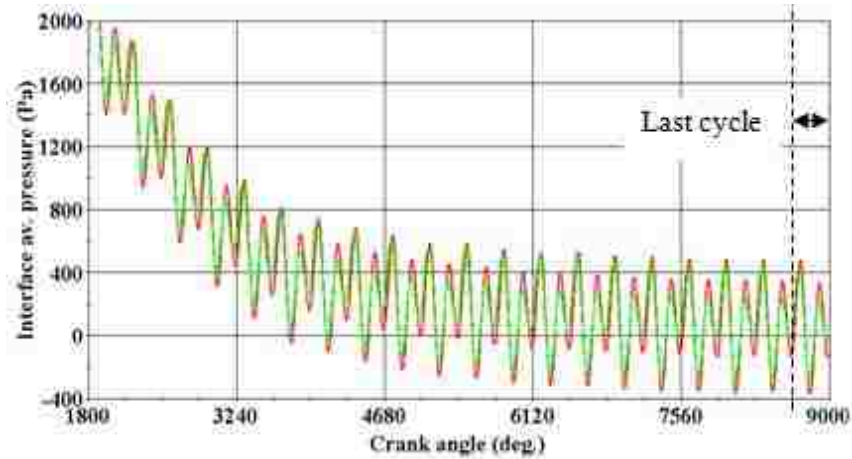
Figure 6.8: Computational domain used to find the temperature profile in the solid piston with and without cooling jet

The boundary conditions as function of the crank angle are extracted at the cylinder/crankcase interface over one cycle from the simulation in step 2, i.e., interface 3 shown in Figure 6.2. Figure 6.9 shows the temperature and pressure profiles as function of crank angle, extracted at the cylinder/crankcase interface for cylinders 1 and 4. The last cycle of pressure and temperature (shown in Figure 6.9), velocity and kinetic energy (not shown here) are mapped as a time dependent

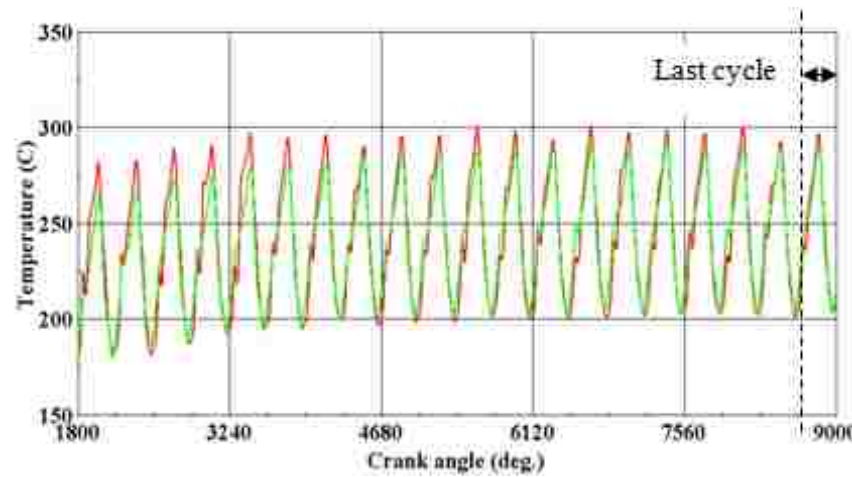


boundary condition at the interface marked in Figure 6.8. Two simulations, one with and one without the cooling jet, are run to find the initial temperature distribution in the piston. The acceleration methodology outlined in Chapter 5 is used here with the cooling jet to expedite the simulation.

(a)



(b)



— Interface of cylinder / crankcase - bay 1 — Interface of cylinder / crankcase - bay 4

Figure 6.9: (a) Pressure and (b) temperature profile as function of crank angle, extracted at cylinder/ crankcase interface (interface 3 shown in Figure 6.2)

### 6.3.2 Nusselt Number Profiles

After the initialization of the computational domain, the simulation is run for the full engine geometry to obtain the transient Nusselt number distribution on the surface of the piston as function of crank angle, with and without cooling jet. The piston-fluid interface is split into several regions as shown in Figure 6.10. Each colour in this figure represents a separate region.

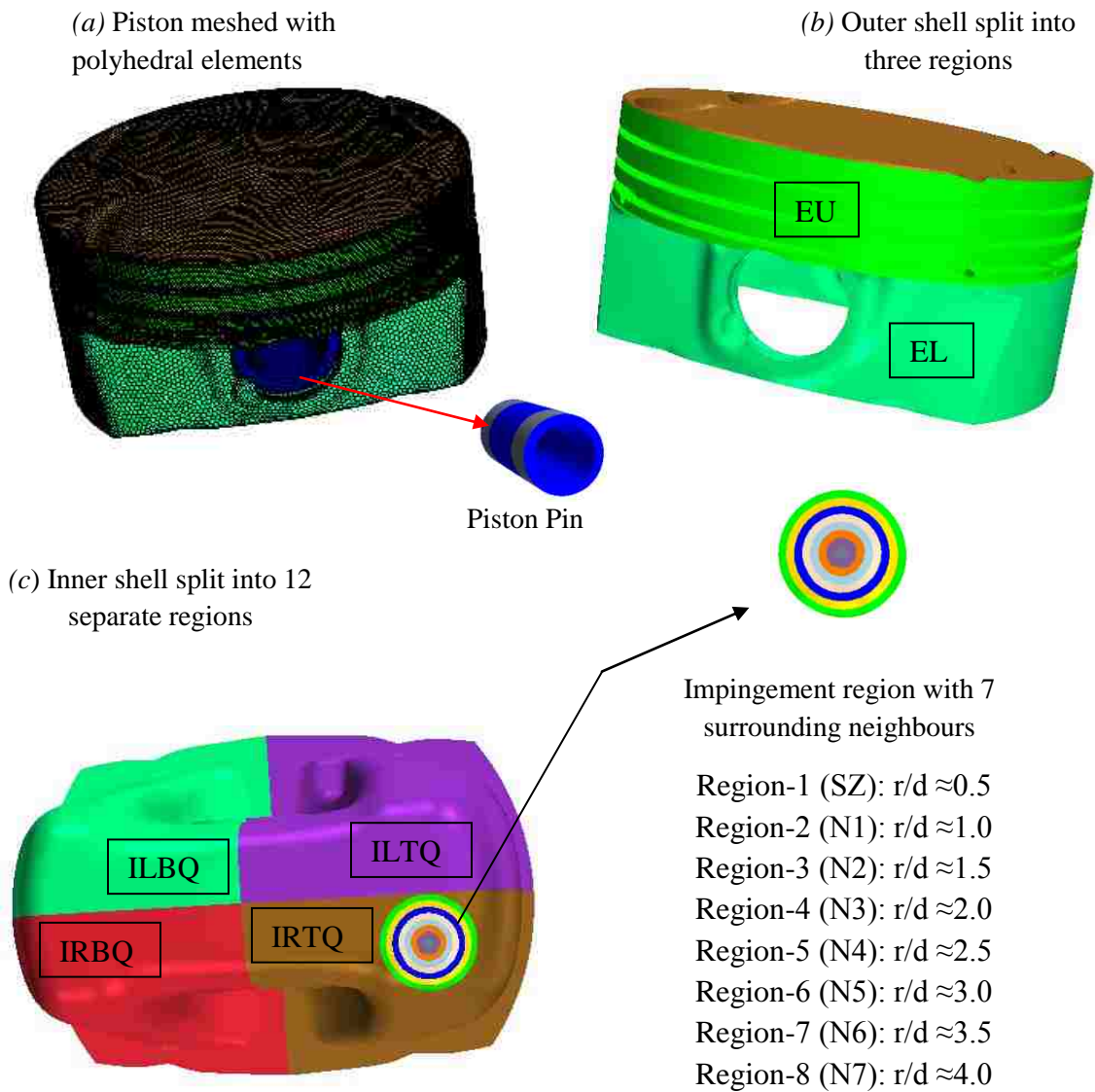


Figure 6.10: Solid piston configuration; (a) Entire piston; (b) External shell;

(c) Internal shell

The simulations are conducted under the following assumptions:

- The temperature of the piston pin is kept constant, i.e.,  $T_{pin} = 200^{\circ}\text{C}$  (Stone, 2012).
- The time step from the generic model in Chapter 5 for  $\omega = 210$  rad/s (2000 rpm) is used.

In this stage of the simulation, the compression and oil rings of the piston are not included in the computational domain. It is difficult to implement the meshing in such tight regions due to the small clearance between the rings and piston walls on one hand and between the rings and cylinder walls on the other hand. Therefore, two transient simulations are required. In the first simulation, the transient Nusselt number profile is obtained using the full-scale engine without the piston rings. The Nusselt number profiles without and with the cooling jet are shown in Figures 6.11a and 6.11b. The transient Nusselt number is averaged from the recurring cycles in these figures to obtain one average cycle Nusselt number for each region at the fluid-solid interface (see also Chapter 5, section 5.3.2.2). These profiles will be used in the second simulation (see next subsection) as a boundary condition to find the temperature distribution in the piston.

Only the piston and compression rings are used as a computational domain in the second stage. The heat dissipation is insignificant through the oil ring (Stone, 2012), therefore this ring is excluded from the computational domain. The HTC (or  $Nu$ ) in Figure 6.11a is calculated using the blow-by temperature as a reference temperature, i.e.,  $T_{ref} = 655^{\circ}\text{C}$ , while the jet issuing temperature,  $T_{ref} = 90^{\circ}\text{C}$ , is used to calculate the HTC and then  $Nu$  in Figure 6.11b. The different reference temperatures interpret the positive and negative sign of HTC or  $Nu$  in Figure 6.11a and 6.11b, where the

Newton law of cooling is used to calculate the HTC. It was noticed that the HTC is comparable for both cases, i.e., with and without cooling jet at the external shell of the piston. Based on  $T_{ref} = 655^{\circ}\text{C}$ , the surface average HTC over one cycle is  $185 \text{ W/m}^2\cdot\text{K}$  and  $8.0 \text{ W/m}^2\cdot\text{K}$  approximately, corresponding to the outer shell regions, i.e., Region-EU and Region-EL shown in Figure 6.10b.

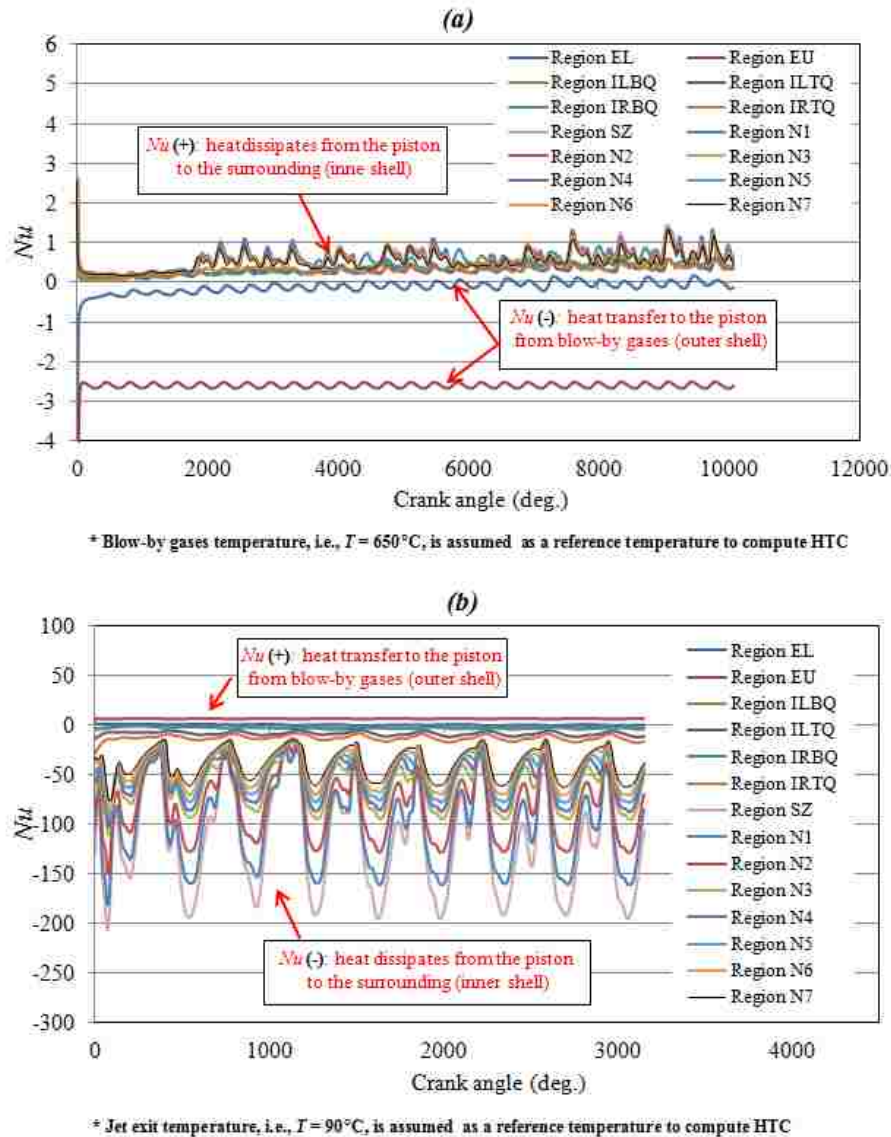


Figure 6.11: Average Nusselt number at piston-fluid interface; (a) without cooling jet; (b) with cooling jet

### 6.3.3 Piston Temperature Profile

The temperature profiles in the piston are obtained by conducting a transient simulation using the solid piston and two compression rings as shown in Figure 6.12. The oil ring has not been used in this simulation. Since the material of the piston is mainly aluminium alloy and the material of the rings is cast iron, it is necessary to use two physics continua in this simulation. The contact resistance of conduction between the piston and piston rings is taken as  $R_c = 2 \times 10^{-5} \text{m}^2 \cdot \text{K/W}$  (Cengel & Ghajar, 2011). The temperature of the ring tip, which slides and contacts the cylinder wall, is set at  $140^\circ\text{C}$ , i.e.,  $10^\circ\text{C}$  higher than the cylinder wall temperature. The other surfaces of the ring are subjected to convective heat transfer due to the blow-by gases.

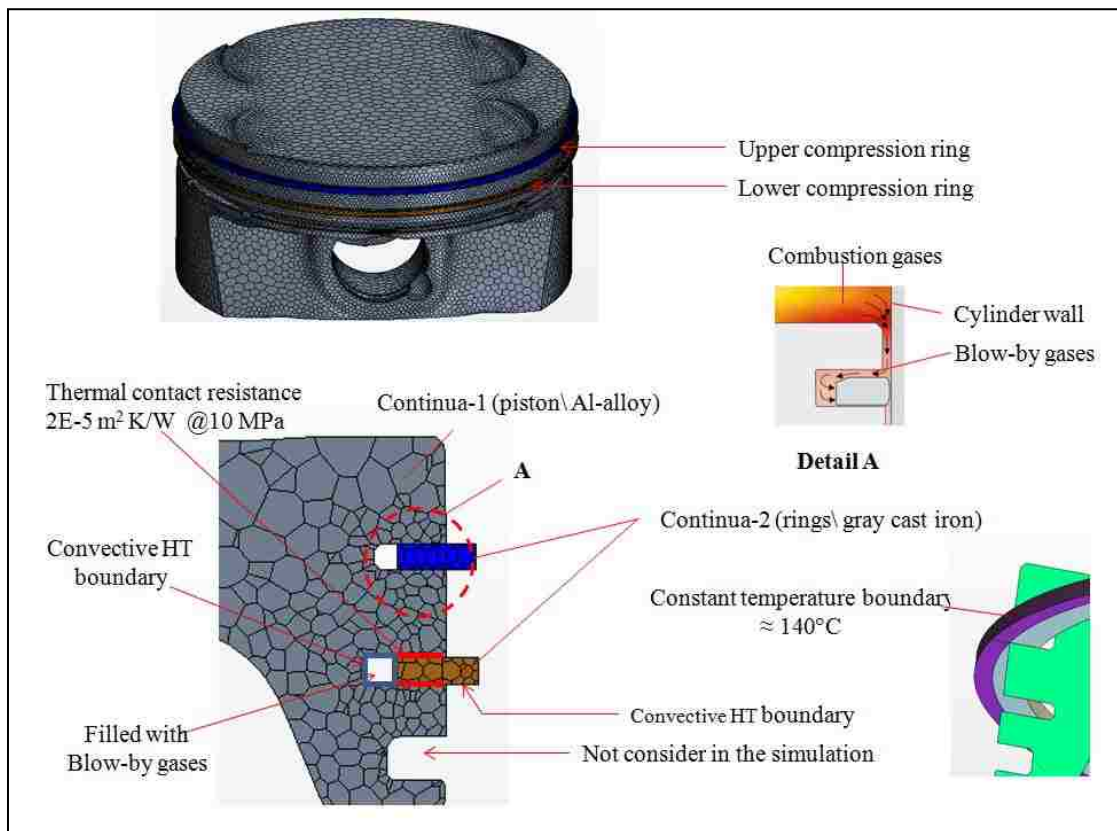


Figure 6.12: Computational domain (piston and two compression rings) with the relevant thermal boundary conditions

The transient profiles of Nusselt number from the previous section are mapped at the corresponding piston surfaces for the current simulation. Two transient simulations are carried, i.e., using the heat transfer coefficient profiles with and without the cooling jet. Figures 6.13 and 6.14 show the temperature profile in the piston for both cases. In this simulation, the volume flow rate of oil from each squirter in the engine is  $\dot{Q} = 0.025 \text{ m}^3/s$  at  $90^\circ\text{C}$ .

Examination of the temperature contours in Figure 6.13 (case without jet) reveals that the contour of higher temperature is shifted towards the left edge of the piston. The highest temperature appears in the region above the stagnation zone, right below the exhaust valves. It should be noted that the phrase "stagnation zone" is metaphorically used here (no jet case), just to mark the location of this region for comparison purpose with the jet case. The weight of the left side of the piston (exhaust side) is more than the weight of the right side of the piston (intake side). This design is intentionally considered to tolerate the higher thermal stress at the exhaust side of the piston. Therefore, more metal at the exhaust side leads to a higher thermal conductance resistance and consequently a higher temperature at this region.

For the jet case, the contour of highest temperature is shifted towards the right edge of the piston as shown in Figure 6.14. The highest temperature appears in the region below the intake valves. However, this temperature remains less than the temperature at the same corresponding location in the case of no jet.

For this specific simulation, the volume average, the stagnation zone, the maximum and minimum temperatures in the piston are reduced by 10%, 25%, 12% and 25% , respectively, with the cooling jet in comparison with no cooling jet.

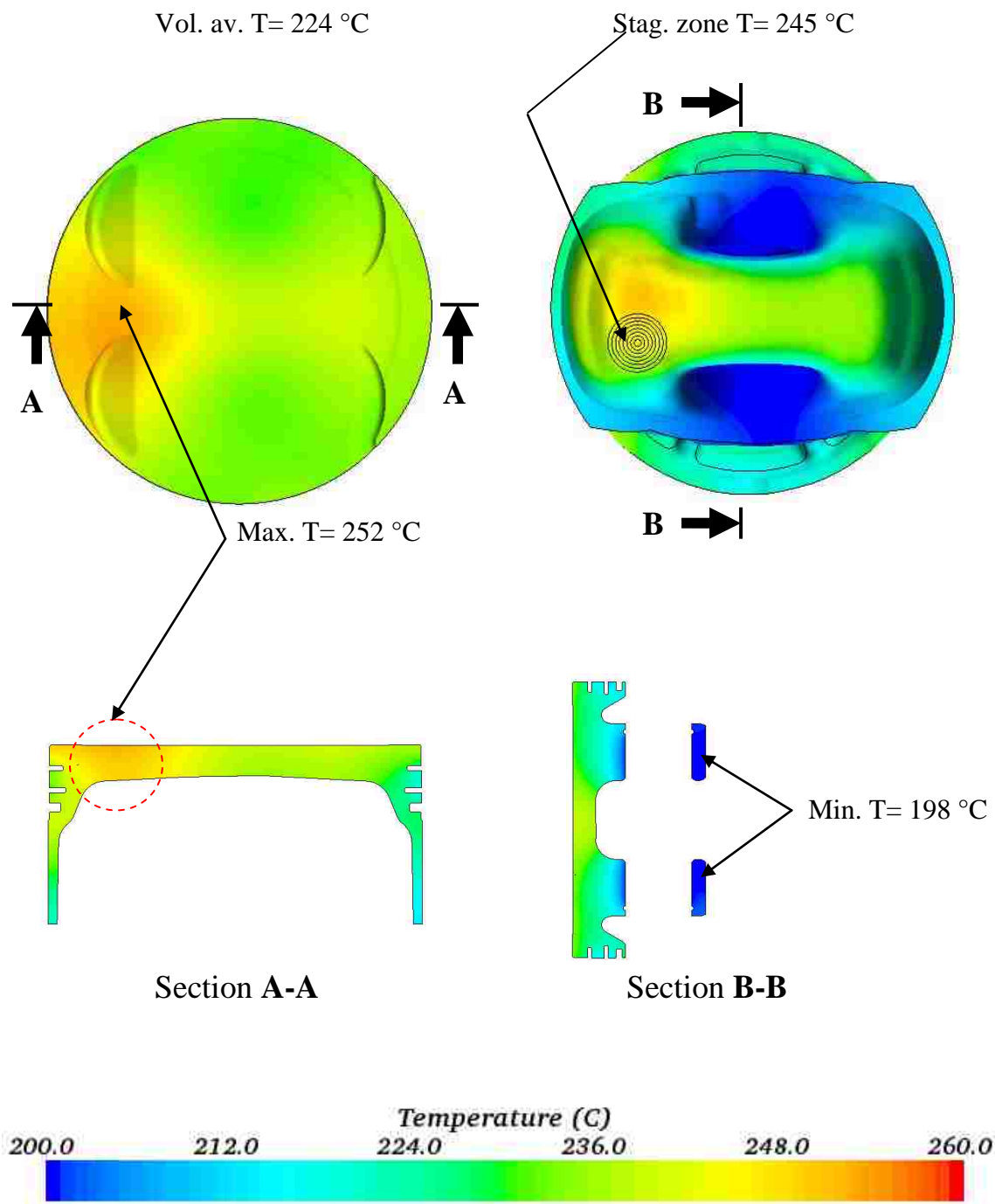


Figure 6.13: Temperature profile in the piston without cooling jet,  $N = 2000\text{ rpm}$



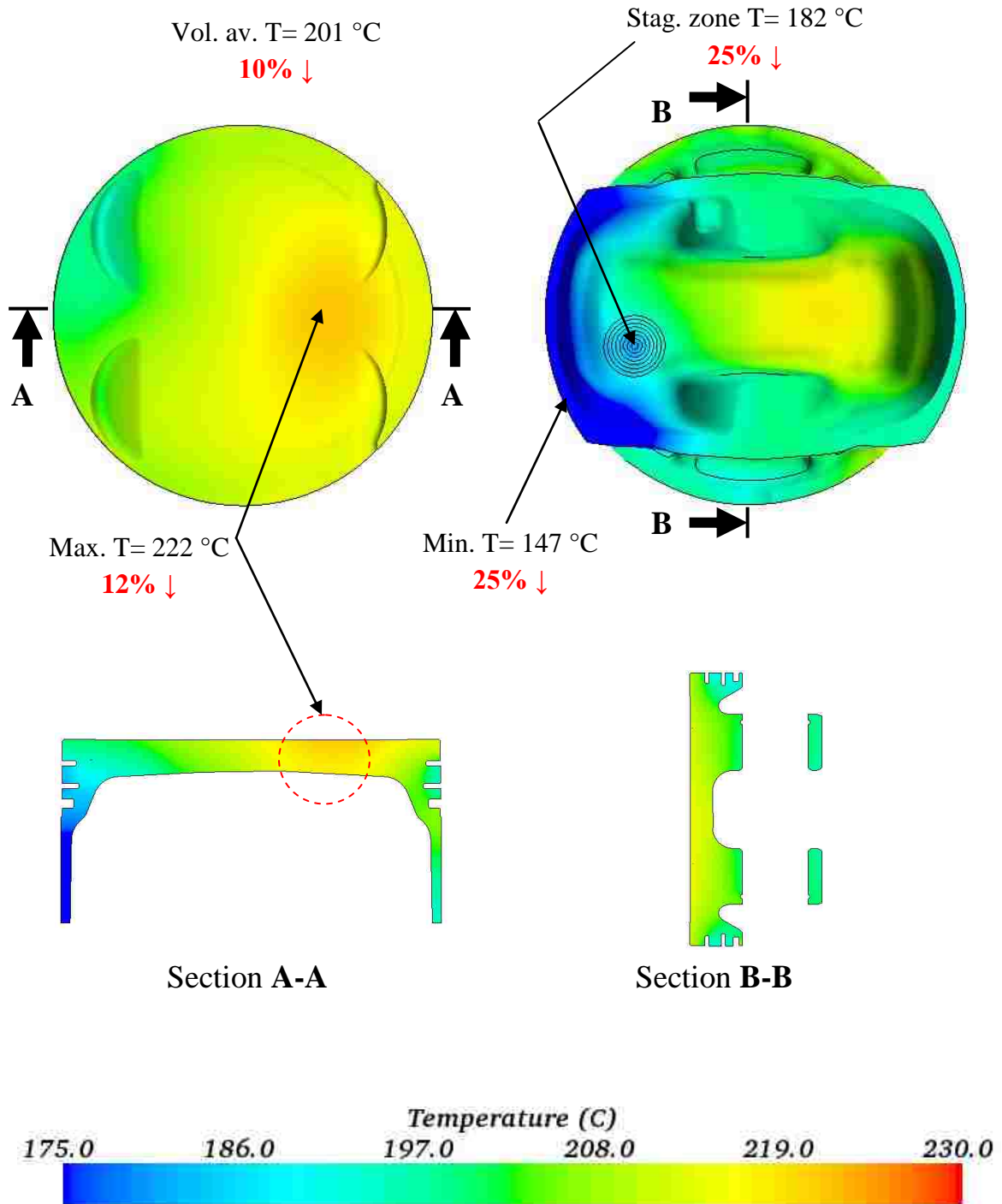


Figure 6.14: Temperature profile in the piston with cooling jet,  $N = 2000\text{ rpm}$ ,  
 (jet flow rate  $\dot{Q} = 0.025\text{ m}^3/\text{s}$ ,  $v_{bulk} = 10\text{ m/s}$ )



Table 6.1 gives the heat dissipation through different parts of the piston with and without the cooling jet. The amount of heat passing into the piston increases by 4% with the cooling jet. The temperature difference between the surroundings and the solid piston is higher with the cooling jet. This will enhance the convective heat transfer into the piston. The amount of heat dissipation through the piston rings is 64% and 68% of the total heat into the piston for the two cases. The temperature of the piston pin is kept constant in both simulations, i.e., 200°C (Stone, 2012). Therefore, the difference between the volume average temperature of the piston (see Figures 6.13 and 6.14) and the piston pin is 24°C and 1°C for the two cases. This will drive 28% of the total heat to be dissipated through the piston pin in the case with no cooling jet and increases the heat dissipated through the rings in the case with the cooling jet. The amount of heat dissipation through the inner shell of the piston is four times larger in the case of the cooling jet in comparison with the no jet case. This is attributed to the high heat transfer coefficient associated with the cooling jet.

	Without jet	With jet
Total heat into the piston (W)	1600	1670
Heat dissipation through piston rings (W)	1020 <b>(64%)</b>	1138 <b>(68%)</b>
Heat dissipation through piston pin (W)	451 <b>(28%)</b>	~0 <b>(0%)</b>
Heat dissipation through inner surface (W)	129 <b>(8%)</b>	530 <b>(32%)</b>

Table 6.1: Heat dissipation through different parts of the piston with and without jet

## 6.4 Conclusions

In this chapter, an automotive engine application of the cooling oil jet is evaluated. A transient CFD simulation of the Chrysler 2.0 L Tigershark Inline 4-Cylinder gasoline engine is used to evaluate the oil jet impingement process to cool down the pistons. The boundary conditions for the simulation are extracted from a one-dimensional simulation (GT-Power Modeling).

The convective heat transfer coefficient distribution on the piston wall and the temperature profile are computed to evaluate the jet cooling performance. The heat dissipation through different piston parts is estimated with and without the cooling jet. The conclusions from this simulation can be summarized as follows:

- A methodology is presented to find the steady solution of the flow field in the crankcase and the temperature profile in the piston with and without a cooling oil jet. The simulation can predict the location of the maximum and minimum temperature as well as the temperature distribution in the piston.
- The contour of maximum temperature in the piston is found directly beneath the exhaust valves in the case without the cooling jet. An impinging jet can cool down this region.
- The contour of highest temperature in the piston is found beneath the intake valves in the case with the cooling jet. However, this temperature remains less than the temperature at the same corresponding location in the case of no jet.
- The amount of heat into the piston from combustion gases increases in the presence of the cooling jet. The temperature difference between the surroundings and the solid

piston is higher with the cooling jet. This will enhance the convective heat transfer into the piston.

- The impinging jet is regarded as a method of achieving particularly high convective heat transfer coefficients and therefore enhances the heat transfer from the inner shell of the piston, particularly from the stagnation region and its neighbouring regions. The amount of heat dissipation through the inner shell of the piston is four times higher in the case of the cooling jet in comparison with the no jet case.
- The amount of heat dissipation through the piston rings is comparable for both cases. In addition, the heat dissipation from the inner shell of the piston with the cooling jet is comparable to the heat dissipation through the piston pin and the connecting rod with no oil jet. In other words, the heat source inside the crankcase is comparable for both cases. Therefore, a high rise in the temperature of the oil in the oil sump is not expected. More investigation is required in the future to verify and generalize this outcome.

## CHAPTER 7

### CONCLUSIONS AND RECOMMENDATIONS

#### 7.1 Conclusions

The research in this study was focused on exploring the performance of a liquid (oil) cooling jet. A computational study was carried out to investigate the heat transfer due to liquid jet impingement onto a solid surface. Specific conclusions have been drawn at the end of each chapter, based on the results of the simulations described in that chapter. From a global perspective, the major conclusions may be summarized as follows.

- The maximum heat transfer coefficient due to jet impingement occurs in the region within the fluid film where the radial velocity gradient is positive. In other words, the stagnation region exists within the accelerating region around the stagnation point and extends up to the interface between the positive and negative velocity gradients in the liquid film adjacent to the wall.
- Despite the fact that many researchers have claimed that the extent of the stagnation region is fixed, the computational data suggests that the radial extent of the stagnation region beneath the jet is not uniform, but is a function of the radial velocity gradient  $\partial u_r / \partial r$  in this region.
- For jet impingement onto a stationary boundary, a correlation has been developed describing the stagnation zone Nusselt number. This correlation is applicable over a wide range of Reynolds numbers and Prandtl numbers. This correlation is expressed in terms of Reynolds number, Prandtl number and a non-dimensional radial velocity gradient. It does not explicitly depend on the nozzle-to-target spacing since it is applicable only for long jets, i.e.,  $H/d > 10.0$ .

- Correlations to predict local Nusselt number have been also developed for jet impingement onto a fixed boundary. In these correlations, the normalized local Nusselt number varies weakly with Reynolds number for given nozzle size. It can be approximately considered to be a function of  $r/d$  only.
- For a given Reynolds number, the temperature distribution on the impinging surface is more uniform for larger nozzles compared to smaller nozzles. Smaller nozzles provide more efficient cooling at the stagnation region and subsequently lower temperature. Larger nozzles cool the surface more uniformly.
- For given nozzle size and Reynolds number, the shorter jet provides a more efficient localized cooling (higher HTC) in comparison with the longer jet. However, the longer jet provides a more efficient surface average cooling (higher HTC) in comparison with the shorter jet.
- For given nozzle size and Reynolds number, the effect of nozzle geometry is insignificant on the thermal characteristics for long jets. The viscosity tends to eliminate the velocity gradient in the radial direction for long jets, which results in a constant velocity gradient at the stagnation point.
- For jet impingement onto a moving boundary, an innovative methodology to accelerate the computational solution and reduce the cost in terms of CPU time has been proposed in this study. The acceleration procedure relies mainly on the cyclic profile of Nusselt number. The steady cyclic profile of the transient Nusselt number only occurs when the temperature distribution in the disc is close to the final temperature distribution.

- For jet impingement onto a moving boundary, the maximum Nusselt number is attained a short time after the relative velocity between the disc and the jet reaches its maximum. The turning process of the jet after impingement lags the occurrence of maximum HTC by a few degrees.
- For industrial applications, it may be reasonable to perform a steady-state simulation to obtain a cost effective prediction of temperature distribution even when the disc has a reciprocating motion.
- As an application of the jet cooling process, the impinging oil jet is investigated for piston cooling. A Chrysler full-scale engine is used in the simulation. A procedure was set up that can be followed for future similar simulations. For the specific simulation carried out in this study, the volume average, the stagnation zone, the maximum and minimum temperatures in the piston are reduced by 10%, 25%, 12% and 25%, respectively, with the cooling oil jet in comparison with the case of no cooling jet.

## **7.2 Recommendations for Future Work**

Through this computational study of jet impingement heat transfer, several issues about the cooling process by jet impingement have come to light and should be considered. Some recommendations for the future work are as follows:

- Further investigations are needed for a cooling jet impinging onto a moving boundary to examine the effects of nozzle size and a wide range of jet Reynolds number.
- Another important aspect that can complement the results of the current study is the effect of jet inclination angle on the jet impingement cooling process.

- For automotive industry applications, more studies are required to investigate the consequences of the cooling oil jet impingement inside the crankcase, i.e., the temperature rise of the oil in the crankcase due to the cooling jet.
- Further computational approaches should be investigated to reduce the cost in term of CPU time with the entire engine simulation and make it more feasible from the industrial point of view.

## REFERENCES

- Agarwal, A.K., Goyal, S.K., and Srivastava, D.K., Time Resolved Numerical Modelling of Oil Jet Cooling of a Medium Duty Diesel Engine Piston, *International Communications in Heat and Mass Transfer*, Vol. 38, pp. 1080-1085, 2011.
- Anderson, J.D., *Computational Fluid Dynamics, The Basics with Applications*, McGraw-Hill, NY, USA, 1995.
- Arolla, S.K., and Durbin, P.A., Modeling Rotation and Curvature Effects within Scalar Eddy Viscosity Model Framework, *J. Heat and Fluid Flow*, Vol. 39, pp. 78-89, 2013.
- Astrachancev, G.P., An Iterative Method of Solving Elliptic Net Problems, *USSR Computational Mathematics and Mathematical Physics*, Vol. 11, pp. 171–182, 1971.
- Azuma, T., and Hoshino, T., The Radial Flow of a Thin Liquid Film, Part 1: Laminar-Turbulent Transition, *JSME*, Vol. 27, pp. 2739-2746, 1984a.
- Azuma, T., and Hoshino, T., The Radial Flow of a Thin Liquid Film, Part 2: Film Thickness, *JSME*, Vol. 27, pp. 2747-2754, 1984b.
- Azuma, T., and Hoshino, T., The Radial Flow of a Thin Liquid Film, Part 3: Velocity Profile, *JSME*, Vol. 27, pp. 2755-2762, 1984c.
- Azuma, T., and Hoshino, T., The Radial Flow of a Thin Liquid Film, Part 4: Stability of Liquid Film and Wall Pressure, *JSME*, Vol. 27, pp. 2763-2770, 1984d.
- Bakhvalov, N.S., On the Convergence of a Relaxation Method with Natural Constraints on the Elliptic Operator, *USSR Computational Mathematics and Mathematical Physics*, Vol. 6, pp. 101–113, 1966.
- Behnia, M., Parneix, S., and Durbin, P., Simulation of Jet Impingement Heat Transfer with the  $k-\varepsilon-v^2$  Model, Center for Turbulence Research, Annual Research Briefs, Stanford University, Stanford, CA, USA, 1996.
- Bhunja, S.K., and Lienhard, J.H., Splattering During Turbulent Liquid Jet Impingement on Solid Targets, *J. Fluids Eng.*, Vol. 116(2), pp. 338-344, 1994a.
- Bhunja, S.K., and Lienhard, J.H., Surface Disturbance Evolution and the Splattering of Turbulent Liquid Jets, *J. Fluids Eng.*, Vol. 116(4), pp. 721-727, 1994b.
- Burmeister, L.C., *Convective Heat Transfer*, Wiley, NY, USA, 1983.
- CD-adapco, STAR-CCM+, V7.02.008, User Manual, 2012.



- Cengel, Y.A., and Ghajar, A.J., Heat and Mass Transfer: Fundamentals and Applications, 4<sup>th</sup> ed., McGraw-Hill, NY, USA, 2011.
- Dai, Z., Chou, W.H., and Faeth, G.M., Drop Formation Due to Turbulent Primary Breakup at the Free Surface of Plane Liquid Wall Jets, Phys. Fluids, Vol. 10, pp. 1147–1157, 1998.
- Donaldson, C.D., Snedeker, R.S., and Margolis, D.P., A Study of Free Jet Impingement, Part 2: Free Jet Structure and Impingement Heat Transfer, J. Fluid Mech., Vol. 45, pp. 477-521, 1971.
- Durbin, P.A., On the  $k$ - $\varepsilon$  Stagnation Point Anomaly, Int. J. Heat and Fluid Flow, Vol. 17, pp. 89-90, 1996.
- Edelbauer, W., and Diemath, A., Simulation of the Ventilation Losses in the Crankcase of an Internal Combustion Engine, Progress in Computational Fluid Dynamics, Vol. 10(1), pp. 1-18, 2010.
- Eggers, J., and Villermaux, E., Physics of Liquid Jets, Phys. Fluids, Vol. 71(3), pp. 1–79, 2008.
- Elison, B., and Webb, B., Local Heat Transfer to Impingement Liquid Jets in the Initially Laminar, Transitional, and Turbulent Regimes, Int. J. Heat and Mass Transfer, Vol. 37, pp. 1207–1216, 1994.
- Errico, M., A Study of the Interaction of Liquid Jets with Solid Surfaces, PhD Thesis, University of California, San Diego, CA, USA, 1986.
- Fedorenko, R.P., The Speed of Convergence of One Iterative Process, USSR Computational Mathematics and Mathematical Physics, Vol. 4, p. 227-235, 1964.
- Ferziger, J.H., and Peric, M., Computational Methods for Fluid Dynamics, 3<sup>rd</sup> ed., Springer, NY, USA, 2002.
- Gutfinger, G., Topics in Transport Phenomena, Hemisphere Publishing Corporation, John Wiley and Sons, Washington, USA, 1975.
- Hewitt, G.F., Shires, G.L., and Bott, T.R., Process Heat Transfer, CRC Press, Boca Raton, FL, 1994.
- Hirt, C.W., and Nichols, B.D., Volume of Fluid (VOF) Method for the Dynamics of Free Surfaces, J. Computational Physics, Vol. 39, pp. 201-225, 1981.
- Hsiang, L.P., and Faeth, G.M., Drop Deformation and Breakup Due to Shock Wave and Steady Disturbances, Int. J. Multiphase Flow, Vol. 21(4), pp. 545–560, 1995.

Hoffmann, K., and Chiang, S., Computational Fluid Dynamics, Vol. 3, 4<sup>th</sup> ed., Engineering Education System, Wichita, KS, USA, 2000.

Iqbal, O., and Arora, K., Windage Tray Design Comparison Using Crankcase Breathing Simulation, SAE Technical Paper 2013-01-0580, doi:10.4271/2013-01-0580, 2013.

Jayatileke, C.L., The Influence of Prandtl Number and Surface Roughness on the Resistance of the Laminar Sublayer to Momentum and Heat Transfer, Progress in Heat and Mass Transfer, Vol. 1, pp. 193-330, 1969.

Jiji, L.M., and Dagan, Z., Experimental Investigation of Single Phase Multi-Jet Impingement Cooling of Array of Microelectronic Heat Sources, Proceedings of the International Symposium on Cooling Technology for Electronic Equipment, Pacific Institute for Thermal Engineering, Honolulu, Hawaii, pp. 265-283, 1987.

Kader, B.A., Temperature and Concentration Profiles in Fully Turbulent Boundary Layers, Int. J. Heat and Mass Transfer, Vol. 24, pp. 1541-1544, 1981.

Kays, W.M., Turbulent Prandtl Number - Where Are We?, J. Heat Transfer, Vol. 116, pp. 284-295, 1994.

Lee, K., Aalburg, C., Diez, F.J., Faeth, G.M., and Sallam, K.A., Primary Breakup of Turbulent Round Liquid Jets in Uniform Crossflows, AIAA Journal, Vol. 45(8), pp. 1907-1916, 2007.

Leonard, B.P., The ULTIMATE Conservative Difference Scheme Applied to Unsteady One-Dimensional Advection, Computer Methods in Applied Mechanics and Engineering, Vol. 88, pp. 17-74, 1991.

Lienhard, J.H., Liu, V.X., and Gabour, L.A., Splattering and Heat Transfer During Impingement of a Turbulent Liquid Jet, J. Heat Transfer, Vol. 114(2), pp. 362-372, 1992.

Lienhard, J.H., Liquid Jet Impingement, Annual Review of Heat Transfer, Vol. 6, Ch. 4, pp. 199-270, NY, USA, 1995.

Lienhard, J.H., Heat Transfer by Impingement of Circular Free-Surface Liquid Jets, 18th National and 7th ISHMT-ASME, Heat and Mass Transfer Conference, Guwahati, India, 2006.

Lienhard IV, J.H., and Lienhard V, J.H., A Heat Transfer Textbook, 3<sup>rd</sup> ed., Phlogiston Press, Cambridge, MA, USA, 2008.

Liu, X., Lienhard, J.H., and Lombarda, S., Convective Heat Transfer by Impingement of Circular Liquid Jets, J. Heat Transfer, Vol. 113, pp. 571-582, 1991.

Liu, X., and Lienhard, J.H., Liquid Jet Impingement Heat Transfer on a Uniform Flux Surface, ASME Heat Transfer Division, Book No. H00498, Vol. 106, pp. 523-530, 1989.

Lowery, G.W., and Vachon, R.I., The Effect of Turbulence on Heat Transfer from Heated Cylinders, *Int. J. Heat and Mass Transfer*, Vol. 18, pp. 1229-1242, 1975.

Ma, C.F., and Bergles, A.E., Boiling Jet Impingement Cooling of Simulated Microelectronic Chips, *Proceedings of ASME: Heat Transfer in Electronic Equipment*, Boston, MA, pp. 5-12, 1983.

Mazallon, J., Dai, Z., and Faeth, G.M., Primary Breakup of Nonturbulent Round Liquid Jets in Gas Crossflows, *Atomization and Sprays*, Vol. 9(3), pp. 291–311, 1999.

Mehendale, A.B., Han, J.C., and Ou, S., Influence of High Mainstream Turbulence on Leading Edge Heat Transfer, *J. Heat Transfer*, Vol. 113, pp. 843-850, 1991.

Miyamoto, M., Sumikawa, J., Akiyoshi, T., and Nakamura, T., Effects of Axial Heat Conduction in a Vertical Flat Plate on Free Convection Heat Transfer, *Int. J. Heat and Mass Transfer*, Vol. 23, pp. 1545–1553, 1980.

Menter, F.R., Two-Equation Eddy-Viscosity Turbulence Modeling for Engineering Applications, *AIAA Journal*, Vol. 32(8), pp. 1598-1605, 1994.

Metzger, D.E., Cummings, K.N., and Ruby, W.A., Effect of Prandtl Number on Heat Transfer Characteristics of Impinging Liquid Jets, *Proceedings of the 5th International Heat Transfer Conference*, Tokyo, Japan, Vol. 2, pp. 20-24, 1974.

Muzaferija, S., Peric, M., Sames, P., and Schelin, T., A Two-Fluid Navier-Stokes Solver to Simulate Water Entry, *Proceedings of 22nd Symposium on Naval Hydrodynamics*, Washington, DC, USA, 1998.

Pai, M.G., Desjardins, O., and Pitsch, H., Detailed Simulations of Primary Breakup of Turbulent Liquid Jets in Crossflow, *Center for Turbulence Research, Annual Research Briefs*, University of Colorado, Boulder, CO, USA, 2008.

Pan, Y., Stevens, J., and Webb, B.W., Effect of Nozzle Configuration on Transport in the Stagnation Zone of Axisymmetric Impinging Free Surface Liquid Jets - Part 2: Local Heat Transfer, *J. Heat Transfer*, Vol. 114(4), pp. 880-886, 1992.

Pope, S.B., *Turbulent Flows*, Cambridge University Press, UK, 2000.

Pozzi, A., and Lupo, M., The Coupling of Conduction with Laminar Natural Convection Along a Flat Plate, *J. Heat and Mass Transfer*, Vol. 31, pp. 1807–1814, 1988.

Press, W.H., Teukolsky, S.A., Vetterling, W.T., and Flannery, B.P., *Multigrid Methods for Boundary Value Problems, Numerical Recipes, The Art of Scientific Computing*, 3<sup>rd</sup> ed., Cambridge University Press, NY, USA, 2007.

Rayleigh, L., On the Instability of Jets, *Proc. London Math. Soc.*, Vol. 10, pp. 4-13, 1878.

Reichardt, H., Vollstaendige Darstellung der turbulent en Geschwindigkeitsverteilung in Glatten Leitungen, *Z. Angew, Math. Mech.*, Vol. 31(7), pp. 208-219, 1951.

Rhie, C.M., and Chow, W.L., Numerical Study of the Turbulent Flow Past an Airfoil with Trailing Edge Separation. *AIAA J.*, Vol. 199, pp. 1525-1532, 1983.

Sallam, K.A., Dai, Z., and Faeth, G.M., Drop Formation at the Surface of Plane Turbulent Liquid Jets in Still Gases, *Int. J. Multiphase Flow*, Vol. 25, pp. 1161–1180, 1999.

Sallam, K.A., Dai, Z., and Faeth, G.M., Liquid Breakup at the Surface of Turbulent Round Liquid Jets in Still Gases, *Int. J. Multiphase Flow*, Vol. 28, pp. 427–449, 2002.

Sallam, K.A., Aalburg, C., and Faeth, G.M., Breakup of Round Non-turbulent Liquid Jets in Gaseous Crossflow, *AIAA Journal*, Vol. 42(12), pp. 2529–2540, 2004.

Sharan, A., and Hoshino, T., Jet-Disc Boiling: Burnout Predictions and Application to Solar Receivers, Master's Thesis in Mechanical Engineering, University of Houston, USA, 1984.

Shen, Y.C., Theoretical Analysis of Jet-Ground Plane Interaction, IAS Paper No. 62-144, 1962.

Spalart, P.R., and Rumsey, C.L., Effective Inflow Conditions for Turbulence Models in Aerodynamic Calculations, *AIAA Journal*, Vol. 45(10), pp. 2544-2553, 2007.

Stevens, J., Measurements of Local Fluid Velocities in an Axisymmetric Free Liquid Jet Impinging on a Flat Plate, PhD Thesis, Brigham Young University, USA, 1991.

Stevens, J., and Webb, B.W., Local Heat Transfer Coefficients Under an Axisymmetric, Single Phase Liquid Jet, *J. Heat Transfer*, Vol. 113, pp. 71-78, 1991.

Stevens, J., and Webb, B.W., Measurements of Free Surface Flow and Structure Under an Impinging Free Liquid Jet, *J. Heat Transfer*, Vol. 114(1), pp. 79-84, 1992.

Stevens, J., Pan, Y., and Webb, B.W., Effect of Nozzle Configuration on Transport in the Stagnation Zone of Axisymmetric Impinging Free-Surface Liquid Jets, *J. Heat Transfer*, Vol. 114(4), pp. 874-879, 1992.

- Stone, R., Introduction to Internal Combustion Engine, 4<sup>th</sup> ed., SAE International and Macmillan Press, USA, 2012.
- Strand, T., On the Theory of Normal Ground Impingement of Axisymmetric Jets in Inviscid Incompressible Flow, AIAA Paper No. 64-424, San Diego, CA, USA, 1964.
- Vader, D.T., Incropera, F.P., and Viskanta, R., Local Convective Heat Transfer from a Heated Surface to an Impinging Planar Jet of Water, Int. J. Heat and Mass Transfer, Vol. 34, pp. 611-623, 1991.
- Varghese, M., Goyal, S., and Agarwal, A., Numerical and Experimental Investigation of Oil Jet Cooled Piston, SAE Technical Paper 2005-01-1382, 2005.
- Venkatakrishnan, V., On the Convergence of Limiters and Convergence to Steady State Solutions, NASA Ames Research Centre, AIAA-93-0880, CA, USA, 1994.
- Versteeg, H.K., and Malalasekera, W., An Introduction to Computational Fluid Dynamics: The Finite Volume Method, 2<sup>nd</sup> ed., Pearson Education Ltd., UK, 2007.
- Vynnycky, M., and Kimura, S., Transient Conjugate Free Convection Due to a Heated Vertical Plate, Int. J. Heat and Mass Transfer, Vol. 39, pp. 1067–1080, 1996.
- Ubbink, O., Issa, R.I., Method for Capturing Sharp Fluid Interfaces on Arbitrary Meshes, J. Computational Physics, Vol. 153, pp. 26-50, 1999.
- Waclawczyk, T., and Koronowicz, T., Comparison of CICSAM and HRIC High-Resolution Schemes for Interface Capturing, J. Theoretical and Applied Mechanics, Vol. 46(2), pp. 325-345, 2008.
- Wang, X.S., Dagan, Z., and Jiji, L.M., Heat Transfer Between a Circular Free Impinging Jet and Solid Surface with Nonuniform Wall Temperature or Heat Flux - 1, Solution for the Stagnation Region, Int. J. of Heat and Mass Transfer, Vol. 32, pp. 1351-1360, 1989.
- Watson, E.J., The Radial Spread of a Liquid Over a Horizontal Plane, J. Fluid Mech., Vol. 20, pp. 481-499, 1964.
- Weber, C., Disintegration of Liquid Jets, Z. Angew Math. Mech., Vol. 11(2), pp. 136-159, 1931.
- White, F.M., Fluid Mechanics, 7<sup>th</sup> ed., McGraw-Hill Series in Mechanical Engineering, 2009.
- Wilcox, D.C., Turbulence Modelling for CFD, 2<sup>nd</sup> ed., DCW Industries Inc., La Canada, CA, USA, 1998.

Wilcox, D.C., Simulation of Transition with a Two-Equation Turbulence Model, AIAA J., Vol. 32(2), pp. 247-255, 1994.

Wu, P.K., Tseng, L.K., and Faeth, G.M., Primary Breakup in Gas/Liquid Mixing Layers for Turbulent Liquids, Atomization and Sprays, Vol. 2, pp. 295–317, 1992.

Wu, P.K., and Faeth, G.M., Aerodynamic Effects on Primary and Secondary Spray Breakup, Atomization and Sprays, Vol. 3, pp. 265–289, 1993.

Wu, P.K., Miranda, R.F., and Faeth, G.M., Effects of Initial Flow Conditions on Primary Breakup of Nonturbulent and Turbulent Round Liquid Jets, Atomization and Sprays, Vol. 5, pp. 175–196, 1995.

Wu, P.K., and Faeth, G.M., Onset and End of Drop Formation Along the Surface of Turbulent Liquid Jets in Still Gases, Phys. Fluids, Vol. 7, pp. 2915–2917, 1995.

Zaleski, S., Simulations of High Reynolds Number Breakup of Liquid-Gas Interfaces, Von Karman Institute for Fluid Dynamics, Lecture Series, 2002.

Zuckerman, N., and Lior, N., Jet Impingement Heat Transfer: Physics, Correlations and Numerical Modelling, Advances in Heat Transfer, Vol. 39, pp. 565-631, 2006.

## Appendix

### WRITTEN PERMISSION FROM THE COPYRIGHT HOLDERS

- A. Nasif, G., Barron, R.M., Balachandar, R. and Iqbal, O., 2013, "Simulation of Jet Impingement Heat Transfer", Proceedings of ASME 2013 Internal Combustion Engine Division (ICED), Fall Technical Conference, Paper No. ICEF2013-19050, Dearborn, MI, USA.
- B. Nasif, G., Barron, R.M. and Balachandar, R., 2014, "Heat Transfer Due to an Impinging Jet in a Confined Space", ASME, J. Heat Transfer, 136(11), doi: 10.1115/1.4028242.
- C. Nasif, G., Barron, R.M. and Balachandar, R., 2013, "Jet Impingement Heat Transfer: Moving Disc", Proceedings of the 22nd National and 11th ISHMT-ASME Heat and Mass Transfer Conference, Paper No. HMTC1300891, Kharagpur, India.
- D. Nasif, G., Barron, R.M. and Balachandar, R., 2014, "Simulation of Jet Impingement Heat Transfer onto a Moving Disc", Int. Journal of Heat and Mass Transfer, (paper accepted).
- E. Nasif, G., Barron, R.M. and Balachandar, R., 2014, "Heat Transfer Characteristics of Jet Impingement onto a Heated Disc Bounded by a Cylindrical Wall", Proceedings of the 10th International Conference on Heat Transfer, Fluid Mechanics and Thermodynamics (HEFAT), pp. 441-447, Orlando, FL, USA.
- F. Nasif, G., Barron, R.M. and Balachandar, R., 2014, "Jet Impingement Heat Transfer: Stationary Disc", International Journal of Surface Engineering and Materials Technology (IJSEMT), 4(1), pp. 34-38.

## Papers (A&B)



Ghassan Nasif <nasifg@uwindsor.ca>

### Letter of Permission/Copyrighted Material

Beth Darchi <DarchiB@asme.org>  
To: Ghassan Nasif <nasifg@uwindsor.ca>

Thu, Aug 7, 2014 at 3:41 PM

Dear Mr. Nasif:

This letter has been revised to reflect all request. It is our pleasure to grant you permission to use **all or any** part of the following ASME papers:

- "Simulation of Jet Impingement Heat Transfer", by Nasif, G., Barron, R.M., Balachandar, R. and Iqbal, C., ASME 2013 Internal Combustion Engine Division (ICED), Fall Technical Conference, Paper Number ICEF2013-19050
- "Heat Transfer Due to an Impinging Jet in a Confined Space", by Nasif, G., Barron, R.M. and Balachandar, R., *Journal of Heat Transfer*, 2014

as cited in your letter for inclusion in a Ph.D. thesis to be published by University of Windsor.

Permission is granted for the specific use as stated herein and does not permit further use of the materials without proper authorization. Proper attribution must be made to the author(s) of the materials. **PLEASE NOTE:** if any or all of the figures and/or Tables are of another source, permission should be granted from that outside source or include the reference of the original source. ASME does not grant permission for outside source material that may be referenced in the ASME works.

As is customary, we request that you ensure full acknowledgment of this material, the author(s), source and ASME as original publisher. Acknowledgment must be retained on all pages printed and distributed.

Many thanks for your interest in ASME publications.

Sincerely,



Beth Darchi  
Publishing administrator  
ASME  
2 Park Avenue, 8th Floor  
New York, NY 10016-5900  
Tel: 1.212.591.7700  
darchi@asme.org



## Paper (C)



Ghassan Nasif <nasifg@uwindsor.ca>

---

### Letter of Permission/Copyrighted Material

---

Prof. Suman Chakraborty <sumanchakraborty\_iitkgp@yahoo.com>

Fri, Aug 8, 2014 at  
12:41 AM

Reply-To: sumanchakraborty\_iitkgp@yahoo.com

To: Ghassan Nasif <nasifg@uwindsor.ca>

Dear Ghassan,

As I mentioned, you may use the material presented by you in the 22nd National and 11th ISHMT-ASME Heat and Mass Transfer Conference, Kharagpur, India (paper # HMTTC1300891) towards your Ph.D. thesis, on approval from your thesis advisor.

Regards,

Suman Chakraborty

Dr Suman Chakraborty  
Professor, Department of Mechanical Engineering  
Indian Institute of Technology (IIT)  
Kharagpur-721302, INDIA

**Paper (D)**



Ghassan Nasif <nasifg@uwindsor.ca>

---

**Elsevier Oxford - HMT-D-14-01209 [Reference: 140813-002984]**

---

EP Support <support@elsevier.com>  
Reply-To: EP Support <support@elsevier.com>  
To: nasifg@uwindsor.ca

Wed, Aug 13, 2014 at 8:52 AM

**Subject**

Elsevier Oxford - HMT-D-14-01209

**Discussion**

**Response Via Email (Roser Raurich i Roura)**

13/08/2014 12:52 PM

Dear Dr Nasif,

Thank you so much for taking the time to talk to me.

After further investigation, the editorial office of "International Journal of Heat and Mass Transfer" has informed me that "the author has the rights to use their accepted or final published article for inclusion in their thesis".

Please see the below link:

<http://www.elsevier.com/journal-authors/author-rights-and-responsibilities#author-use>

For any further assistance, please do not hesitate to contact me.

Kind regards,

Roser Raurich i Roura  
Researcher Support

**Customer By Phone (Entered by Roser Raurich i Roura)**

13/08/2014 12:49 PM

Author wanted to use info from an article that is under review.

## Paper (E)



Ghassan Nasif <nasifg@uwindsor.ca>

---

### Letter of Permission/Copyrighted Material

---

Josua Meyer <Josua.Meyer@up.ac.za>  
To: Ghassan Nasif <nasifg@uwindsor.ca>

Wed, Aug 6, 2014 at 3:22 PM

Dear Gus:  
You are welcome to use it for your PhD.  
Regards  
Josua



Ghassan Nasif <nasifg@uwindsor.ca>

---

### Letter of Permission/Copyrighted Material

---

Ghassan Nasif <nasifg@uwindsor.ca>  
To: Josua Meyer <josua.meyer@up.ac.za>

Wed, Aug 6, 2014 at 9:10 AM

Dear Prof. Meyer,

I have paper presented recently in 10th International Conference on Heat Transfer, Fluid Mechanics and Thermodynamics HEFAT, 2014, Orlando-Florida, details as follow:

*Nasif, G., Barron, R.M. and Balachandar, R., 2014, "Heat Transfer Characteristics of Jet Impingement onto a Heated Disc Bounded by a Cylindrical Wall", 10th International Conference on Heat Transfer, Fluid Mechanics and Thermodynamics (HEFAT), Orlando, FL, USA.*

I need to use the material of this paper towards my Ph.D. thesis. I appreciate if I can get a letter of permission for this purpose.

Thank you for your cooperation in this regard.

Gus Nasif, P.Eng  
Mechanical Engineering Department  
University of Windsor  
Windsor, Ontario  
Canada

## Paper (F)



Ghassan Nasif <nasifg@uwindsor.ca>

---

### Letter of Permission /Copyrighted Material

---

hazoor sidhu <hazoors@yahoo.com>

Tue, Aug 12, 2014 at 6:17 AM

Reply-To: hazoor sidhu <hazoors@yahoo.com>

To: Pardeep Jindal <pardeepjindal79@gmail.com>, "nasifg@uwindsor.ca" <nasifg@uwindsor.ca>

Dear Author

This is in reference to your mail regarding your paper, [ Nasif, G., Barron, R.M. and Balachandar, R., 2014, "**Jet Impingement Heat Transfer: Stationary Disc**", International Journal of Surface Engineering and Materials Technology (IJSEMT), 4(1), pp. 34-38].

Author can use his research work publish in journal for his own Phd thesis.

Thank you

Dr. Hazoor Singh Sidhu  
Associate Professor of Mechanical Engineering  
Yadvindra College of Engineering  
Punjabi University, Guru Kashi Campus  
Ramma-mandi Road  
Talwandi Sabo, Distt. Bathinda  
Punjab, India-151302  
(Mobile +91-81462-60200)

[Quoted text hidden]

## VITA AUCTORIS

Name: Ghassan (Gus) Nasif

Year of Birth: 1967

Place of Birth: Baghdad-Iraq

Education: University of Baghdad,  
Baghdad, Iraq  
B.Sc. in Nuclear Engineering, 1990

University of Technology,  
Baghdad, Iraq  
M.A.Sc. in Mechanical Engineering, 1995

University of Windsor,  
Windsor, ON  
M.Eng. in Mechanical Engineering, 2008

University of Windsor,  
Windsor, ON  
Ph.D. in Mechanical Engineering, 2014